ADAPTIVE ARRAY SIGNAL PROCESSING ALGORITHMS FOR LEO SATELLITE COMMUNICATIONS

GABRIEL BORGES PINHEIRO

DISSERTAÇÃO DE MESTRADO
EM ENGENHARIA ELÉTRICA

DEPARTAMENTO DE ENGENHARIA ELÉTRICA

FACULDADE DE TECNOLOGIA

UNIVERSIDADE DE BRASÍLIA

Universidade de Brasília
Faculdade de Tecnologia
Departamento de Engenharia Elétrica

Adaptive Array Signal Processing Algorithms for LEO Satellite Communications

Gabriel Borges Pinheiro

DISSERTAÇÃO DE MESTRADO SUBMETIDA AO PROGRAMA DE PÓS-GRADUAÇÃO EM ENGENHARIA ELÉTRICA DA UNIVERSIDADE DE BRASÍLIA COMO PARTE DOS REQUISITOS NECESSÁRIOS PARA A OBTENÇÃO DO GRAU DE MESTRE.

APROVADA POR:

Prof. Daniel Costa Araújo, Dr. (ENE-UnB)
(Orientador)

Prof. Felix Dieter Antreich, Dr. (ITA)
(Examinador Externo)

Prof. Leonardo Aguayo, Dr. (ENE-UnB)
(Examinador Interno)

Brasília/DF, Agosto de 2025.

FICHA CATALOGRÁFICA

PINHEIRO, GABRIEL BORGES

Adaptive Array Signal Processing Algorithms for LEO Satellite Communications. [Brasília/DF] 2025.

835, 109p., 210 x 297 mm (ENE/FT/UnB, Mestre, Dissertação de Mestrado, 2025).

Universidade de Brasília, Faculdade de Tecnologia, Departamento de Engenharia Elétrica.

Departamento de Engenharia Elétrica

1. LEO Satellite Communication
2. Large-space Arrays
3. Uniform Planar Array
4. DoA Estimation
5. Doppler shift
6. Symbol Timing

I. ENE/FT/UnB

II. Título (série)

REFERÊNCIA BIBLIOGRÁFICA

PINHEIRO, GABRIEL BORGES (2025). Adaptive Array Signal Processing Algorithms for LEO Satellite Communications. Dissertação de Mestrado, Publicação PPGEE.DM-835/25, Departamento de Engenharia Elétrica, Universidade de Brasília, Brasília, DF, 109p.

CESSÃO DE DIREITOS

AUTOR: Gabriel Borges Pinheiro

TÍTULO: Adaptive Array Signal Processing Algorithms for LEO Satellite Communications.

GRAU: Mestre ANO: 2025

É concedida à Universidade de Brasília permissão para reproduzir cópias desta Dissertação de Mestrado e para emprestar ou vender tais cópias somente para propósitos acadêmicos e científicos. O autor reserva outros direitos de publicação e nenhuma parte desta dissertação de mestrado pode ser reproduzida sem autorização por escrito do autor.

Gabriel Borges Pinheiro

Universidade de Brasília (UnB)

Campus Darcy Ribeiro

Faculdade de Tecnologia - FT

Departamento de Engenharia Elétrica(ENE)

Brasília - DF CEP 70919-970

ACKNOWLEDGEMENTS

I would like to express my deepest gratitude to all those who have supported me throughout this master's journey.

First and foremost, I extend my heartfelt thanks to my advisor and the project coordinator. Thank you for believing in my potential and my hard work, and for giving me the invaluable opportunity to be a part of this project through the scholarship I was awarded. Your guidance and trust were fundamental to the successful completion of this dissertation.

To my loved ones, including my family and friends, thank you for your unwavering support, patience, and encouragement during this period. Your presence was a constant source of strength and motivation.

Finally, this work was made possible through the financial support of the National Council for Scientific and Technological Development (CNPq). I gratefully acknowledge the funding provided for this research project through the *Uniespaço* grant program, Process *405635/2022-2*, entitled *"Estação Terrena Autônoma Distribuída de Baixo Custo e Alta Taxa de Download"*, under the Action *"Chamada CNPq Nº 20/2022 - Faixa A"*.

ABSTRACT

Title: Adaptive Array Signal Processing Algorithms for LEO Satellite Communications
Author: Gabriel Borges Pinheiro
Advisor: Prof. Dr. Daniel Costa Araújo
Postgraduate Program in Electrical Engineering.
Brasília, august of 2025.

This dissertation presents the modeling, simulation, and performance evaluation of a signal processing chain for a low Earth orbit (LEO) satellite ground station composed of a uniform planar array (UPA) of parabolic antennas. The study focuses on the downlink reception of digitally modulated signals and explores methods to enhance signal acquisition and synchronization in the presence of Doppler shift and time-varying propagation effects. The communication model is implemented assuming a circular LEO orbit, free-space path loss, and the use of pilot-based synchronization sequences. The work investigates techniques for array signal processing, including frequency division multiplexing (FDM) to mitigate grating lobes in large-spaced arrays, frequency-locked loop (FLL) for carrier phase correction, and the Mueller and Muller algorithm for symbol timing synchronization. Subspace-based methods—Singular Value Decomposition (SVD) and PAST algorithm—are employed for Direction of Arrival (DoA) estimation using the MUSIC approach, followed by spatial filtering using Wiener and Delay-and-Sum beamformers. Simulations conducted in Python demonstrate the system's ability to correct Doppler and timing offsets and estimate the DoA of received signals, with results showing improved bit error rate (BER) performance under different noise conditions. The study provides a foundation for implementing advanced ground station receivers for LEO satellite networks and sets directions for future extensions to more realistic channel models and adaptive antenna systems.

RESUMO

Título: Algoritmos de Processamento Adaptativo de Sinais em Arranjos para Comunicações via Satélites LEO

Autor: Gabriel Borges Pinheiro

Orientador: Prof. Dr. Daniel Costa Araújo

Programa de Pós-Graduação em Engenharia Elétrica.

Brasília, agosto de 2025.

Esta dissertação apresenta a modelagem, simulação e avaliação de desempenho de uma cadeia de processamento de sinal para uma estação terrena de satélite em órbita baixa terrestre (LEO), composta por um arranjo planar uniforme (UPA) de antenas parabólicas. O estudo concentra-se na recepção de sinais digitalmente modulados no enlace de descida e na aplicação de métodos para aprimorar a aquisição e sincronização do sinal sob efeitos de variação temporal e desvio Doppler. O modelo de comunicação é implementado assumindo uma órbita circular LEO, perda de percurso em espaço livre e o uso de sequências piloto para sincronização.

São investigadas técnicas de processamento de sinais de arranjo, incluindo a multiplexação por divisão de frequência (FDM) para mitigação de lóbulos de grade em arranjos de grande espaçamento, o laço travado em frequência (FLL) para correção de fase do portador e o algoritmo de Mueller e Muller para sincronização temporal de símbolos. Métodos baseados em subespaço — Decomposição em Valores Singulares (SVD) e o algoritmo PAST — são empregados para a estimação da Direção de Chegada (DoA) via método MUSIC, seguida de filtragem espacial utilizando os filtros Wiener e Delay-and-Sum. As simulações, desenvolvidas em Python, demonstram a capacidade do sistema em corrigir desvios de fase e tempo, bem como estimar a DoA dos sinais recebidos, apresentando melhorias na taxa de erro de bits (BER) sob diferentes condições de ruído. O trabalho fornece uma base para o desenvolvimento de receptores avançados de estações terrenas para redes de satélites LEO e aponta direções para futuras extensões do modelo a canais mais realistas e sistemas de antenas adaptativos.

TABLE OF CONTENTS

LIST OF FIGURES

LIST OF TABLES

LIST OF SYMBOLS

$\mathbf{A}^T$	Transpose of matrix $\mathbf{A}$
$\mathbf{A}^{-1}$	Inverse of matrix $\mathbf{A}$
$\mathbf{I}n$	$n \times n$ identity matrix $\mathbf{A}$
$\text{diag}(\mathbf{r})$	Diagonal matrix formed with the vector $\mathbf{r}$
$\|\mathbf{r}\|$	Norm of the vector $\mathbf{r}$
$\mathbf{a} \cdot \mathbf{b}$	Dot product between the vectors $\mathbf{a}$ and $\mathbf{b}$
$\jmath$	Complex imaginary unity
z^*	Conjugate of the complex number z
$\text{Re}\{z\}$	Real part of the complex number z
$\text{Im}\{z\}$	Imaginary part of the complex number z
$\angle(z)$	Phase argument of the complex number z
$\mathbf{A}^H$	Transpose of complex matrix $\mathbf{A}^*$
$z \sim \mathcal{CN}(\mu,\mathbf{R}_\sigma)$	z is a Complex Gaussian random variable with mean μ and covariance matrix $\mathbf{R}_\sigma$
$z \sim \mathcal{U}[a,b]$	z is a Uniform random variable contained in the $[a,b]$ interval.
r,θ,ϕ	Radius, zenith angle and azimuth angle
ϑ	Elevation angle
$\hat{\mathbf{x}},\hat{\mathbf{y}},\hat{\mathbf{z}}$	Cartesian unitary basis vectors
$\hat{\mathbf{r}},\hat{\theta},\hat{\phi}$	Spherical unitary basis vectors
M_E	Mass of the Earth
R_E	Mean radius of the Earth
h	Altitude of the satellite
T	Satellite orbital period
T_p	Satellite pass duration
$\mathbf{r}(t)_{Sat}$	Satellite position
$\mathbf{r}(t)_{GS}$	GS position
$v_r(t)$	GS-satellite velocity
f_0	Carrier frequency
$f_d(t)$	Doppler frequency shift
d	Diameter of the aperture of the parabolic dish
$\mathbf{F}(\theta)$	Antenna pattern field
$G(\theta)$	Power gain of the element antenna
η_a	Parabolic antenna efficiency coefficient
α,β,γ	Rotation angles for the z,y,x axes
$\mathbf{R}(\alpha,\beta,\gamma)$	Rotation matrix
λ_i	Wave length of the i-th signal wave
$\mathbf{k}_i$	Wave vector of the i-th signal wave
N	Number of array elements

μ_n	Spatial frequency associated to the n-th array element
$\mathbf{a}(\mathbf{\Theta})$	Steering vector associated to the angle vector $\Theta = [\theta,\phi]$
$A(\mu_n)$	Array factor associated to the n-th array element
$\mathbf{w}$	Filter coefficients vector
$\mathbf{a}_i$	Array steering vector
R	Bit rate
T_s	Symbol duration
$p(t)$	Pulse impulse response
M	Number of the set of bandpass symbols
$s(t)$	Analog bandpass signal at time domain
$s^m(t)$	m-th bandpass symbol pulse waveform
K	Number of pulses of a signal
$\text{erfc}(x)$	Complementary error function
P_b	Probability of a bit error function
b	Roll-off factor
P_N	Total system noise power
B	Received signal bandwidth
τ_i	Propagation delay of the i-th signal wave
α_i	FSPL coefficient of the i-th signal wave
κ	Rician κ-factor
$\mathbf{s}_i$	Sampled baseband signal of the i-th signal source
μ_i	Spatial frequency of the i-th signal wave
$\mathbf{G}$	Gain diagonal matrix
$\mathbf{A}$	Array manifold matrix
$\mathbf{W}$	Matrix of received signal AWGN
$\mathbf{X}$	Received signal matrix
$E[\mathbf{X}]$	Expected value of $\mathbf{X}$
$r(t)$	Envelope of the received passband signal
f_n	Carrier frequency associated to the array element n
$\mathbf{R}$	Covariance matrix of $\mathbf{X}$
$\mathbf{U}$	Subspace matrix of $\mathbf{X}$
$\mathbf{U}_s$	Subspace matrix of the transmitted baseband signal
$\mathbf{U}_w$	Subspace matrix of the received signal noise
$J(\mathbf{\Theta})$	MUSIC pseudospectrum function associated to the angle vector $\Theta = [\theta,\phi]$
$\mathbf{w}$	Spatial filter coefficients
$\mathbf{y}$	Reception signal combined with $\mathbf{w}$
$\mathbf{h}_{LP}$	Time response of a low-pass filter

GLOSSARY

ADC Analog-to-Digital Converter

AF Array Factor

AWGN Additive White Gaussian Noise

BER Bit Error Rate

BPSK Binary PSK

DoA Direction-of-Arrival

DOF Degrees of Freedom

DSP Digital Signal Processing

EM Electromagnetic

ECEF Earth-Centered, Earth-Fixed

ECI Earth-Centered Inertial

ERFC Complementary Error Function

ESPRIT Estimation of Signal Parameters via Rotational Invariance Techniques

FDM Frequency Division Multiplexing

FLL Frequency-Locked Loop

FSPL Free-Space Path Loss

GCS Global Coordinate System

GEO Geostationary Earth Orbit

GNSS Global Navigation Satellite System

GS Ground Station

ISI Intersymbol Interference

LCS Local Coordinate System

LEO Low Earth Orbit

LNA Low-Noise Amplifier

LoS Line-of-Sight

MaM Mueller and Müller

MUD Multi-User Detection

MUSIC Multiple Signal Classification

NASA National Aeronautics and Space Administration

NCO Numerically Controlled Oscillator

NDA Non-Data-Aided

NLoS Non-Line-of-Sight

NORAD North American Aerospace Defense Command

PAST Projection Approximation Subspace Tracker

PLL Phase-Locked Loop

PSK Phase Shift Keying

QAM Quadrature Amplitude Modulation

QPSK Quadrature Phase Shift Keying

RAAN Right Ascension of the Ascending Node

RF Radio Frequency

SE Spectral Efficiency

SGP4 Simplified General Perturbations 4

SINR Signal-to-Interference-plus-Noise Ratio

SNR Signal-to-Noise Ratio

SDR Software-Defined Radio

SVD Singular Value Decomposition

ULA Uniform Linear Array

UPA Uniform Planar Array

URA Uniform Rectangular Array

TLE Two-Line Element

UT User Terminal

VCO Voltage-Controlled Oscillator

CHAPTER 1

INTRODUCTION

1.1 CONTEXTUALIZATION

Satellite communications represent a fundamental pillar in the evolution of global connectivity, linking people and organizations across vast distances. In this landscape, Low Earth Orbit (LEO) satellites have emerged as a particularly dynamic and crucial component, offering significant advantages such as low latency, high bandwidth, and higher signal stability (HE *et al.*, 2021). The recent proliferation of small satellite constellations for applications ranging from global internet service to high-resolution Earth observation has created an unprecedented demand for a more capable, flexible, and cost-effective Ground Station (GS) infrastructure to support them (PRATT; ALLNUTT, 2019). GSs are the terrestrial piece of this ecosystem, serving as the critical reception and transmission points for all satellite data. The ability of these stations to acquire, track, and maintain a clear communication link is paramount to the success of any satellite mission (INGRAM *et al.*, 2005). Figure 1.1 illustrates an overview of a satellite 'end-to-end' link, toward the uplink-downlink direction.

To meet the demands of modern LEO constellations, advanced adaptive signal processing techniques are quite beneficial. One of the most powerful methods in this domain is the use of planar antenna arrays combined with beamforming. This technology allows for the precise electronic steering of a signal beam, enabling robust signal capture and directionality, which significantly enhances the quality and reliability of the communication link (ZAKI *et al.*, 2020). The impact of such technology is noticeable across numerous sectors, including high-quality media broadcasting, stable high-speed internet for real-time applications, and critical functions like military navigation and remote environmental sensing (TREES, 2002).

Historically, the ground segment for LEO satellites has been dominated by large, mechanically-steered parabolic antennas. A typical GS utilizes a single dish, often as large as 11 meters in

Figure 1.1. A typical satellite link. The GS sends a message for a User Terminal (UT) through a satellite toward the uplink-downlink direction (Forward-link), and the UT sends another message back (Return-link) to GS.

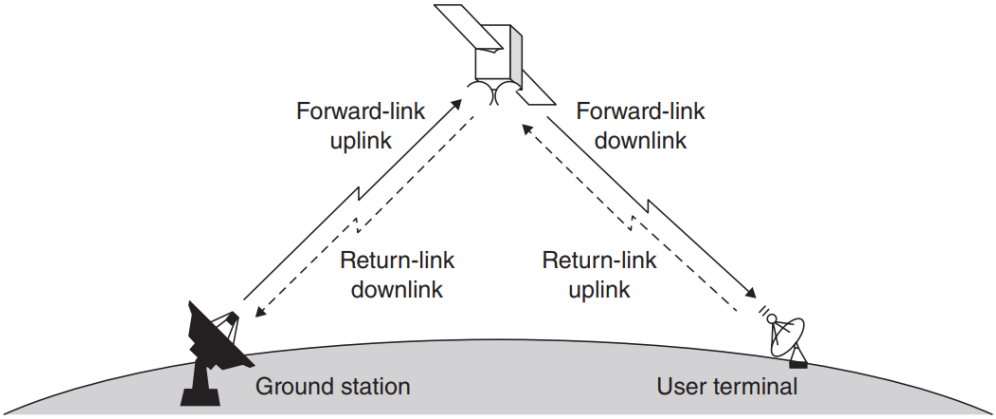

Source: (BRAUN; BRAUN, 2021).

diameter, which tracks one satellite at a time by physically slewing its position. Although effective, and capable of supporting downlinks up to 150 Mbps, this model has substantial drawbacks, such as the construction of such a station represents a significant capital investment, on the order of $4 million, until the last decade, and is accompanied by high ongoing operational and maintenance costs (RONDINEAU *et al.*, 2006). Furthermore, to maximize contact time with satellites in polar orbits, these facilities are optimally located in high-latitude, often remote, regions, limiting their geographical distribution (ZAKI *et al.*, 2020).

This traditional paradigm was challenged by a new architecture for GSs, as explored by researchers such as (INGRAM *et al.*, 2004) in "Optimizing Satellite Communications With Adaptive and Phased Array Antennas."The proposed shift is from a single, large, mechanical antenna to a system composed of multiple, smaller, electronically-steered antenna arrays. This approach seeks to replace costly and failure-prone moving parts with robust digital signal processing. The core concept involves adaptively combining the signals from an array of moderately directive antennas to maximize the Signal-to-Interference-plus-Noise Ratio (SINR), as shown in the Figure 1.2. This not only allows for tracking of the desired satellite but also provides inherent capabilities for mitigating terrestrial interference, making it feasible to deploy GSs in more populated, non-polar, regions.

This dissertation is motivated by the project called "Low-Cost, High-Download Rate, Distributed, and Autonomous Ground Station"(LCEPT, 2022) (translated), and it aligns directly

Figure 1.2. The implemented discrete lens antennas array, on the left. On the right side, the adaptive scheme to get the spatial filtering data and beamforming.

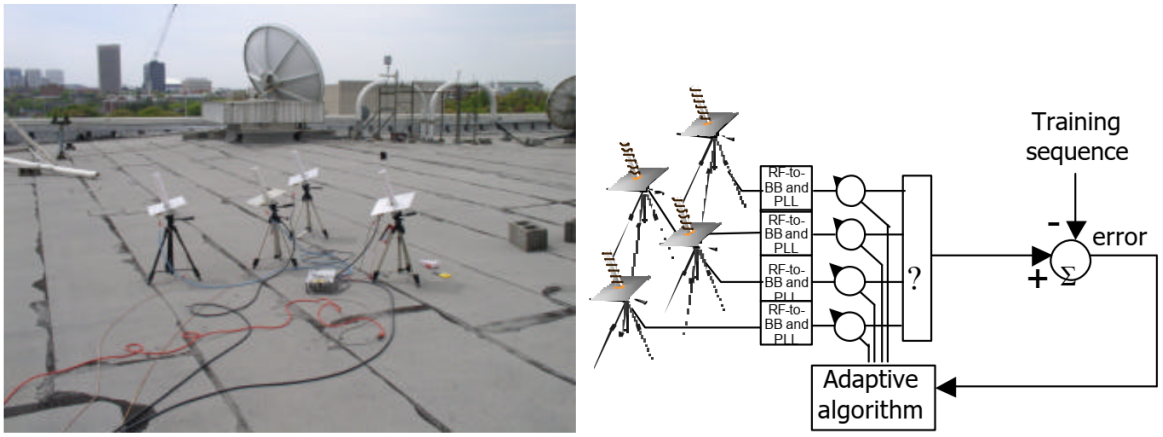

Source: (INGRAM *et al.*, 2004).

with this innovative approach. The primary objective is to investigate the feasibility of such GS. The vision is to develop a remotely programmable station with ideally no moving parts, at a target cost of less than a tenth of current systems. The physical architecture will be centered on an array of antennas with small-to-moderate apertures. The main research thrust will be on the physical layer, focusing on the radio-frequency front-end and, most critically, the implementation of adaptive digital signal processing algorithms to coherently combine the outputs from the array elements. This approach not only allows for agile tracking of the desired satellite but also provides inherent capabilities for mitigating terrestrial interference by maximizing the Signal-to-Interference-plus-Noise Ratio (SINR), making it feasible to deploy GSs in more accessible, non-polar regions (INGRAM *et al.*, 2004).

The core idea on (INGRAM *et al.*, 2004) is while a single station of this new type may not initially match the peak data rates of a massive parabolic dish, the strategic advantage lies in distribution. By drastically lowering the cost, a dense network of these GSs can be deployed and interconnected via the internet. This creates a distributed ground segment, allowing for data to be downloaded sequentially as a satellite passes over a series of stations, thereby enabling near-continuous communication with LEO assets. The architecture under investigation is also inherently flexible, designed for rapid reconfiguration to allow for fast-switching between satellites or even future communication with multiple satellites simultaneously (LCEPT, 2022).

By focusing on this innovative GS architecture, this work aims to contribute directly to

Figure 1.3. GS on University of Brasília, Gama Campus. The antenna array (planar) is highlighted.

Source: Own authorship. Photo taken via Google Maps.

the technological advancement of satellite communications, addressing a key infrastructural challenge to help build a more connected world.

1.2 PROBLEMATIC

The implementation of adaptive array systems for LEO satellite communications entails several significant technical challenges. These challenges stem from the complexity of the physical propagation environment, system geometry, and dynamic satellite movement. This section outlines key problem areas encountered in this research domain, from the physical imperfections of the antenna array to the complex nature of the propagation channel and the signal environment.

1.2.1 Array Calibration and Inter-Element Coupling

In theoretical models, antenna arrays are often treated as ideal structures: each element is assumed to be identical, perfectly matched, and electromagnetically isolated from its neighbors. However, real-world implementations deviate significantly from this idealization. Manufacturing tolerances introduces element-wise variations in gain, phase, and impedance characteristics. More critically, the Electromagnetic (EM) fields radiated by each antenna element induce cur-

rents in adjacent elements - a phenomenon known as mutual coupling (SOBRINHO *et al.*, 2024).

Mutual coupling alters the effective impedance seen by each antenna and distorts the array radiation pattern, causing the array manifold. These deviations are particularly problematic for high-resolution Direction-of-Arrival (DoA) estimation algorithms - e.g., MUSIC, ESPRIT - and adaptive beamforming techniques, which rely on accurate modeling of the array response to perform spatial filtering and signal separation (MORI, 2023).

Without compensation, these imperfections result in beam misalignment, degraded interference suppression, etc. Hence, in such degraded conditions, the array's ability to focus on the desired signal while suppressing interferers becomes fundamentally compromised. Therefore, calibration becomes essential. It aims to identify and correct gain and phase mismatches, as well as model and compensate for mutual coupling effects, thereby restoring the array to a condition approximating its theoretical performance (SOBRINHO *et al.*, 2024).

1.2.2 DoA Estimation

Direction-of-Arrival (DoA) estimation refers to determining the angular coordinates from which EM waves impinge on an antenna array. For satellite communications, accurate DOA information is essential for tracking moving satellites, optimizing beamforming, and improving Spectral Efficiency (SE) through precise spatial filtering, being central to beam steering.

However, satellite motion, signal noise, and low Signal-to-Noise Ratio (SNR) conditions can produce ambiguous or unstable angle estimates, especially when the satellite approaches from low elevation angles or when closely spaced multipath components exist (CHENG *et al.*, 2013).

Furthermore, the very high velocity of LEO satellites introduces a significant and rapidly changing Doppler shift. This effect on links can cause carrier frequency shifts up to tens of kHz and introduce significant phase rotation per symbol, which can lead the beamforming algorithm to steer the main lobe away from the true satellite direction, severely impacting the communication link.

1.2.3 Multipath Signal Reading

In many operational environments, particularly urban and suburban areas, the signal from the LEO satellite does not only arrive via a direct Line-of-Sight (LoS) path. It also reflects and scatters off buildings, terrain, and other obstacles, creating multiple indirect paths to the receiver. This multipath propagation causes the received signal to be a superposition of several delayed and attenuated copies of the original signal.

This phenomenon leads to multipath fading, where the signal strength fluctuates rapidly, and delay spread, which can cause Intersymbol Interference (ISI) in high-data-rate systems (DAVIS *et al.*, 1997).

1.2.4 Grating Lobes from Large-arrays

Grating lobes are replicas of the main beam that appear at predictable angles in the radiation pattern when the inter-element spacing exceeds half a wavelength of the signal frequency (BALANIS, 2016). The presence of grating lobes has several detrimental effects (TREES, 2002):

1. Ambiguity in DoA Estimation: A grating lobe is indistinguishable from the main lobe in terms of gain. This means the array cannot tell if a signal is coming from the intended direction or from the direction of a grating lobe. This ambiguity is catastrophic for DoA estimation algorithms, which may lock onto a grating lobe instead of the true satellite position.

2. Increased Susceptibility to Interference: Just as grating lobes can transmit power in unwanted directions, they can also receive it. A strong interfering signal located in the direction of a grating lobe will be received with the same gain as the desired signal in the main lobe, making it impossible for the array to suppress the interference through spatial filtering alone.

3. Reduced Gain and Efficiency: Power radiated into grating lobes is wasted energy that is not contributing to the main beam. This reduces the overall gain and efficiency of the antenna system.

1.2.5 Propagation time synchronization

Before any data can be demodulated, the receiver must achieve precise timing synchronization with the incoming signal. This involves aligning the receiver local clock with the symbol timing of the received waveform. Timing misalignment in sampling clock causes ISI and decoding errors. Failure to maintain accurate timing synchronization results in a high Bit Error Rate (BER) and can lead to a complete loss of the communication link (SKLAR, 2020).

In the LEO satellite context, this is complicated by the significant and time-varying propagation delay. As the satellite moves from the horizon to its highest point and back to the horizon, the path length changes dramatically, causing the propagation delay to vary continuously. This satellite travels at approximately 7.5 km/s, which can induce substantial frequency shifts, disrupting the orthogonality of subcarriers in multicarrier systems and degrading performance if not properly compensated (MARAL *et al.*, 2020).

1.2.6 Interference from Other Signal Sources

Satellite GSs are susceptible to interference from a multitude of terrestrial and non-terrestrial sources. These can include other satellite systems, terrestrial microwave links, cellular networks, and broadcast services operating in adjacent frequency bands. This interference can be powerful enough to overwhelm the weak signal received from the LEO satellite, significantly reducing the SINR and degrading communication quality (MARAL *et al.*, 2020). The primary advantage of an adaptive antenna array is its ability to mitigate this interference by forming nulls in its radiation pattern in the direction of the interfering sources. However, this ability is dependent on the number of array elements, the accuracy of DOA estimation for both the desired signal and the interference, and the quality of the array calibration. Effectively identifying and nulling multiple, potentially mobile, sources of interference is a key challenge in the design of the GS signal processing algorithms (TREES, 2002).

1.3 BRIEF LITERATURE REVIEW

This section provides a brief overview of the state-of-the-art in the core technologies that are foundational to this work.

The development of adaptive antenna arrays for LEO satellite communications builds upon decades of research in several key areas of signal processing and antenna theory. Current research focuses heavily on adaptive signal processing to optimize the array performance. This task involves processing data in the modem by employing algorithms to coherently combine signals from multiple elements to maximize SINR and actively suppress terrestrial interference by steering nulls in the radiation pattern to unwanted sources.

The adaptive combination of signals from multiple receive antennas offers several key features that are critical for a high-performance GS:

- Array Gain: This is the most direct benefit of using an array. By coherently combining the signals from multiple elements, the overall SNR is improved. For an array with N elements, each receiving a signal with a similar SNR, the combined output SNR is enhanced by a factor of $10\log_{10}(N)$ in dB. This gain is valuable for reliably detecting the weak signals transmitted by satellites.

- Diversity Gain: Satellite signals are often affected by multipath fading, a condition where multiple copies of the signal arrive at the receiver from different directions. These copies can add together destructively, causing a dramatic drop in signal strength. Since the elements of an array are spatially separated, they are unlikely to all experience a deep fade at the same time. An adaptive combiner can capitalize on this by intelligently weighting the signals, thus making the output signal far more resilient to multipath effects. This improvement in signal stability is known as **diversity gain**.

- Interference Suppression and Multi-User Detection (MUD): In today crowded radio spectrum, interference from other signal sources is a major concern. An adaptive array can mitigate this by electronically forming "nulls"in its radiation pattern, effectively deafening itself to signals arriving from the direction of the interference. This capability can be extended to MUD, which would allow the GS to separate signals from multiple satellites

transmitting on the same frequency within the array field of view (LoS). As long as the signals from different satellites arrive from distinct directions, the array processor can compute a unique set of combining weights for each one, isolating the desired signal while suppressing the others.

1.3.1 DoA Tracking

In the satellite context, especially for LEO systems, DoA estimation must cope with high mobility, short pass durations, and multipath interference. Some methods are listed below.

- **Subspace-Based Methods**: Algorithms like Multiple Signal Classification (MUSIC) (SEKIZAWA, 1998) and Estimation of Signal Parameters via Rotational Invariance Techniques (ESPRIT) (ROY; KAILATH, 1989) have been the cornerstone of DoA estimation for decades. These methods exploit the eigen-decomposition of the received signal covariance matrix to achieve high-resolution DoA estimates, separating the signal subspace from the noise subspace, especially when the number of sources is known. MUSIC variants like Root-MUSIC have improved performance in the presence of correlated multipath, and their performance, however, MUSIC is highly dependent on accurate channel and array manifold knowledge (KRIM; VIBERG, 1996).

  The (Standard) ESPRIT algorithm provides faster computation by leveraging subarray invariance (ROY; KAILATH, 1989). Its technique also has well-nowed variants, like Unitary-ESPRIT, offers additional optimizations to the computational load (HAARDT *et al.*, 1998) and as well there is an adaptive implementation of ESPRIT based on the Projection Approximation Subspace Tracker (PAST) signal subspace estimation method, better suited for non-stationary signals. This adaptive method uses previous estimates in a feedback loop, optimizing data processing time and reducing the complexity to a linear $O(nr)$ versus the standard SVD-based implementation that has complexity of $O(n^2)$ (BADEAU *et al.*, 2003).

- **Machine Learning Approaches**: More recently, Machine Learning and Deep Learning techniques have been applied to the DoA estimation problem. These methods can learn the complex, non-linear relationship between the received signal and the DoA, even

in the presence of array imperfections and multipath. Supervised learning models can be trained on extensive datasets of simulated or measured signals to achieve high accuracy, while unsupervised methods can adapt to changing channel conditions (LIU, 2020), (MORADKHANI *et al.*, 2022), (XU *et al.*, 2023), (ZHENG *et al.*, 2024).

- **Compressed Sensing**: Compressed sensing techniques have also been employed to reduce the number of required measurements and the computational complexity of DOA estimation, which is particularly relevant for large number of array elements (MIRZA *et al.*, 2020), (SHI *et al.*, 2023), (JIANG *et al.*, 2023), (LIN *et al.*, 2021), (LIU *et al.*, 2024).

1.3.2 Symbol Synchronization

Symbol synchronization, or timing recovery, is crucial in mitigating timing offset and jitter in high-data-rate satellite links, as mentioned in Section 1.2.5. Classic Non-Data-Aided (NDA) algorithms are widely used for symbol synchronization as they do not require known training sequences.

The Gardner algorithm is a popular choice due to its simplicity and effectiveness in moderate ISI conditions, especially in low SNR conditions (GARDNER, 1986). The early-late gate synchronizer is another classic method that provides robust performance (MENGALI, 2013). Mueller and Müller (MaM) has advantage of needing only one sample per symbol (1 symbol interval) of signal (MUELLER; MULLER, 1976).

1.3.3 Doppler Frequency Shift Correction

The large and time-varying Doppler shift in LEO satellite links must be continuously tracked and corrected to prevent a loss of coherence.

- **Closed Loops**: The most common methods for carrier and phase recovery are either Phase-Locked Loop (PLL) or Frequency-Locked Loop (FLL). They are a feedback control system that generates an output signal whose phase is related to the phase of an input signal. In a satellite receiver, the PLL tracks the phase of the incoming carrier, effectively removing the Doppler-induced frequency shift (KAPLAN; HEGARTY, 2017),

(TEUNISSEN; MONTENBRUCK, 2017).

- **Doppler Pre-Compensation**: With accurate orbital data (e.g., from Two-Line Elements (TLEs)), it is possible to predict the Doppler shift at the GS from a theoretical model and pre-compensate for it, either at the transmitter or the receiver. This significantly reduces the burden on the receiver tracking loops (ALI *et al.*, 2013).

1.3.4 Processing Techniques for Large-Space UPA

For avoiding grating lobes issues in the scanned signal, shown in Section 1.2.4, one of the most effective strategies is to abandon uniform spacing and design aperiodic or non-uniform arrays. By optimizing the positions of the elements, it is possible to suppress the grating lobes that arise from periodic structures. This can be achieved through various optimization algorithms that find the best element placement for a given application (ZHANG *et al.*, 2018), (KRIVOSHEEV *et al.*, 2015).

Another approach involves using specific array geometries, such as T-shaped or L-shaped arrays. These configurations use multiple co-prime sub-arrays to resolve the ambiguity caused by grating lobes, effectively providing an unambiguous 2D Direction of Arrival (DOA) estimation even with large element spacing (SHENG *et al.*, 2023), (LIU *et al.*, 2022).

Furthermore, advanced signal processing techniques can be employed. This includes using antenna elements with specific radiation patterns, such as a null-scanning antenna, which can be designed to place a null in the direction of the grating lobe, effectively suppressing it (KHALILPOUR *et al.*, 2020). Similarly, exciting higher-order modes in the antenna elements can be used to reduce grating lobes, especially when scanning the beam to wide angles (WANG *et al.*, 2018), (WANG *et al.*, 2008).

(PINHEIRO *et al.*, 2024) proposes a novel Frequency Division Multiplexing (FDM) strategy. This technique introduces frequency diversity across elements during RF demodulation, effectively emulating a non-uniform array geometry and suppressing spatial aliasing, leading to their suppression without altering the physical array geometry. Thereby enhancing beamforming performance for satellite tracking.

1.4 OBJECTIVES

The topics about Array Calibration and Inter-element Coupling (Section 1.2.1), Multipath Signal Reading (Section 1.2.3), and Interference from Other Signal Sources (Section 1.2.6) will not be addressed in this work, due to the restriction of the scope of studies for this dissertation. Methods to treat these deleterious effects are considered for others — future — works (5.3.1), and such effects will not be considered in the models developed in this study.

1.4.1 General Objective

The primary objective of this dissertation is to develop and simulate adaptive signal processing algorithms for a proper LEO satellite GS downlink that utilizes a large-space Uniform Planar Array (UPA).

1.4.2 Specific Objectives

- Develop a signal model representative of the reception scenario in LEO satellite communications, accounting for satellite dynamics and UPA array features, like a physical model for the antennas.

- Implement algorithms to perform DoA estimation of the incoming satellite signal at the GS.

- Implement algorithms for spatial filtering of the signal received from the array.

- Analyze the impact of Doppler shift and time-varying propagation effects on system performance, assessing the performance of spatial filtering. Furthermore, propose appropriate compensation methods.

- Explore and implement a novel method to mitigate grating lobes in large-space arrays using Frequency Division Multiplexing (FDM) techniques.

1.5 DOCUMENT STRUCTURE

This dissertation is organized into five main chapters, each addressing a key aspect of the research, from theoretical foundations to implementation and analysis.Follow its detailing.

Chapter 1 : Introduction

This chapter provides the foundational context for the research.

- Section 1.1 establishes the scope and relevance of the work.
- Section 1.2 details the primary challenges inherent in LEO satellite communication with antenna arrays.
- Section 1.3 presents a brief review of any state-of-the-art techniques relevant to this field.
- Finally, Section 1.4 outlines the specific objectives and goals of this dissertation.

Chapter 2 : Theoretical Basis

This chapter is dedicated to the theoretical framework of the systems.

- Section 2.1 describes the spatial scenario of LEO satellites and the consequential effects of their orbital mechanics on the communication link.
- Section 2.2 covers the theoretical tools for modeling the GS array, discussing spherical coordinates, the physical model for parabolic antennas, and the transformation between Local and Global Coordinate Systems.
- Section 2.3 presents the complete model for the LEO satellite communication signal, detailing the flow from bit assignment to Quadrature Phase Shift Keying (QPSK) symbol mapping, pulse shaping with a Raised-Cosine filter, and culminating in a model for the signal received by the array.

Chapter 3 : System Model

This chapter details the signal being modeled and its distortion effects.

Chapter 4 : Proposed Architecture

This chapter details the implementation of the core signal processing algorithms.

- Section 4.1 introduces the novel FDM-based technique for mitigating grating lobes.
- Section 4.2 covers the statistical parametric estimation of the received signal, employing Singular Value Decomposition (SVD) for subspace decomposition and PAST for subspace decomposition.
- Section 4.3 focuses on the implementation of a DoA estimation algorithm, such as MUSIC.
- Section 4.4 discusses the use of spatial filtering for the final reconstruction of the desired signal.
- Finally, Section 4.5 describes the methods for correcting timing and frequency errors, specifically the MaM algorithm for symbol synchronization and a FLL for Doppler frequency shift correction.

Chapter 5 : Results and Conclusions

The final chapter presents the outcomes of the research.

- Section 5.1 show the setups parameters for the system implementation.
- Section 5.2 provides a detailed description of the simulations performed and an in-depth analysis of the implemented algorithms' performance.
- Section 5.2 summarizes the key findings of the dissertation, draws final conclusions, and suggests potential avenues for future work.

CHAPTER 2

THEORETICAL BASIS

2.1 SCENARIO

LEO satellites operate in a environment that dictates their design, function, and interaction with GS. Understanding their orbital characteristics is fundamental to designing any communication system that relies on them. This section details the essential elements of LEO satellite motion, from the classical laws governing their paths to the practical data formats used to track them and the real-world forces that perturb their orbits.

2.1.1 Spherical Coordinates

The analysis of electromagnetic wave propagation and antenna radiation patterns is most naturally described using a coordinate system that matches the geometry of the expanding wavefronts. The basic aspects of spherical coordinates used in this work are described in Chapter A in the Appendix.

Earth-Centered Inertial (ECI) and Earth-Centered, Earth-Fixed (ECEF) Coordinate Systems

To describe the position and motion of a satellite and relate it to a ground station, two fundamental coordinate systems are used: the ECI frame and the ECEF frame. The key difference between them is that the ECI frame is non-rotating with respect to the distant stars, while the ECEF frame rotates with the Earth (VALLADO, 2013).

The ECI coordinate system is a non-rotating, or inertial, frame of reference. Its origin is at the center of the Earth mass, but its axes are fixed with respect to the celestial sphere (i.e., the distant stars). This "inertial" property is crucial because the laws of physics that govern

a satellite orbit, such as Newton's laws of motion and Kepler's laws, are simpler and more naturally expressed in a non-accelerating frame.

- Origin: Earth center of mass.
- Fundamental Plane: The Earth equatorial plane.
- Principal Direction (X-axis): Points towards the vernal equinox, which is a fixed direction in space where the ecliptic plane intersects the celestial equator.
- Orientation: The axes do not rotate with the Earth.

Because orbital mechanics are described in this non-rotating frame, the classical Keplerian orbital (Section 2.1.2) or TLE (Section 2.1.3) parameters are used to calculate a satellite state vector (position and velocity). The resulting position vector is naturally expressed in the ECI coordinate system. This frame is ideal for propagating the satellite trajectory through space. This coordinate system, as its name implies, is fixed to the Earth and rotates with it. Its axes are aligned with the Earth body, making it a non-inertial, accelerating frame.

- Origin: Earth center of mass.
- Z-axis: Points towards the North Pole.
- X-axis: Points towards the intersection of the prime meridian (0^o longitude, passing through Greenwich, England) and the equator.
- Y-axis: Completes the right-handed system.

When relating a satellite position to a fixed location on Earth, such as a GS or a Geostationary Earth Orbit (GEO) satellite, the natural reference frame is the ECEF system. A location in ECEF $\mathbf{r}_{gs}$ can be directly mapped to its geographic coordinates. The latitude (ϑ) is the angle north or south from the equatorial plane, and the longitude (ϕ) is the angle east or west from the Greenwich meridian. These geographic coordinates, in turn, are used to determine the pointing angles from a ground station to a satellite, namely the Azimuth (compass direction) and Elevation (angle above the horizon).

To track a satellite, a GS must continuously perform a time-dependent rotation to convert the satellite predicted position from the ECI frame (where its orbit is described) to the ECEF frame $\mathbf{r}_{sat}$ (to know where it is relative to the rotating Earth).

2.1.2 The Keplerian Orbit

LEO satellites move in elliptical orbits governed by Kepler's laws of planetary motion, assuming an idealized two-body system (Earth and satellite). This model is defined by a set of six classical parameters - Keplerian orbital elements - along with the position of the satellite within it at a specific time (**epoch**), they are illustrated in the Figure 2.1:

1. **Semi-Major Axis (a)**: Defines the size of the orbit. It is half the length of the longest axis of the ellipse.

2. **Eccentricity (e)**: This describes the shape of the elliptical orbit. An eccentricity of 0 corresponds to a perfect circle, while values between 0 and 1 indicate an ellipse. The higher the eccentricity, the more elongated the orbit.

3. **Inclination (i)**: This is the angle between the orbital plane of the satellite and the equatorial plane of Earth. An inclination of 0^o means that the satellite orbits directly above the equator, while an inclination of 90 °0 signifies a polar orbit.

4. **Right Ascension of the Ascending Node (RAAN) (Ω)**: This parameter orients the orbital plane in space. The ascending node is the point where the satellite crosses the equatorial plane moving from south to north. Ω is the angle measured eastward in the equatorial plane from a fixed reference direction in space to the ascending node.

5. **Argument of Perigee (ω)**: This defines the orientation of the ellipse within the orbital plane. It is the angle measured in the direction of the satellite motion from the ascending node to the perigee — the point in the orbit closest to the Earth.

6. **True Anomaly (ν)**: This specifies the satellite position along its elliptical path at a given epoch. It is the angle measured from the perigee to the satellite current position vector.

Figure 2.1. (a) Elliptical satellite orbit. Can be seen the Perigee and Apogee distances, and the Major and Minor Axes. (b) Any orbital parameters traced in relation to the equatorial plane.

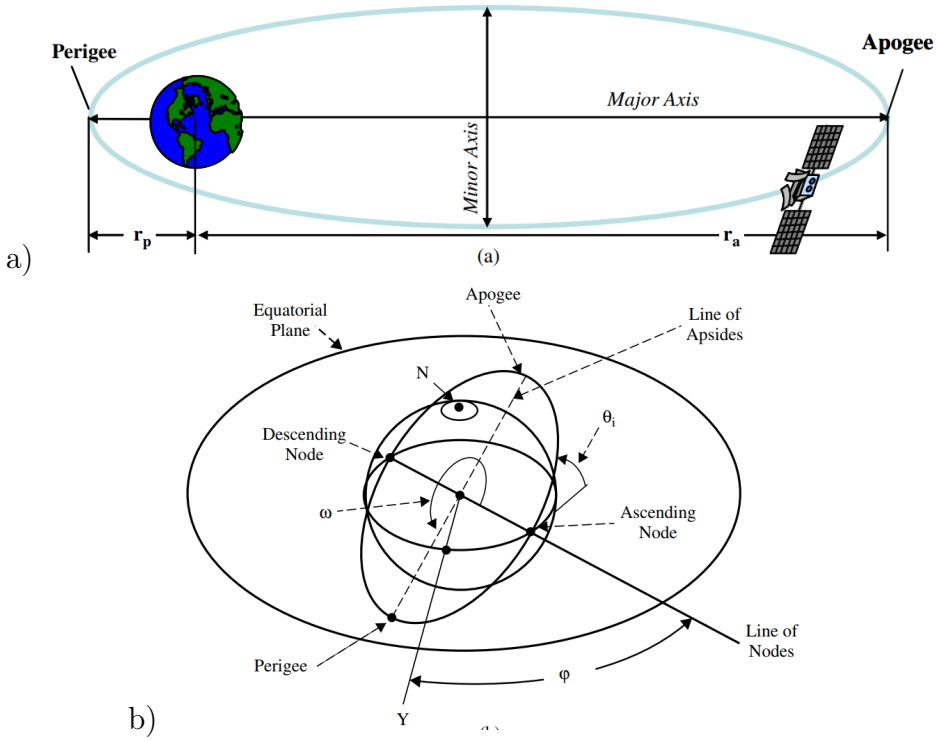

Source: (JR, 2017).

Due to the relatively low altitude of LEO satellites compared to the Earth radius, their orbits often exhibit very small eccentricities ($e \approx 0$) (PRATT; ALLNUTT, 2019). As a result, it is generally acceptable to approximate the elliptical orbit as circular, simplifying calculations without introducing significant error.

Perturbations of Orbits

A satellite orbit is not a perfect ellipse due to various perturbing forces that cause it to deviate from the ideal Keplerian path. The most significant of these for LEO satellites are(VALLADO, 2013):

- **Earth Asphericity**: The Earth is not a perfect sphere; it is an oblate spheroid, bulging at the equator. This non-uniform mass distribution causes gravitational variations that lead to a long-term precession of RAAN Ω and the argument of perigee ω.

- **Atmospheric Drag**: For satellites at lower altitudes (below 1000 km), the friction from

the Earth tenuous upper atmosphere is a major perturbing force. This drag acts opposite to the direction of motion, causing the satellite to lose energy and its orbit to decay, gradually decreasing the semi-major axis a and eccentricity e.

- **Third-Body Perturbations**: The gravitational pull from the Sun and the Moon can also alter a satellite orbit, primarily affecting the inclination i and Ω over long periods.

2.1.3 TLE format

While keplerian elements perfectly describe an ideal orbit, real-world orbits are not perfect. To track satellites in practice, the North North American Aerospace Defense Command (NORAD) and National Aeronautics and Space Administration (NASA) uses a format called the TLE set, it contains the orbital elements of an object at an epoch. The TLE format indirectly accounts for perturbations, they are mean orbital elements averaged over time to account for perturbations (VALLADO, 2013).

A TLE consists of a title line followed by two lines of data in a specific format (CELESTRAK, 2022):

- **Line 1**:
  - Epoch (YYDDD.DDDDDD format);
  - First and second derivatives of mean motion $\dot{v}$, $\ddot{v}$;
  - BSTAR drag term.
- **Line 2**:
  - Inclination i;
  - RAAN Ω;
  - Eccentricity e;
  - Argument of perigee ω;
  - Mean anomaly M;
  - Mean motion v.

These data, including key perturbations, are used as input for an orbital propagation model, such as Simplified General Perturbations 4 (SGP4), to predict the position and velocity of the satellite at any point in the near future (VALLADO, 2013).

The BSTAR drag term in line 1 is a coefficient used by the SGP4 to estimate the effects of atmospheric drag. The model also includes terms to handle the secular (long-term) perturbations caused by the Earth oblateness. Because these perturbations continuously change the orbit, TLE for LEO satellites must be updated frequently - often every few days - to maintain tracking accuracy (CELESTRAK, 2022).

2.1.4 Orbital Velocity

The velocity of a LEO satellite is not constant unless its orbit is perfectly circular. According to Kepler's Second Law, a satellite moves fastest at perigee and slowest at apogee (the nearest and farthest point from Earth, respectively). For a simplified circular orbit, the radius of the orbit r is the sum of Earth's radius and the satellite's altitude, and the orbital velocity (v) is determined by balancing gravitational and centripetal forces, in which the following formula is obtained (PRATT; ALLNUTT, 2019):

$$v = \sqrt{\frac{GM}{R_E + h}}, \tag{2.1}$$

where:

- $G = 6.674 \times 10^{-11}\,\mathrm{Nm^2/kg^2}$ (gravitational constant),
- $M_E = 5.972 \times 10^{24}\,\mathrm{kg}$ (Earth's mass),
- $R_E = 6371\,\mathrm{km}$ (Earth mean radius),
- h: Average altitude of the satellite.

The Orbital Period - also called Revolution Period - (T) can be calculated as

$$T = 2\pi \frac{R_E + h}{v}. \tag{2.2}$$

For example, LEO satellites, which typically orbit at altitudes between 200 and 2,000 km, this results in extremely high velocities, on the order of 7.3 km/s, completing an orbit in about 100 minutes (PRATT; ALLNUTT, 2019).

2.1.5 Coverage and Satellite Pass

The coverage area, or footprint, of a satellite is the portion of the Earth surface from which the satellite is visible.This area is a circle whose size depends on the satellite altitude and the minimum elevation angle required for a ground station to establish a reliable link (MARAL *et al.*, 2020). A satellite pass duration T_p is the period during which a satellite is visible above the local horizon of a ground station, allowing for direct LoS communication.The pass begins at the Acquisition of Signal and ends at the Loss of Signal point. It is influenced primarily by the orbital altitude h and the satellite footprint.

When the satellite beamwidth is large enough to fully cover the local horizon, the mean pass duration can be approximated by a simple linear relation with respect to the satellite altitude. Based on the article "A Tractable Approach for Predicting Pass Duration in Dense Satellite Networks"(AL-HOURANI, 2021) the approximate minimal pass duration $T_p^{\min}$ (in minutes) for a LEO satellite with altitude h in kilometers is given by

$$T_p^{\min} \approx 9.31 \times 10^{-3} \cdot h[\text{km}] + 4.68. \quad [\text{min}] \tag{2.3}$$

This formula is derived under the **isotropic assumption** where satellites are modeled using a random circular orbit model (i.e., a stochastic geometry approach). Due to their high velocity, LEO satellites have a limited **visibility window** over any ground location, typically between 5 and 15 minutes per pass (INGRAM *et al.*, 2004).

2.1.6 Doppler Shift

One of the most prominent features of the LEO satellite channel is the significant Doppler shift, which is a change in the frequency of the received signal due to the high relative velocity between the satellite and the ground station, as already discussed in Subseção 1.2.5.

Let the distance between GS-satellite $D(t) = \|\mathbf{r}(t)_{\text{sat}} - \mathbf{r}(t)_{\text{GS}}\|$ be the so-called **slant range** and $v_r(t) = \frac{dD(t)}{dt}$ be its relative velocity of the satellite, the Doppler shift, $f_d(t)$, can be modeled by (MARAL *et al.*, 2020):

$$f_d(t) = \frac{v_r(t)}{c} f_0, \tag{2.4}$$

where c is the speed of light and f_0 is the carrier frequency.

The relative velocity, $v_r(t)$, changes throughout the satellite pass, being maximum when the satellite is at the horizon (rising or setting) and zero when the satellite is at its highest elevation point directly overhead (assuming a direct overhead pass). For a typical S-band system at $f_0 = 2\,\text{GHz}$, the Doppler shift may reach up to $\pm 50\,\text{kHz}$, depending on the satellite's trajectory relative to the observer. This time-varying nature of the Doppler shift requires continuous tracking and compensation at the receiver.

It is worth mentioning that the initial estimate for the Doppler frequency shift can be predicted analytically from the satellite's orbital parameters (e.g., available in TLEs). Given the known orbital velocity $\mathbf{v}_{\text{sat}} = v_r\hat{\mathbf{r}} + v_\theta\hat{\theta} + v_\phi\hat{\phi}$, satellite position $\mathbf{r}_{\text{sat}}$, and the ground station position $\mathbf{r}_{\text{GS}}$, the relative velocity in the line-of-sight direction v_r is computed as:

$$v_r(t) = \hat{\mathbf{r}} \cdot \mathbf{v}_{\text{sat}} = \frac{(\mathbf{r}_{\text{sat}} - \mathbf{r}_{\text{gs}})}{||\mathbf{r}_{\text{sat}} - \mathbf{r}_{\text{gs}}||} \cdot \mathbf{v}_{sat} = \frac{(\mathbf{r}_{\text{sat}} - \mathbf{r}_{\text{gs}})\mathbf{v}_{sat}^T}{D} \tag{2.5}$$

2.2 ANTENNA MODEL

The core of the GS receiving system is the antenna array. To accurately simulate the performance of this system and implement effective signal processing algorithms, a precise mathematical model of the antennas radiation characteristics is of great value. This section details the physical model for a UPA composed of parabolic dish antennas.

2.2.1 Far-Field Parabolic Antenna Model

A parabolic reflector antenna is a high-gain antenna used for point-to-point communications, and it functions by reflecting the electromagnetic waves from a feed source placed at its focal point. This process transforms the spherical waves from the feed into a nearly uniform plane wave across the antenna aperture, resulting in a highly directive beam. In the far-field region, the radiated electric field can be determined by applying the principles of Fourier optics to the field distribution across the aperture (ORFANIDIS, 2016).

For a model shown in Figure 2.2, the electric field vector, $\mathbf{E}(r, \theta, \phi)$, at a large distance r from the antenna, can be expressed in its spherical polarization components, E_θ and E_ϕ. These

components represent the projection of the electric field onto the unit vectors $\hat{\theta}$ and $\hat{\phi}$ in a spherical coordinate system. Based on the principles outlined in (SMOLDERS *et al.*, 2019), supposing an isotropic feeder, the far-field components can be modeled as:

$$\begin{aligned} E_\theta(r,\theta,\phi) &= \; jk_i\frac{d^2}{4}E_0\frac{e^{-jk_ir}}{2r}(1+\cos\theta)\cos\phi\frac{J_1\left(k_i\frac{d}{2}\sin\theta\right)}{k_i\frac{d}{2}\sin\theta} \\ E_\phi(r,\theta,\phi) &= -jk_i\frac{d^2}{4}E_0\frac{e^{-jk_ir}}{2r}(1+\cos\theta)\sin\phi\frac{J_1\left(k_i\frac{d}{2}\sin\theta\right)}{k_i\frac{d}{2}\sin\theta}, \end{aligned} \tag{2.6}$$

where:

- $k = 2\pi/\lambda$ is the wavenumber, and λ is the signal wavelength.
- d is the diameter of the aperture of the parabolic dish.
- θ is the angle measured from the antenna main axis, on the boresight (positive Z-axis for this case).
- J_1 is the order one Bessel function of the first kind
- E_0 is a complex constant representing the field on the boresight.

Figure 2.2. Parabolic antenna. Side view, on the left, the feed antenna illuminates a parabolic reflector. Frontal view, on the right, the origin of coordinate system is on the center.

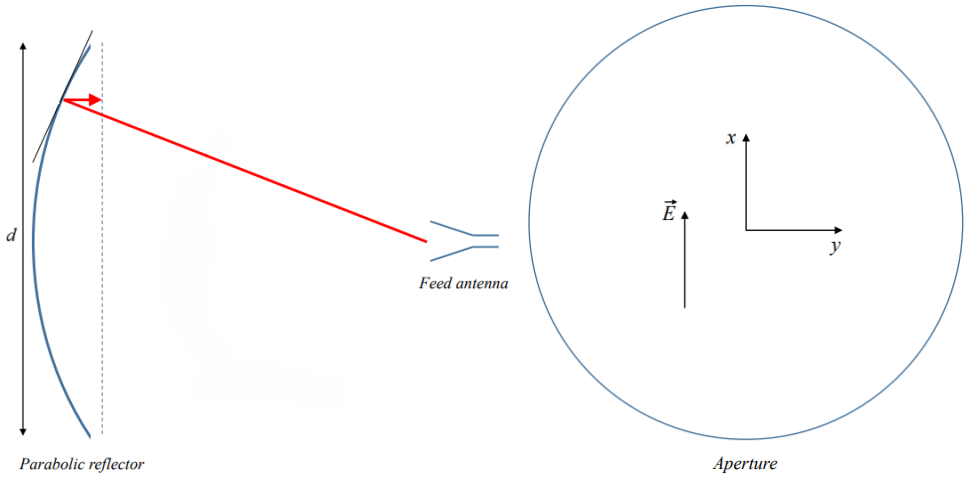

Source: (SMOLDERS *et al.*, 2019).

They are the perpendicular components of $\mathbf{E}_\perp(r,\theta,\phi)$, then its magnitude is

$$\|\mathbf{E}_\perp(r,\theta,\phi)\|^2 = \|\mathbf{E}_\theta(r,\theta,\phi)\|^2 + \|\mathbf{E}_\phi(r,\theta,\phi)\|^2, \tag{2.7}$$

and the radiation pattern magnitude associated with it is

$$\|\mathbf{F}(\theta)\|^2 = \frac{\|\mathbf{E}_\perp(\theta,\phi)\|^2}{E_0^2} = (1+\cos\theta)^2 \left[\frac{J_1\left(k_i \frac{d}{2}\sin\theta\right)}{k_i \frac{d}{2}\sin\theta}\right]^2 \tag{2.8}$$

and does not depend neither on r nor on ϕ.

The **gain** of an antenna, $G(\theta)$, is a fundamental parameter that quantifies its ability to concentrate radiated power in a specific direction relative to an isotropic source that radiates power equally in all directions. For a parabolic antenna, the gain is directly proportional to its effective aperture area and inversely proportional to the square of the wavelength.

The gain is closely related to the directivity, $D(\theta)$, which is the gain of a hypothetical lossless antenna. The directivity is determined by the radiation pattern:

$$D(\theta) = D_0|F(\theta)|^2 = D_0(1+\cos\theta)^2 \left[\frac{J_1\left(k_i \frac{d}{2}\sin\theta\right)}{k_i \frac{d}{2}\sin\theta}\right]^2, \tag{2.9}$$

where $D_0 = \eta_a \left(\frac{4\pi A_p}{\lambda^2}\right)$ is the maximum directivity occurring at the boresight ($\theta = 0^o$), within $A_p = \frac{\pi d^2}{4}$ being the physical area of the aperture. Its radiation pattern is illustrated on Figure 2.3, it can be seen that its directivity is very narrow, with high gain in boresight. To achieve gain diversity, each antenna element should point in a different direction, as argued in Section 5.3.1.

Figure 2.3. A parabolic antenna radiation pattern of the (2.8).

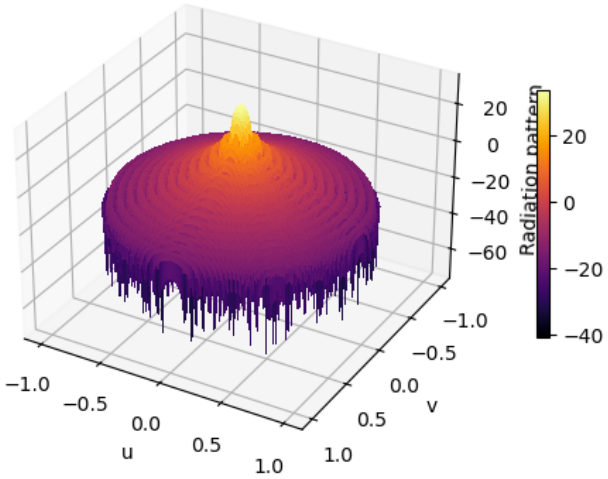

Source: Own authorship.

The actual gain is the directivity reduced by the antenna efficiency, η_a, which accounts for

various practical losses such as feed spillover, aperture blockage by the feed structure, non-uniform illumination, and resistive losses (SMOLDERS *et al.*, 2019), therefore

$$G(\theta) = \eta_a D(\theta). \tag{2.10}$$

The maximum gain, G_0, which occurs on the boresight axis, is a key figure of merit and is given by

$$G_0 = \eta_a D_0 = \eta_a \left(\frac{\pi d}{\lambda}\right)^2. \tag{2.11}$$

The aperture efficiency, η_a, for a typical parabolic reflector antenna generally falls in the range of 55% to 65% (ORFANIDIS, 2016).

2.2.2 Global and Local Coordinate Systems

In the analysis and simulation of antenna arrays — especially in 3D propagation environments such as those encountered in satellite or millimeter wave systems—defining precise coordinate systems is necessary. The Global Coordinate System (GCS) provides a universal frame of reference for network-wide evaluations, while the Local Coordinate System (LCS) defines the orientation and radiation pattern of each individual antenna element or array panel.

They are illustrated in Figure 2.4, at left. The GCS ($\hat{\mathbf{r}} = [x\ y\ z]$) serves as an absolute, universal frame of reference for the entire communication scenario. It is used to define the positions of all entities within a common space. The LCS ($\hat{\mathbf{r}}' = [x'\ y'\ z']$) is defined relative to each antenna array. Its orientation is defined via three rotations, as exemplified in Figure 2.4, (ETSI, 2020):

- α: **bearing** angle (rotation about GCS z-axis),
- β: **downtilt** (rotation about the intermediate $\dot{y}$-axis),
- γ: **slant** (rotation about the rotated $\ddot{x}$-axis).

This rotation sequence allows any mechanical orientation of the antenna relative to the global frame and it is through a coordinate transformation based on a composite rotation matrix

$$\mathbf{R}(\alpha,\beta,\gamma) = R_z(\alpha)R_y(\beta)R_x(\gamma) \tag{2.12}$$

Figure 2.4. At left, relation between references in GCS (θ,ϕ) and LCS (θ',ϕ'). At right, set of axis rotation angles α, β and γ, respectively

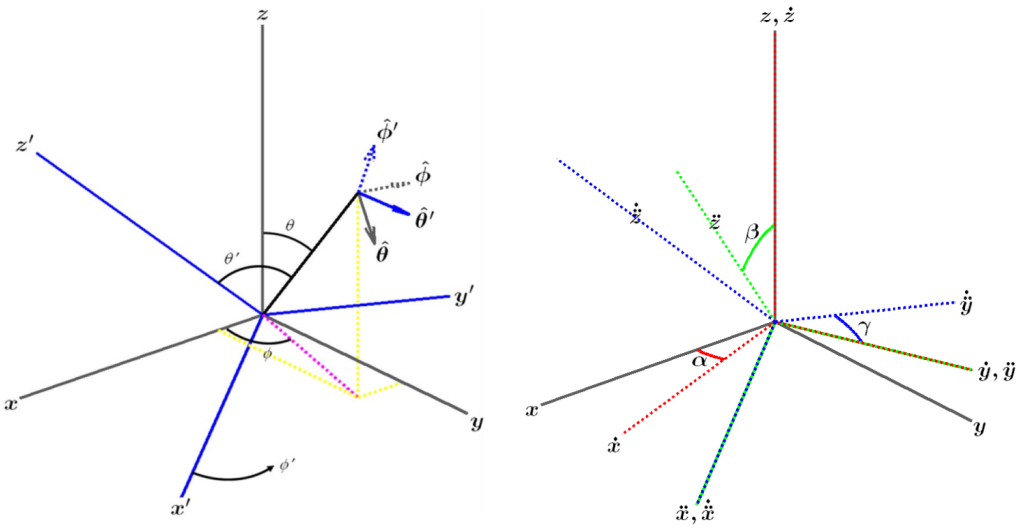

Source: (ETSI, 2020).

in which

$$R_z(\alpha) = \begin{pmatrix} +\cos\alpha & -\sin\alpha & 0 \\ +\sin\alpha & +\cos\alpha & 0 \\ 0 & 0 & 1 \end{pmatrix}, \; R_y(\beta) = \begin{pmatrix} +\cos\beta & 0 & +\sin\beta \\ 0 & 1 & 0 \\ -\sin\beta & 0 & +\cos\beta \end{pmatrix} \tag{2.13}$$

$$\text{and } R_x(\gamma) = \begin{pmatrix} 1 & 0 & 0 \\ 0 & +\cos\gamma & -\sin\gamma \\ 0 & +\sin\gamma & +\cos\gamma \end{pmatrix}. \tag{2.14}$$

Therefore, it is possible to compute $[x \; y \; z]^T = \mathbf{R}[x' \; y' \; z']^T$.

Knowing that $\mathbf{R}$ is orthogonal, the reverse transformation (negative angles) is given by

$$\mathbf{R}^{-1} = \mathbf{R}^T = R_x(-\gamma)R_y(-\beta)R_z(-\alpha). \tag{2.15}$$

2.2.2.1 LCS to GCS Conversion

Let $\mathbf{F}'(\theta',\phi') = F'_{\theta'}\hat{\theta}' + F'_{\phi'}\hat{\phi}'$ be the radiation pattern of an antenna defined in the LCS. Its corresponding pattern in the GCS is $\mathbf{F}(\theta,\phi) = F_\theta\hat{\theta} + F_\phi\hat{\phi}$. The purpose is apply coordinate transformations so that:

$$\mathbf{F}(\theta,\phi) = \mathbf{F}'(\theta',\phi'). \tag{2.16}$$

Coordinates Transformation

Having specified α,β,γ rotations on the antenna element, first, from the desired GCS coordinates θ, ϕ are obtained these corresponding LCS coordinates θ', ϕ'. To do this, the unitary vector $\hat{\mathbf{r}}$ from Equação A.4 of GCS is transformed in LCS through

$$\hat{\mathbf{r}}' = \mathbf{R}^{-1}\hat{\mathbf{r}}. \tag{2.17}$$

Then, the converted coordinates are obtained from the (A.3):

$$\begin{aligned} \theta' &= \arccos(z') = \arccos([0\ 0\ 1]\ \ \hat{\mathbf{r}}') \\ \phi' &= \angle(x' + \jmath y') = \angle([1\ \jmath\ 0]\ \ \hat{\mathbf{r}}') \end{aligned} \tag{2.18}$$

Polarized Field Component Transformation

Given the polarized field components in LCS $F'_\theta(\theta', \phi')$ and $F'_\phi(\theta', \phi')$, finally, for computing the conversion of the Equação 2.16, and knowing that $\hat{r} + \hat{\theta} + \hat{\phi} = \mathbf{R}\ (\hat{r'} + \hat{\theta'} + \hat{\phi'})$, their counterparts in GCS are:

$$\begin{bmatrix} F_\theta(\theta, \phi) \\ F_\phi(\theta, \phi) \end{bmatrix} = \begin{bmatrix} \cos\psi & -\sin\psi \\ \sin\psi & \cos\psi \end{bmatrix} \begin{bmatrix} F'_\theta(\theta', \phi') \\ F'_\phi(\theta', \phi') \end{bmatrix}. \tag{2.19}$$

Here, ψ is the angular displacement between the spherical basis vectors of LCS and GCS and depends on $(\alpha, \beta, \gamma, \theta, \phi)$. It is calculated using

$$\psi = \angle\left(\hat{\theta} \cdot \mathbf{R} \cdot \hat{\theta}' + j\hat{\phi} \cdot \mathbf{R} \cdot \hat{\phi}'\right). \tag{2.20}$$

carrying $\hat{\theta}(\theta,\phi)$, $\hat{\phi}(\theta,\phi)$ and $\hat{\theta}'(\theta',\phi')$, $\hat{\phi}'(\theta',\phi')$ from Equação A.4.

This transformation correctly projects the antenna local polarization characteristics into the global frame, ensuring that the interaction between the antenna array and the incoming or outgoing waves is well-suited.

2.2.3 Phased Array

The core of the GS receiving system is the antenna array. An array architecture, as opposed to a single large antenna, allows for **spatial adaptive processing**, which is the intelligent

combination of signals received by multiple antenna elements. This approach provides significant advantages in performance, flexibility, and robustness, making it highly suitable for the demanding environment of satellite communications.

2.2.3.1 UPA Model

For this work, a UPA architecture is considered. In this configuration, the antenna elements are arranged on a two-dimensional grid. A specific and common case of the UPA is the Uniform Rectangular Array (URA), where the elements are placed in a rectangular grid with uniform spacing, as illustrated in Figura 2.5.

Figure 2.5. A URA arranged in the YZ-plane, with the reference origin at the lower-left corner.

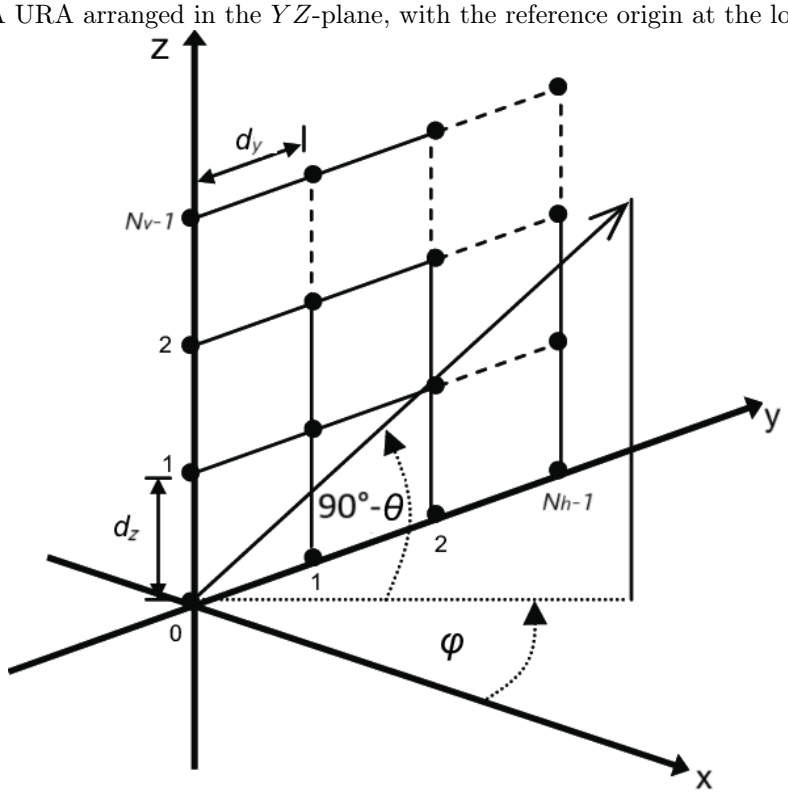

Source: (AGATONOVIĆ *et al.*, 2012).

A key advantage of a planar array is that its two-dimensional nature provides two Degrees of Freedom (DOF). This allows the array to resolve the signal DoA in both azimuth (ϕ) and zenith (θ), making the vector of angular parameters to be estimated $\mathbf{\Theta} = [\phi, \theta]$ (TONG *et al.*, 2022).

Taking the geometrical center of the array as the reference origin, the position vector

$$\mathbf{p}_n = [x_n \ y_n \ z_n]^T$$

for each element n can be described in spherical coordinates as stated in Equação A.2:

$$\begin{cases} x_n = & \|p_n\| \cos\phi \sin\theta \\ y_n = & \|p_n\| \sin\phi \sin\theta \\ z_n = & \|p_n\| \cos\theta. \end{cases} \tag{2.21}$$

This geometric model is the mathematical foundation for deriving the array steering vector, which is essential for all subsequent signal processing tasks, including beamforming and DOA estimation.

Array Factor

The total radiation pattern of an antenna array is determined by two key characteristics: the radiation pattern of the individual antenna elements and the spatial arrangement of those elements. For a general array of N elements, the total electric field, and hence its antenna pattern, is given by the sum of the contributions from each element multiplied by a complex phase associated with the signal wave direction and the elements' position:

$$\mathbf{F}_{total}(\mathbf{\Theta}) = \sum_{n=1}^{N} \mathbf{F}_n(\mathbf{\Theta}) w_n e^{j\mathbf{k}\cdot\mathbf{p}_n}, \tag{2.22}$$

where:

- $\mathbf{F}_n(\mathbf{\Theta})$ is the antenna pattern of the n-th antenna. It can be obtained at the Subseção 2.2.1.
- w_n is the complex excitation weight (amplitude and phase) applied to the n-th element.
- $\mathbf{p}_n$ is the position vector of the n-th element.
- $\mathbf{k}$ is the wave vector, which points in the direction of propagation $\mathbf{\Theta}$ and has a magnitude of $k = 2\pi/\lambda$.

The dot product $\mathbf{k} \cdot \mathbf{p}_n$ represents the phase difference of the signal from the n-th element relative to the origin, in the direction (θ, ϕ).

The influence of the array geometry, including the element positions and the relative phasing of their signals, is captured by a function known as the Array Factor (AF). It represents the far-field radiation pattern of an array of isotropic point sources. It is a spatial weighting function that, when multiplied by the radiation pattern of a single element, gives the total radiation pattern of the array. This is known as the principle of **pattern multiplication** (BALANIS, 2016).

For an array with equal elements pointing to the same direction, the total far-field antenna pattern, $\mathbf{F}_{total}(\mathbf{\Theta})$, can be expressed as:

$$\mathbf{F}_{total}(\mathbf{\Theta}) = \underbrace{\mathbf{F}_{element}(\mathbf{\Theta})}_{\text{Element Pattern}} \underbrace{A(\mathbf{\Theta})}_{\text{Array Factor}} \tag{2.23}$$

The Array Factor is a scalar function that depends on the number of elements, their geometric layout, and the excitation (amplitude and phase) applied to each one:

$$A(\mathbf{\Theta}) = \sum_{n=1}^{N} w_n e^{j\mathbf{k}\cdot\mathbf{p}_n}. \tag{2.24}$$

Array Factor for a UPA

For a Uniform Planar Array UPA with $N = N_h \times N_v$ elements arranged in the YZ-plane (as described in the Figura 2.5), we can derive a more specific expression for the Array Factor. If we want to steer the main beam of the array to a specific direction (θ_0, ϕ_0), we apply a set of phase shifts to the elements. These phase shifts are encapsulated in the array **steering vector**.

The steering vector, $\mathbf{a}(\mathbf{\Theta})$, for the entire array is a column vector whose n-th element is the phase contribution from the n-th antenna element in the direction (θ, ϕ):

$$\mathbf{a}(\mathbf{\Theta}) = \begin{bmatrix} e^{j\mathbf{k}\cdot\mathbf{p}_1} \\ e^{j\mathbf{k}\cdot\mathbf{p}_2} \\ \vdots \\ e^{j\mathbf{k}\cdot\mathbf{p}_N} \end{bmatrix}. \tag{2.25}$$

To steer the beam to $\mathbf{\Theta}_0 = [\phi_0, \theta_0]$, the complex weights are chosen to be the conjugate of the steering vector in that direction, i.e., $w_n = e^{-j\mathbf{k}_0\cdot\mathbf{p}_n}$, where $\mathbf{k}_0$ is the wave vector for the steering direction. Substituting this into the general AF formula gives:

$$A(\mu_n) = \mathbf{w}\cdot\mathbf{a}(\mathbf{\Theta}) = \sum_{n=1}^{N} e^{-j\mathbf{k}_0\cdot\mathbf{p}_n} e^{j\mathbf{k}\cdot\mathbf{p}_n} = \sum_{n=1}^{N} e^{j\mu_n}, \tag{2.26}$$

in which $\mathbf{w} = [w_1 \ \cdots \ w_N]^T$, and $\mu_n = (\mathbf{k} - \mathbf{k}_0) \cdot \mathbf{p}_n$ is the spatial frequency.

For a URA in the YZ-plane with inter-element spacing d_y and d_z, the position of the element at the $(m,\, l)$-th position is $\mathbf{p}_{ml} = md_y\hat{\mathbf{y}} + ld_z\hat{\mathbf{z}}$. The Array Factor can then be written as the product of two one-dimensional array factors (TREES, 2002):

$$A(\mu_{ml}) = \left(\sum_{m=0}^{N_h-1} e^{jm(kd_y \sin\theta_n \sin\phi - kd_y \sin\theta_0 \sin\phi_0)} \right) \left(\sum_{l=0}^{N_v-1} e^{jl(kd_z \cos\theta - kd_z \cos\theta_0)} \right). \tag{2.27}$$

These are geometric series that can be summed to give the final closed-form expression for the UPA AF:

$$A(\mu_{ml}) = \frac{\sin\left(\frac{N_h}{2}\mu_y\right)}{\sin\left(\frac{1}{2}\mu_y\right)} \frac{\sin\left(\frac{N_v}{2}\mu_z\right)}{\sin\left(\frac{1}{2}\mu_z\right)}, \tag{2.28}$$

where $\mu_y = kd_y(\sin\theta \sin\phi - \sin\theta_0 \sin\phi_0)$ and $\mu_z = kd_z(\cos\theta - \cos\theta_0)$are the cartesian direction components of μ.

This Array Factor function precisely describes the spatial filtering characteristics of the UPA, showing how the array gain is distributed across different directions in space and how this distribution changes as the beam is steered.

Given the (2.10), it can be deduced from the (2.22) that the total power gain of an array of antennas, G_{tot}, is the superposition of the product of the n-th individual array factor and the element gain pattern, $G_n(\theta)$:

$$G_{tot}(\theta) = \left| \sum_{n=1}^{N} \sqrt{G_n(\theta)} e^{j\mu_n} \right|^2, \tag{2.29}$$

when all antennas are equal and point to the same direction (i.e. $G_n(\theta) = G(\theta)$, $\forall n$), (2.29) follow the same fashion of (2.23):

$$G_{tot}(\theta) = |A(\mu_n)|^2 G(\theta). \tag{2.30}$$

2.2.3.2 Uniform Linear Array

A Uniform Linear Array (ULA) is a one-dimensional antenna array and can be considered a simplified special case of the UPA discussed previously. In a ULA, the antenna elements are arranged along a single straight line with uniform spacing between them. This simpler geometry reduces the complexity of signal processing but also limits the array capabilities.

In a ULA with N elements aligned along the Z-axis, the position vector, $\mathbf{p}_n$, of the n-th element can be described as:

$$\mathbf{p}_n = nd_z\hat{\mathbf{z}}, \quad \text{for } n = 0, 1, \ldots, N-1, \tag{2.31}$$

where d_z is the inter-element spacing.

Unlike the two-dimensional UPA, which has two DOF and can resolve the signal direction in both azimuth and zenith, the one-dimensional ULA has only one DOF. This means it can unambiguously determine the angle of arrival only in the plane that contains the array axis (e.g., the zenith angle, θ), assuming the other angular parameter is known or is not relevant (TREES, 2002).

Array Factor for a ULA

The AF for a ULA is a simplification of the UPA AF. The total radiation pattern is still determined by the principle of pattern multiplication, where the total pattern is the product of the element pattern and the array factor.

The steering vector, $\mathbf{a}(\theta)$, for a ULA along the Z-axis depends only on the zenith angle θ:

$$\mathbf{a}(\theta) = \begin{bmatrix} 1 \\ e^{jkd\cos\theta} \\ \vdots \\ e^{j(N-1)kd\cos\theta} \end{bmatrix}. \tag{2.32}$$

To steer the main beam to a direction θ_0, the complex weights w_n are chosen to cancel the phase progression from that direction, i.e., $w_n = e^{-jknd\cos\theta_0}$. The resulting AF becomes:

$$A(\mu_n) = \sum_{n=0}^{N-1} e^{jknd(\cos\theta - \cos\theta_0)} = \sum_{n=0}^{N-1} (e^{j\mu_z})^n, \tag{2.33}$$

where the phase difference term μ_z is given by

$$\mu_z = kd(\cos\theta - \cos\theta_0). \tag{2.34}$$

This geometric series can be summed to obtain the closed-form expression:

$$A(\mu_n) = \frac{\sin\left(\frac{N}{2}\mu_z\right)}{\sin\left(\frac{1}{2}\mu_z\right)}. \tag{2.35}$$

This function describes the spatial filtering characteristics of the ULA, defining the main beam and sidelobe structure as a function of the zenith angle. While simpler to analyze and implement, the ULA inability to resolve the full 3D direction of arrival makes the UPA a more suitable choice for satellite tracking applications.

2.2.3.3 Grating Lobes

An ideal antenna array would channel all its radiated energy into a single, narrow main beam pointed in the desired direction. However, in practice, the discrete nature of the array and the physical spacing between its elements can give rise to unwanted replicas of this main beam at other angles. These replicas are known as **grating lobes**, as discussed in the Section 1.2.4. Their appearance is a significant problem that can severely degrade the performance of an array, particularly for systems requiring high precision, such as satellite tracking.

Grating lobes are a direct consequence of spatial aliasing. This phenomenon occurs when the antenna elements are spaced too far apart relative to the wavelength λ of the signal being transmitted or received. The critical spacing is half a wavelength ($\lambda/2$). When the inter-element spacing, $d_{y,z}$, exceeds this value, the array can no longer unambiguously determine the direction of an incoming wave (BALANIS, 2016).

Figure 2.6. Grating lobes on antenna pattern. On the top side, spacing of $\lambda/2$ (100% of visibility). On the bottom side, spacing of λ (200% of visibility, generating 1 replica).

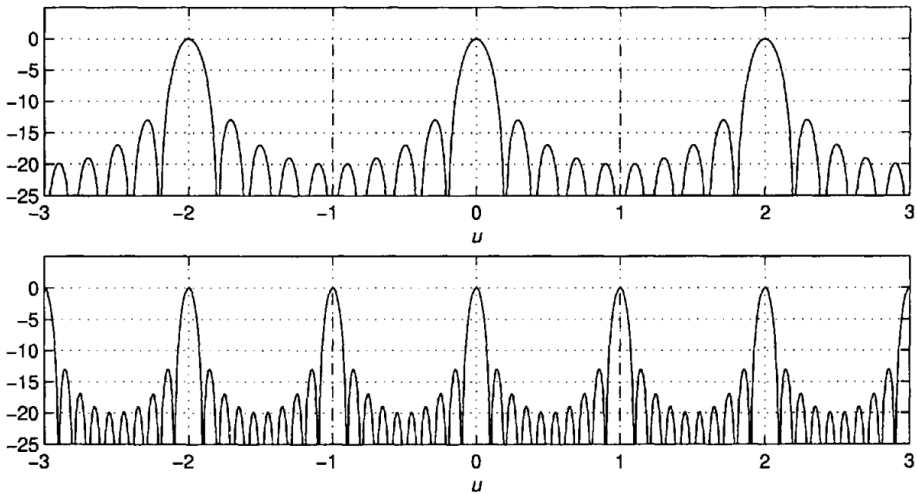

Source: (TREES, 2002).

Mathematically, the direction of the main beam (θ_0) and the grating lobes (θ_g) for a ULA

can be found from the (2.35). Maxima occurs when the argument of the sine functions in the denominator is a multiple of π. For a beam steered to boresight ($\theta_0 = 90°$ for an array on the Z-axis), the grating lobes will appear at angles θ_g that satisfy:

$$kd\cos\theta_g = \pm 2\pi m, \quad \text{for } m = 1, 2, 3, \ldots \tag{2.36}$$

A real solution for θ_g (i.e., a visible grating lobe) will exist if $|\frac{m\lambda}{d}| \leq 1$. For the first grating lobe ($m = 1$), this condition becomes $d \geq \lambda$. If the beam is steered away from boresight, the condition becomes even stricter, and grating lobes can appear even when the spacing is less than a full wavelength (TREES, 2002).

2.3 SIGNAL MODEL

To analyze and develop the signal processing algorithms for the GS, it is imperative to first establish a mathematical model of the communication signal. This section details the end-to-end signal model for the LEO satellite digital communication system, tracing the path of the information from its initial digital form to the final baseband waveform received by the antenna array. The model encompasses the key stages of digital signal preparation required for transmission over a bandlimited Low Earth Orbit (LEO) satellite channel.

2.3.1 Bit to Symbol Assignment

In a digital communication system, the process of transmitting information begins with the **baseband signal**. This signal represents the original data, such as a stream of binary digits, in its unprocessed, unmodulated form. In the context of LEO satellite communications, the lowpass signal is the foundation of the information that is prepared on the ground before being modulated onto a high-frequency carrier wave for its journey to the satellite.

The raw information from a source is typically a sequence of bits. To improve bandwidth efficiency, these bits are grouped together to form **symbols**. A group of k bits can represent one of $M = 2^k$ possible symbols. This mapping process is known as symbol assignment. This grouping creates a distinction between the **bit rate** and the **symbol rate**:

- Bit Rate (R): This is the rate at which the original information bits are transmitted, measured in bits per second (bps).
- Symbol Rate (R_s): Also known as the baud rate, this is the rate at which symbols are transmitted, measured in symbols per second (or baud).

The relationship between the two is given by:

$$R_s = \frac{R}{k} = \frac{R}{\log_2 M}. \tag{2.37}$$

Each symbol, of duration $T_s = \frac{1}{R_s}$, is transmitted using a pulse p(t), shaped to fit within the available bandwidth and time slot. The transmitted baseband signal can be modeled as:

$$s_{bb}(t) = \sum_{k=-\infty}^{\infty} a_k p\left(t - kT_s\right), \tag{2.38}$$

where a_n are the symbol amplitudes that depend on the modulation scheme.

Pilot Signal

In digital communication systems, particularly those operating over dynamic and challenging channels like a LEO satellite link, it is often necessary for the transmitter to send known reference signals to assist the receiver in its demodulation and decoding tasks. These known signals are referred to as pilot signals or pilot sequences.

A pilot signal is a deterministic waveform, known in advance by both the transmitter and the receiver, which is embedded into the data stream at the baseband level. The receiver can exploit its knowledge of the pilot structure to perform several critical functions:

- Carrier Phase and Frequency Recovery: The high velocity of LEO satellites induces a significant and rapidly changing Doppler shift, which can cause a loss of phase coherence. The receiver can compare the received pilot signal with its known, ideal version to accurately estimate and track this phase and frequency offset, allowing for robust carrier recovery.
- Timing Synchronization: Pilot signals with specific, known patterns can be used to achieve precise symbol timing synchronization. The receiver can correlate the incoming signal

with the known pilot sequence to find the exact start of a data frame or to fine-tune its sampling clock.

- Channel Estimation: By observing how the channel distorts the known pilot signal, the receiver can estimate the channel current state, including its amplitude and phase response. This channel state information can then be used to equalize the received data signal, mitigating the effects of fading and other distortions.

Pilot signals are typically inserted into the baseband signal in two ways:

1. Preamble/Unique Word: For burst-mode transmissions (common in TDMA systems), a known sequence of symbols, often called a preamble or a unique word, is appended to the beginning of each data burst.

2. Distributed Pilots: For continuous transmissions, pilot symbols or tones can be scattered throughout the data stream at regular intervals in time and/or frequency.

The use of pilot signals represents a trade-off between performance and efficiency. While they consume a portion of the available power and bandwidth that could otherwise be used for data, the significant improvements they provide in synchronization and channel estimation are often essential for achieving reliable communication, especially in the demanding environment of a LEO satellite link.

ISI Problem

Every communication channel, including the satellite link, is bandlimited, meaning it can only pass a certain range of frequencies. When a sequence of sharp, distinct pulses (representing symbols) is transmitted through such a channel, the channel filtering effect causes the pulses to spread out or "smear"in time.

This temporal spreading causes the energy from one pulse to spill over into the time slots of adjacent pulses. At the receiver, when sampling the signal to detect a specific symbol, the measurement is corrupted by the residual energy from these neighboring symbols. This phenomenon is known as ISI, and it is a major source of errors in digital communication

systems, as it can cause the receiver to misinterpret the received symbol (PROAKIS; SALEHI, 2008).

To eliminate ISI, the overall pulse shape must conform to the **Nyquist criterion**. This criterion states that for zero ISI, the impulse response of the end-to-end system, $h(t)$, must have the property that it is zero at all k integer multiples of the symbol period, T_s, except for $k = 0$. It yields:

$$h(kT_s) = \begin{cases} 1, & k = 0 \\ 0, & k \neq 0. \end{cases} \tag{2.39}$$

A pulse that meets this condition will have zero crossings at the exact sampling instants of all other symbols, ensuring that they do not interfere with the current symbol measurement. This means that at the center of any given symbol interval, the contribution from all other symbols is exactly zero.

2.3.2 Pulse Shaping

In a practical digital communication system, transmitted pulses must be shaped to fit within a limited channel bandwidth. An ideal rectangular pulse has an infinite bandwidth (its Fourier transform is a sinc function), making it unsuitable for real-world channels. While an ideal "brick-wall"filter would provide the narrowest possible bandwidth for a given symbol rate without causing interference, such a filter is not physically realizable. A practical and widely implemented solution to this problem is the **raised-cosine filter**.

The primary purpose of the raised-cosine filter is to create a pulse shape that has a finite bandwidth and, critically, results in **zero ISI** at the ideal sampling instants $t = nT_s$. The frequency response of a raised-cosine filter is characterized by a flat amplitude portion and a roll-off section that smoothly tapers to zero. Its frequency response, $P(f) = \int_{-\infty}^{\infty} p(t)e^{-\jmath 2\pi ft}dt$, is defined in three parts (SKLAR, 2020):

$$P(f) = \begin{cases} T_s, & 0 \leq |f| \leq \frac{1-b}{2T_s} \\ \frac{T_s}{2}\left[1 + \cos\left(\frac{\pi T_s}{b}\left[|f| - \frac{1-b}{2T_s}\right]\right)\right], & \frac{1-b}{2T_s} < |f| \leq \frac{1+b}{2T_s} \\ 0, & |f| > \frac{1+b}{2T_s} \end{cases} \tag{2.40}$$

The **roll-off factor**, $b \in [0, 1]$, determines the "excess bandwidth"of the filter beyond the theoretical minimum Nyquist bandwidth of $1/(2T_s)$. An $b = 0$ corresponds to the ideal unrealizable

brick wall filter, while $b = 1$ corresponds to a filter that uses 100% excess bandwidth (i.e., double the Nyquist bandwidth).

The time-domain impulse response, $p(t) = \int_{-\infty}^{\infty} P(f)e^{j2\pi ft}df$, corresponding to this frequency response is a sinc pulse multiplied by another cosine term:

$$p(t) = \frac{\sin(\pi t/T_s)}{\pi t/T_s}\frac{\cos(b\pi t/T_s)}{1-(2bt/T_s)^2}. \tag{2.41}$$

It is illustrated in Figure 2.7.

Figure 2.7. Raised cosine pulse $p(t)$ vesus time (sec).

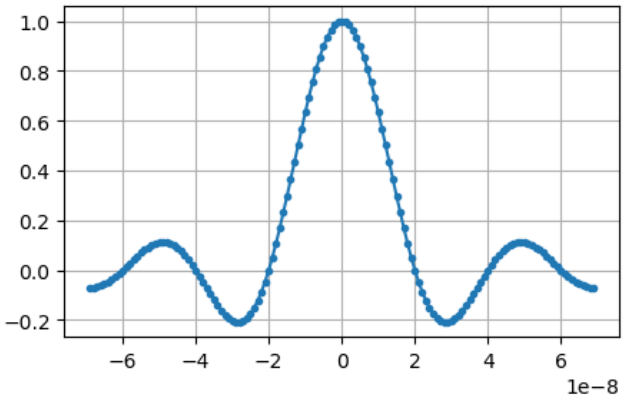

Source: Own authorship.

ISI due to Symbol Asynchrony

The zero-ISI property of the raised-cosine pulse holds true only if the receiver samples the incoming waveform at the exact, ideal moments in time. In any real system, perfect timing is impossible to achieve as mentioned in the Section 1.2.5, and there will always be some degree of **symbol asynchrony** or **timing jitter**.

If the receiver sampling clock is not perfectly synchronized with the incoming symbols, i.e. offset by a small amount Δt, the samples will be taken slightly before or after the ideal point, at $t = kT_s + \Delta t$. At these offset times, the raised-cosine pulses from adjacent symbols do not have zero amplitude. Consequently, the sample for the desired symbol will be contaminated by non-zero contributions from its neighbors, re-introducing ISI into the system. The severity of this ISI is related to the roll-off factor, b; pulses with a smaller roll-off factor have longer-lasting tails and are more sensitive to timing errors (SKLAR, 2020). This highlights the critical

importance of robust symbol synchronization algorithms at the receiver to minimize timing errors and maintain a low BER.

2.3.3 Bandpass Modulation

In any digital communication system, the fundamental task is to map digital information - a sequence of bits - onto a physical waveform that can be transmitted efficiently over a channel. For Radio Frequency (RF) channels, such as a satellite link, this is achieved through **bandpass modulation**, where the baseband digital information is modulated onto a high-frequency carrier wave. A powerful and intuitive way to analyze and visualize this process is through the concept of **signal space** and its graphical representation, the **constellation diagram**.

The baseband signal is transformed into a passband waveform by modulating with a sinusoidal carrier f_0, resulting in:

$$s(t) = \mathrm{Re}\left\{ s_{\mathrm{bb}}(t) \cdot e^{\jmath 2\pi f_0 t} \right\}, \tag{2.42}$$

where $s_{\mathrm{bb}}(t)$ is the complex baseband equivalent of the modulated signal.

In digital communication, signals can be modeled as vectors in a signal space where each symbol corresponds to a unique waveform or **signal point**. The set of these points forms the constellation diagram. This representation enables Geometric interpretation of modulation schemes, distance-based error analysis with Euclidean distance, and in addition to design of optimal receivers (e.g., minimum distance decision rule).

For a signal set $\{s^1(t), s^2(t), \ldots, s^M(t)\}$, we define each unique symbol $s^m(t)$ as a linear combination of orthonormal basis functions $\{\varphi_1(t), \varphi_2(t)\}$:

$$s^m(t) = s_1^m \varphi_1(t) + s_2^m \varphi_2(t). \tag{2.43}$$

This corresponds to a 2D vector $\mathbf{s}^m = [s_1^m \; s_2^m]$ in signal space. The coordinates of this vector are the projections of the signal onto each basis function. The distance between symbols in this space determines the symbol error probability.

For bandpass modulation, the most common basis functions are two quadrature carriers:

$$\varphi_1(t) = \sqrt{\frac{2}{T_s}} \cos(2\pi f_0 t) \text{ and } \varphi_2(t) = \sqrt{\frac{2}{T_s}} \sin(2\pi f_0 t), \tag{2.44}$$

where f_0 is the carrier frequency. These two basis functions, the **in-phase** (I) and **quadrature** (Q) components, are orthogonal and form a two-dimensional signal space.

Different modulation schemes are distinguished by how they arrange the points in the constellation.

- Phase Shift Keying (PSK): the information is encoded in the phase of the carrier wave, while the amplitude is kept constant. This means all constellation points lie on a circle centered at the origin.
- Quadrature Amplitude Modulation (QAM): encodes information in both the amplitude and the phase of the carrier. This allows for more points to be placed in the constellation, typically in a square or rectangular grid, enabling higher data rates.

Each point represents a unique **bit group**, and the **decision boundaries** in the signal space define the region in which each symbol is detected. The geometry of the signal constellation is directly related to the system performance in the presence of noise. When a signal is transmitted, channel noise adds a random component to the received vector, causing the received point to land in a "cloud"around the ideal constellation point. The receiver task is to decide which of the M possible symbols was transmitted based on the noisy received point (SKLAR, 2020).

2.3.3.1 QPSK

QPSK, sometimes called 4-PSK, is a widely used bandpass modulation technique that offers a significant improvement in bandwidth efficiency over its simpler counterpart, Binary PSK (BPSK). It achieves this by encoding two bits of data into each transmitted symbol (00, 01, 10, 11), thereby doubling the data rate for the same symbol rate (and thus, the same bandwidth).

QPSK is a form of phase modulation where the carrier signal can take one of four possible phase shifts, with each phase representing a unique dibit. In the signal space representation, this results in a constellation with four points, equally spaced on a circle of constant radius (amplitude) around the origin. The four phases are typically chosen to be $\theta_m \in \left\{\frac{\pi}{4}, \frac{3\pi}{4}, \frac{5\pi}{4}, \frac{7\pi}{4}\right\}$,

as shown in Figure 2.8.

Figure 2.8. On the left,QPSK Constellation Diagram ($\varphi_1(t)$ versus $\varphi_2(t)$). There is a set of $M = 4$ possible points for the symbol $\mathbf{s}^m$. On the right, the symbols are deteriorated with additive noise.

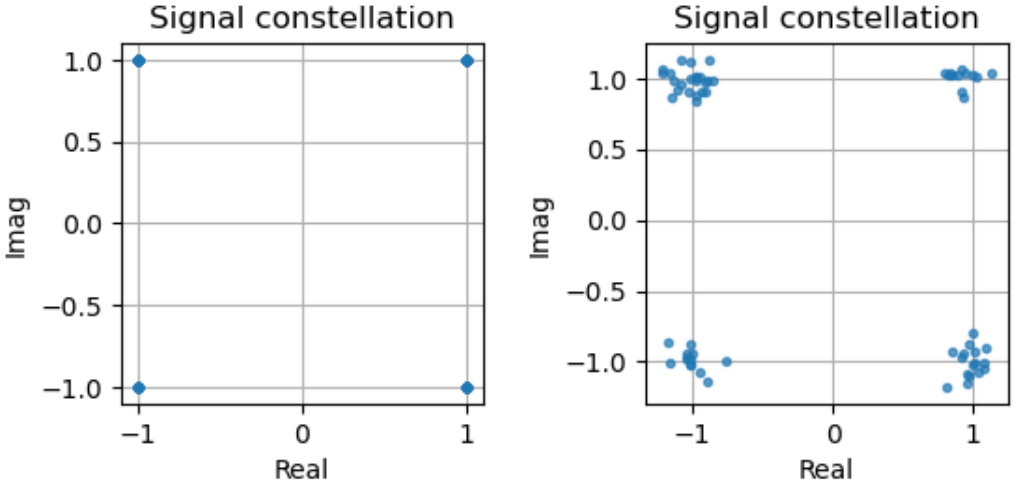

Source: Own authorship.

A crucial aspect of the symbol mapping in QPSK is the use of **Gray coding**. As seen in Figura 2.8, the bit-to-symbol assignment is arranged such that any two adjacent constellation points differ by only one bit. This is a significant advantage because the most likely errors caused by noise will be mistaking a symbol for an adjacent one. With Gray coding, such a symbol error will result in only a single bit error, which minimizes the overall BER of the system (SKLAR, 2020).

A QPSK signal can be mathematically represented as the sum of two orthogonal basis functions as explained in Subseção 2.3.3. The general form of the transmitted signal for the m-th symbol is:

$$s^m(t) = p(t)\cos(2\pi f_0 t + \theta_m), \quad \text{for } m = 1, 2, 3, 4, \tag{2.45}$$

where $p(t)$ is the signal pulse amplitude and θ_m is one of the four carrier phases. Using trigonometric identities, this can be expanded into its I and Q components:

$$s^m(t) = p(t)\cos(\theta_m)\cos(2\pi f_0 t) - p(t)\sin(\theta_m)\sin(2\pi f_0 t). \tag{2.46}$$

For the constellation shown in Figure 2.8, the values of $\cos(\theta_m)$ and $\sin(\theta_m)$ will be $\pm 1/\sqrt{2}$. This means the QPSK signal is effectively the sum of two BPSK signals, one on the in-phase carrier and one on the quadrature carrier. For instance, the incoming bit stream is divided

into two separate streams (one for the I channel and one for the Q channel), and each stream modulates its respective carrier with a BPSK-like signal ($+p(t)$ or $-p(t)$).

Looking in terms of the equations (2.38) and (2.42), in (2.45) $a_k = exp(\jmath\theta_k)$ hence considering pulses

$$s(t) = \mathrm{Re}\left\{ \sum_{k=-\infty}^{\infty} p\left(t - kT_s\right) e^{\jmath\theta_k} e^{\jmath 2\pi f_0 t} \right\}. \tag{2.47}$$

And its sampled version on each T_s instant is

$$s(kT_s) = \mathrm{Re}\left\{ \sum_{\nu=1}^{K} p\left[\left(k-\nu\right)T_s\right] e^{\jmath(\theta_\nu + 2\pi f_0 k T_s)} \right\},\ k = 1,2,\cdots,K, \tag{2.48}$$

for a signal with K pulses.

2.3.3.2 BER

The ultimate measure of performance for a digital communication system is how reliably it can deliver data from the source to the destination in the presence of channel impairments like noise and interference. The probability of making an error depends on the distance between the constellation points. A larger distance between points makes the system more robust to noise.

The most common metric for quantifying this reliability is the BER. It is defined as the ratio of the number of bit errors received to the total number of bits transmitted during a specific time interval. It is a direct measure of the end-to-end performance of the system. For example, a BER of 10^{-5} means that, on average, one bit is received in error for every 100.000 bits transmitted.

The BER is a function of the SNR, typically expressed as the ratio of energy per bit to noise power spectral density (E_b/N_0). For many common modulation schemes in an Additive White Gaussian Noise (AWGN) channel, the theoretical probability of a bit error (P_b) can be expressed using the Complementary Error Function (ERFC)

$$\mathrm{erfc}(x) = \frac{1}{\sqrt{2\pi}} \int_x^{\infty} e^{-t^2/2} dt. \tag{2.49}$$

Modulation schemes with more densely packed constellations, like higher-order QAM, require a higher E_b/N_0 to achieve the same BER as schemes with more sparsely spaced points, like BPSK (SKLAR, 2020).

QPSK BER Performance

As described previously, a QPSK signal can be viewed as two independent BPSK-modulated signals carried on quadrature carriers I and Q. Because these two channels are orthogonal, the noise in the I channel does not affect the Q channel, and vice versa.

Therefore, the P_b in the I channel is independent of the P_b in the Q channel. Since each channel carries half the total power and transmits at half the total data rate, the resulting bit error probability for the overall QPSK system is the same as it is for a BPSK system.

For coherent QPSK in an AWGN channel, assuming Gray coding (which minimizes bit errors per symbol error), the probability of bit error is given by:

$$P_b \approx \operatorname{erfc}\left(\sqrt{\frac{2E_b}{N_0}}\right). \tag{2.50}$$

Since the BER equations for BPSK and QPSK are identical, their theoretical performance curves are also identical. This means that for a given BER, QPSK requires the same E_b/N_0 as BPSK. They are equally power-efficient. QPSK encodes 2 bits per symbol, whereas BPSK encodes only 1 bit per symbol. This means that for the same T_s (which occupies the same bandwidth), QPSK has double the data rate and thus double the bandwidth efficiency of BPSK. Therefore, in summary, QPSK provides a significant advantage over BPSK by doubling the spectral efficiency without any penalty in power efficiency.

CHAPTER 3

SYSTEM MODEL

The electromagnetic wave that arrives at the ground station is a significantly transformed version of the signal originally transmitted by the satellite. Its journey through the vacuum of space and the Earth's atmosphere subjects it to a multitude of linear, time-varying, and stochastic processes that collectively define the satellite communication channel.

A mathematical model of this received signal is employed for designing and simulating the digital signal processing algorithms required for reliable communication (Section 3.1). This model accounts for any channel impairments that attenuate and corrupt the signal, the constantly changing propagation delay, and the spatial properties imposed by the antenna array at the receiver. Then the effects that compose it are described.

Channel issues such as atmospheric losses, fading and multipath effects were not the subject of this work, but they are addressed in Chapter B in the Appendix.

3.1 ARRAY RECEPTION MODEL

Consider a narrowband transmission of I signal sources received by a GS equipped with a UPA composed of $N = N_x \times N_y \geq I$ parabolic antennas. Each element of the array receives a delayed, Doppler-shifted, and attenuated version of the transmitted signal due to the satellite's position and motion. The received signal matrix $\mathbf{X} \in \mathbb{C}^{N \times K}$, with K samples, is modeled as

$$\mathbf{X} = \sum_{i=1}^{I} \alpha_i g(\theta_i)\ \mathbf{a}_i \mathbf{s}_i^T + \mathbf{W}, \tag{3.1}$$

where:

- $\alpha_i = \frac{\lambda}{4\pi D_i}$: Linearized Free-Space Path Loss (FSPL) coefficient - from (3.6) - for source i, with distance D_i.
- $g(\theta_i) = \sqrt{G(\theta_i)}$: Square-root antenna gain at arrival angle θ_i.

- $\mathbf{a}_i$: Steering vector, encoding the phase shift for each array element due to DoA $\mathbf{\Theta}_i = [\theta_i \ \phi_i]$.

- Complex "baseband"pilot signal from the satellite:

$$\mathbf{s}_i = \left[s(-\tau_i)e^{j\psi_0} \quad s(T_s - \tau_i)e^{j2\psi_1} \quad \cdots \quad s[(K-1)T_s - \tau_i]e^{j\psi_{K-1}}\right]^T, \tag{3.2}$$

  in which the delayed symbol pulse $s(kT_s - \tau_i)$ is multiplied by a array phase demodulation vestige $\psi_k = \Delta\mu_k + 2\pi f_d(kT_s)kT_s$, which includes the subcarrier mixing remaining $\Delta\mu_k$ phase (will be addressed in Section 4.1), and Doppler phase shift of (3.8), $2\pi f_d(k)kT_s$, being $f_d(k)$ the time-varying Doppler frequency.

- $\mathbf{W} \sim \mathcal{CN}(0, \sigma^2\mathbf{I}_N)$: A matrix of uncorrelated Complex AWGNs. $\mathbf{I}_N$ is the identity matrix of size N.

The steering vector is constructed as

$$\mathbf{a}_i = \left[e^{j\mu_i \cdot 0}, e^{j\mu_i \cdot 1}, \ldots, e^{j\mu_i \cdot (N-1)}\right]^T. \tag{3.3}$$

It describes the array's response to a plane wave arriving from a specific DoA $\Theta_i = (\theta_i, \phi_i)$ through the **spatial frequency** μ_i , and each element position $\mathbf{p}_n$, relative to the array's origin, contributes to the phase shift via:

$$\mu_i = \mathbf{p}_n \cdot \mathbf{k}(\theta_i, \phi_i). \tag{3.4}$$

Here, λ_i is the signal wavelength, and $\mathbf{k}(\theta_i, \phi_i)$ is the wave vector, which points in the direction of propagation and has magnitude $k_i = 2\pi/\lambda_i$.

The **array manifold matrix** $\mathbf{A} \in \mathbb{C}^{N \times I}$ is constructed by stacking the steering vectors of each source as $\mathbf{A} = [\alpha_1\mathbf{a}(\theta_1, \phi_1) \ \ldots \ \alpha_I\mathbf{a}(\theta_I, \phi_I)]$, $\mathbf{G} = \text{diag}([g(\theta_0) \ \cdots \ g(\theta_I) \ \ 1 \ \cdots \ 1])$ is a $N \times N$ gain matrix, and $\mathbf{S} = [\mathbf{s}_1 \ \cdots \ \mathbf{s}_I]^T$ is the pilot signal matrix.

Therefore, the overall signal in compact form is:

$$\mathbf{X} = \mathbf{GAS} + \mathbf{W}. \tag{3.5}$$

This model forms the basis for all necessary array processing techniques, such as adaptive beamforming and high-resolution DOA estimation, which are designed to exploit the spatial

structure captured by the manifold matrix to separate the desired signal from interference and noise.

3.2 PROPAGATION DELAY

The signal travels at the speed of light, resulting in a **propagation delay**, τ_i, between the satellite and the ground station, given by $\tau_i = D(t)/c$. For a LEO satellite, the distance $D(t)$ can vary significantly during a pass (e.g., from over 2000 km at the horizon to 500 km at zenith). This causes the propagation delay to be highly time-varying, which must be continuously tracked and compensated for by the receiver's synchronization circuits.

3.3 CHANNEL IMPAIRMENTS

As the signal propagates from the satellite to the ground station, it is degraded by a combination of phenomena that reduce its power, introduce random fluctuations, and add unwanted noise. These impairments are the primary factors limiting the performance of the communication link.

3.3.1 FSPL

The most fundamental and significant source of signal attenuation is the geometric spreading of the electromagnetic wavefront as it travels through space. This power reduction, known as FSPL, is a deterministic loss that depends only on the distance and frequency. The FSPL, expressed in decibels (dB), is given by the Friis transmission equation:

$$\alpha(\text{dB}) = 20\log_{10}(D(t)) + 20\log_{10}(f) + 20\log_{10}\left(\frac{4\pi}{c}\right), \tag{3.6}$$

where $D(t)$ is the distance between the satellite and the ground station in meters, f is the signal frequency in Hertz, and c is the speed of light in meters per second ($\approx 3 \times 10^8$ m/s).

For a LEO satellite, the distance d is not constant; it changes continuously throughout a pass, causing the path loss to be time-varying. The path loss is at its minimum when the satellite is at its highest elevation and maximum when it is on the horizon.

3.3.2 Doppler Shift Phase Effect

Due to satellite movement, the received carrier experiences Doppler shift of the (2.4), described in Section 2.1.6. This time-varying channel effect affects the phase of the received signal as

$$\varphi_d(t) = 2\pi \int_0^t f_d(\tau) d\tau, \tag{3.7}$$

compensating this phase shift is essential to preserve symbol integrity and coherent demodulation.

This phase shift can be modeled in the i-th received baseband signal $\mathbf{s}_i$ sampled at T_s instant, considering a time delay τ_i, as

$$\mathbf{s}_i = \begin{bmatrix} s(-\tau_i)e^{j2\pi f_d(0)\cdot 0T_s} \\ s(T_s - \tau_i)e^{j2\pi f_d(T_s)\cdot 1T_s} \\ \vdots \\ s[(K-1)T_s - \tau_i]e^{j2\pi f_d[(K-1)T_s](K-1)T_s} \end{bmatrix}, \tag{3.8}$$

with K samples.

3.3.3 System Noise

All electronic components in the receiver generate random noise due to the thermal agitation of electrons. The total noise power, P_N, added to the signal at the receiver is given by:

$$P_N = k_b T_{sys} B, \tag{3.9}$$

where:

- k_b is Boltzmann's constant (1.38×10^{-23} J/K).
- B is the receiver's noise bandwidth in Hertz.
- T_{sys} is the **equivalent system noise temperature** in Kelvin. This is a critical figure of merit for a receiver and is the sum of the noise contributions from all components in the receive chain, referred to the input of the receiver. It primarily consists of the antenna noise temperature (T_A), which accounts for noise from the sky and ground picked up by the antenna, and the noise temperature of the Low-Noise Amplifier (LNA) and subsequent stages.

This noise is typically modeled as AWGN, a random signal with a flat power spectral density N_0 across the frequency band of interest and a complex Gaussian amplitude distribution of zero mean, added independently to each received sample:

$$\mathbf{W}_{n,k} \sim \mathcal{CN}(0, \sigma^2), \tag{3.10}$$

in which the variance is related to the noise power, i.e. $\sigma^2 = P_w$.

CHAPTER 4

PROPOSED ARCHITECTURE

The raw signal captured by the GS's antenna array is a faint and distorted version of the information transmitted by the LEO satellite. To recover the original message with high fidelity, a chain of signal processing techniques must be applied. This chapter details the key algorithms employed in this work to acquire, synchronize, and enhance the received signal, as shown in the Figure 4.1. The process begins with the initial signal acquisition, which relies on a priori knowledge from the satellite, and culminates in the spatial filtering and symbol synchronization of the array's signal to reconstruct the desired data stream.

Figure 4.1. Transmitted signal flow DSP chain.

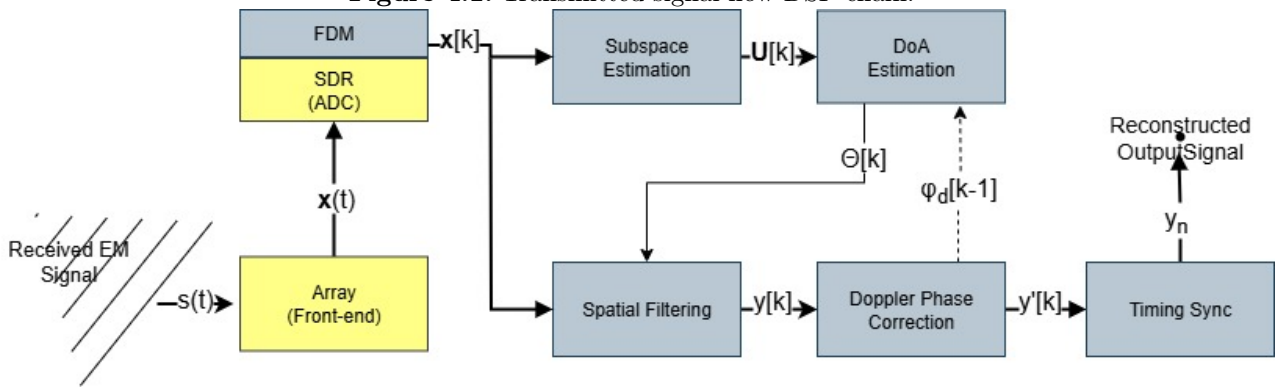

Source: Own authorship.

For proper signal acquisition, it is assumed that the satellite metadata is available to the GS. This includes orbital data (such as TLE sets) for a specific time stamp, which allows for the initial pointing of the array and prediction of the Doppler shift. It is also assumed that the structure of the pilot signals is known, and that key link budget parameters are available to the receiver. Furthermore, it will be supposed that the known pilot sequences are located in the preamble of the baseband message frame, allowing for initial synchronization and channel estimation. Due to the scope of this work, it is worth noting that noise is modeled as AWGN, and signal sources are not correlated.

The raw, digitized I/Q data streams from each antenna element are obtained through the channels of a Software-Defined Radio (SDR). SDRs are highly flexible radio systems where components that are typically implemented in hardware (e.g., mixers, filters, modulators, demodulators) are instead implemented by means of software on a personal computer or embedded system. In this application, a multi-channel SDR front-end is used to downconvert the RF signal from each antenna element to baseband. The signals are then digitized by high-speed Analog-to-Digital Converters (ADCs). The resulting streams of complex samples are then fed into the main processing unit where the following algorithms are executed in software, providing immense flexibility for implementing and testing the various techniques. Once digitized by the SDRs, the signals from the multiple antenna elements of the UPA are made available as input data streams to the digital processing chain (MITOLA, 2000).

4.1 FREQUENCY DIVISION MULTIPLEXING

A significant challenge in using a large-spaced (i.e., $d_{x,y} > \lambda/2$) uniform array is the inevitable appearance of grating lobes in its radiation pattern. It has already been mentioned in the Section 1.2.4 that this is a highly deleterious effect, as it introduces ambiguity that can corrupt DoA estimation and degrade the performance of beamforming algorithms.

This section describes the use of FDM as a method for mitigating grating lobes in large-spaced arrays by introducing controlled frequency offsets across antenna elements. While the following analysis is presented for a ULA with array spacing d for clarity. The arguments developed are analogous for a UPA setup. To counteract the grating lobe effect, this work proposes a novel technique that, in the demodulation stage of the RF chain, assigns a unique subcarrier frequency f_n to each array element n. This is a form of FDM, where the frequency for each element is defined as:

$$f_n = f_0 + \Delta f_n, \tag{4.1}$$

where f_0 is the nominal carrier frequency and Δf_n is the subcarrier spacing.

This approach can be seen as a method to emulate a non-uniform array in the signal processing domain. Instead of physically varying the inter-element spacing $d_{y,z}$, which remains fixed,

the spatial frequency μ_n is made non-uniform by introducing the term Δf_n:

$$\mu_n = \frac{2\pi d}{c}(f_0 + \Delta f_n)\cos\theta, \tag{4.2}$$

knowing that the wavelength is $k_n = \frac{2\pi}{\lambda_n} = \frac{2\pi f_n}{c}$.

Then, the array factor of the (2.33) then becomes dependent on this frequency progression:

$$A(\mu_n) = \sum_{n=0}^{N-1} w_n e^{j\frac{2\pi d\cos\theta}{c}(f_0+\Delta f_n)}. \tag{4.3}$$

The strategy is to select a value for each Δf_n that forces the radiation pattern of the large-spaced array to approximate the ideal pattern of an array that satisfies the Nyquist criterion for spacing, i.e., $d = \lambda/2$. For an ideal ULA (with a fixed frequency $f_n = f_0$ and uniform weights $w_n = 1$), the array factor is of the (2.35):

$$A(\mu_{\text{opt}}) = \sum_{n=0}^{N-1} e^{jn\pi\cos\theta} = \frac{\sin(\frac{N}{2}\pi\cos\theta)}{\sin(\frac{1}{2}\pi\cos\theta)}. \tag{4.4}$$

By carefully choosing Δf_n, the goal is to make the power pattern of the FDM-based large-spaced array approximate the ideal power pattern, thereby suppressing the grating lobes:

$$|A(\mu_{\text{n}})|^2 \approx |A(\mu_{\text{opt}})|^2. \tag{4.5}$$

The approach is particularly advantageous because it does not require mechanical adjustments or additional hardware, only frequency configuration at the SDR demodulation stage. Thus, this method enhances array processing resolution without compromising spatial or hardware constraints, making it viable for compact, modular ground station designs.

However, it should be noted that this scheme yields a higher system bandwidth occupancy. The total bandwidth of signal covers since the band B of the lower frequency subcarrier f_n until the which of high frequency, hence it can be estimated as:

$$B_{\text{Total}} = \max\left(f_n + \frac{B}{2}\right) - \min\left(f_n - \frac{B}{2}\right) = \max(f_n) - \min(f_n) + B. \tag{4.6}$$

4.1.1 Fixed separation

For the initial scope of this work, we investigate configurations where a fixed frequency separation Δf is maintained between adjacent subcarriers. In this scheme, the frequency offset

for each subcarrier of (4.1) is linearly related by the expression

$$\Delta f_n = n\Delta f \tag{4.7}$$

for a ULA,where n is the subcarrier index. Consequently, the total required bandwidth, as defined in (4.6), can be simplified to

$$B_{\text{Total}} = n\Delta f + B. \tag{4.8}$$

This linear arrangement significantly simplifies the allocation of frequency resources. Furthermore, for this specific configuration, an empirical relationship was observed between the required frequency separation Δf and the physical spacing d between antenna elements. Through simulation, it was verified that for element spacings that are not excessively large [1], a linear relationship exists. Therefore, it can be stated that the necessary frequency separation is directly proportional to the element spacing:

$$\Delta f \propto d. \tag{4.9}$$

4.2 SUBSPACE ANALYSIS

High-resolution DoA estimation algorithms such as MUSIC and ESPRIT are founded on the principle of subspace analysis. This approach exploits the spatial diversity of the signal received in the antenna array, partitioning the N-dimensional observation space $\mathbf{U}$ into two fundamental, orthogonal components: the signal subspace $\mathbf{U}_s$, which contains the energy from the sources of interest, and the noise subspace $\mathbf{U}_w$. By identifying these subspaces, it becomes possible to estimate the signals' parameters. This section details two methods for performing this matrix decomposition: the classic SVD and the adaptive PAST algorithm.

4.2.1 SVD

The SVD is a powerful matrix factorization technique that provides a robust, non-iterative method for identifying the signal and noise subspaces from a block of received data. The incoming RF signal is mixed with the (aided) local oscillators frequency to downconvert it to baseband.

[1] successful tests were conducted for spacings up to 4λ

The process begins by analyzing the received signal matrix $\mathbf{X} \in \mathbb{C}^{N \times K}$ of the (3.5), where N is the number of antenna elements and K is the number of samples collected. By treating this data as a realization of a stochastic process, we can estimate its spatial correlation matrix. Assuming the process is asymptotically uncorrelated, the correlation matrix can be approximated by the sample covariance matrix (HAYKIN, 2014):

$$\mathbf{R} \triangleq E[\mathbf{X}\mathbf{X}^H] \approx \frac{1}{K}\mathbf{X}\mathbf{X}^H. \tag{4.10}$$

$E[\mathbf{X}] = \sum_{n=0}^{N-1} \mathbf{x}_n p_n$ is the expected value of X, with $\mathbf{x}_n$ being its n-th row, and p_n the respective probability of $\mathbf{x}_n$.

The approximation by the right side of the (4.10) is reasonable under the Law of Large Numbers, provided that the number of samples K is sufficiently large compared to the number of signal sources I ($K \gg I$) (ANDERSON, 1963). The structure of this matrix, assuming uncorrelated AWGN, can be decomposed as

$$\mathbf{R} = \mathbf{A}\mathbf{R}_s\mathbf{A}^H + P_w\mathbf{I}_N, \tag{4.11}$$

where $\mathbf{R}_s = E[\mathbf{S}\mathbf{S}^H]$ is the signal correlation matrix and P_w is the noise power. The eigenvectors of this matrix $\mathbf{R}$ form the basis for the observation space. It is also worth noting that $P_w\mathbf{I}_N = \mathbf{R}_w$ is the noise correlation matrix.

Instead of performing an eigendecomposition on the estimated covariance matrix, it is often more numerically stable to apply the SVD directly to the data matrix $\mathbf{X}$:

$$\mathbf{X} = \mathbf{U}\mathbf{\Sigma}\mathbf{V}^H, \tag{4.12}$$

where $\mathbf{U} \in \mathbb{C}^{N \times N}$ and $\mathbf{V} \in \mathbb{C}^{M \times M}$ are unitary matrices, and $\mathbf{\Sigma} \in \mathbb{C}^{N \times M}$ is a diagonal matrix of singular values. A direct parallel can be drawn here: the columns of the matrix $\mathbf{U}$ (the left singular vectors of $\mathbf{X}$) are the eigenvectors of the sample covariance matrix $K\mathbf{R} = \mathbf{X}\mathbf{X}^H$(STRANG, 2010).

Therefore, the matrix $\mathbf{U}$ provides a basis for the total subspace of the received signal. If there are I incident signals, the I largest singular values in $\mathbf{\Sigma}$ will correspond to the signal energy, and the remaining $N - I$ smaller singular values will correspond to the noise floor. This allows for the partitioning of the total space:

- Signal Subspace ($\mathbf{U}_s$): This subspace is spanned by the I columns of $\mathbf{U}$ corresponding to the I largest singular values.
- Noise Subspace ($\mathbf{U}_n$): This subspace is spanned by the remaining $N - I$ columns of $\mathbf{U}$ and is orthogonal to the signal subspace.

4.2.2 PAST

While SVD is robust, its computation on the entire data matrix is a block-based process with a high computational complexity, typically on the order of $\mathcal{O}(N^3)$ (YANG, 1995). For a non-stationary system, such as tracking a moving LEO satellite, the signal subspace is constantly changing. Re-computing the full SVD for each new block of data is inefficient.

The PAST algorithm offers an adaptive and computationally efficient alternative. It is an iterative method that updates the estimate of the signal subspace with each new incoming reception snapshot $t \in \mathbb{N}$. This makes it highly suitable for tracking time-varying signals (BADEAU *et al.*, 2003).

PAST works by sequentially minimizing a cost function associated with the covariance matrix, effectively tracking its principal components over time. A key advantage is that it reuses information from previous estimates, using a forgetting factor, ξ, to weigh new information more heavily. This allows it to adapt to changes in the signal environment.

The steps for the real-time updating of the signal subspace $\mathbf{U}_s(t)$ based on new signal snapshots Let $\mathbf{X}_n(t)$ be the n-th row vector of $\mathbf{X}(t)$ are the following (BADEAU *et al.*, 2003):

1. Initialization ($t = 0$):

$$\mathbf{U}_s(0) = \begin{bmatrix} \mathbf{I}_I \\ \mathbf{0}_{(N-I)\times I} \end{bmatrix}, \quad \mathbf{Z}(0) = \mathbf{I}_I, \tag{4.13}$$

   with:

   - $\mathbf{U}_s(0)$: Initial guess of signal subspace.
   - $\mathbf{Z}(0)$: Auxiliary matrix for computation.

2. Recursive Update Equations:

Given $\mathbf{X}_n(t)$ being the n-th column vector of $\mathbf{X}(t)$ and defining the input snapshot vector $\mathbf{x}(t) = \sum_{n=0}^{N} \mathbf{X}_n(t)$ and the forgetting factor $\xi \in (0,1)$:

$$\begin{aligned}
\mathbf{y}(t) &= \mathbf{U}_s(t-1)^H \mathbf{x}(t) \\
\mathbf{h}(t) &= \mathbf{Z}(t-1)\mathbf{y}(t) \\
\gamma(t) &= \frac{1}{\xi + \mathbf{h}(t)^H \mathbf{y}(t)} \\
\mathbf{g}(t) &= \gamma(t)\mathbf{h}(t) \\
\mathbf{Z}(t) &= \frac{1}{\xi}\left(\mathbf{Z}(t-1) - \mathbf{g}(t)\mathbf{h}(t)^H\right) \\
\mathbf{e}(t) &= \mathbf{x}(t) - \mathbf{U}_s(t-1)\mathbf{y}(t) \\
\mathbf{U}_s(t) &= \mathbf{U}_s(t-1) + \mathbf{e}(t)\mathbf{g}(t)^H.
\end{aligned} \tag{4.14}$$

Another significant advantage is its reduced complexity. By only estimating the I-dimensional signal subspace, $\mathbf{U}_s(t)$, the PAST algorithm achieves a linear complexity of $\mathcal{O}(NI)$ per t update, which is far more efficient than the full SVD, especially when the number of sources I is much smaller than the number of antennas N. Although it is a suboptimal technique compared to the full SVD on a stationary signal, its adaptive nature and efficiency are highly desirable for real-time tracking applications. These facts are summarized in Table 4.2.2.

Table 4.1. Comparison of subspace techniques.

Technique	**Pros**	**Cons**	**Complexity**
SVD	Accurate, well-established	High computational cost	$\mathcal{O}(N^3)$
PAST	Adaptive, low-latency	Suboptimal accuracy	$\mathcal{O}(NI)$

Source: (BADEAU *et al.*, 2003).

For algorithms like MUSIC that require the noise subspace, PAST does not directly compute it. Instead, it can be estimated via the projection matrix onto the null subspace, $\text{span}(\overline{\mathbf{U}_s}) = \text{span}(\mathbf{U}) \setminus \text{span}(\mathbf{U}_s)$(YANG, 1995), is the complement of the orthogonal projection onto the signal subspace and can be calculated as (LIN *et al.*, 2015)

$$\overline{\mathbf{U}_s} = \mathbf{I}_N - \mathbf{U}_s\mathbf{U}_s^H, \tag{4.15}$$

assuming $\mathbf{U}_s$ has orthonormal columns.

4.3 DOA ESTIMATION

DoA information is fundamental to a wide range of applications, from radar and sonar to wireless communications. It is determined by measuring the characteristics of a received wavefront across a sensor array—in this case, an antenna array. For a satellite ground station, accurate DOA estimation is critical for several key tasks: tracking the satellite as it moves across the sky, spatially filtering the signal to optimize reception, and pre-coding the transmission signal for efficient beamforming.

There are many methods to estimate DoA, with two of the most prominent being MUSIC and ESPRIT. These are subspace-based algorithms capable of estimating the DOA from multiple, independent signal sources. For this work, the MUSIC algorithm was selected.

4.3.1 MUSIC

Its core principle is based on exploiting the orthogonality between the signal subspace and the noise subspace, which are derived from the received signal's covariance matrix. After the signal and noise subspaces have been identified using a technique like SVD or an adaptive tracker like PAST, the MUSIC algorithm can be applied to estimate the DoA of the satellite signal. The fundamental insight of MUSIC is that the steering vectors corresponding to the true directions of arrival lie entirely within the signal subspace and are, therefore, perfectly orthogonal to the noise subspace.

This orthogonality condition allows us to define a cost function, often called the MUSIC pseudospectrum, which will have sharp peaks at the angles corresponding to the true DoAs. The cost function is defined as the inverse of the squared projection of a candidate steering vector onto the noise subspace (KRIM; VIBERG, 1996):

$$J(\boldsymbol{\Theta}) = \frac{1}{\mathbf{a}(\boldsymbol{\Theta})^H \mathbf{U}_w \mathbf{U}_w^H \mathbf{a}(\boldsymbol{\Theta})} = \frac{1}{\|\mathbf{a}(\boldsymbol{\Theta})^H \mathbf{U}_w\|^2}, \tag{4.16}$$

where:

- $\boldsymbol{\Theta} = [\theta, \phi]$ is the vector of candidate zenith and azimuth angles.
- $\mathbf{a}(\boldsymbol{\Theta})$ is the steering vector of the array for the direction $\boldsymbol{\Theta}$, computed as described in

Section 2.2.3.1.

When the candidate direction $\boldsymbol{\Theta}$ is equal to the true DoA of a signal, the steering vector $\mathbf{a}(\boldsymbol{\Theta})$ is orthogonal to the noise subspace. This makes the denominator of the cost function approach zero, resulting in a sharp peak (theoretically infinite for signal with no distortion) in the function's output. The estimated DoAs of source i are therefore the angles that maximize this function:

$$\hat{\boldsymbol{\Theta}}_i = \arg\max_{\boldsymbol{\Theta}} J(\boldsymbol{\Theta}). \tag{4.17}$$

Practical Angular Scanning

In practice, the maximization of the cost function is achieved by performing a systematic search over all possible directions of arrival. For a UPA, this involves a two-dimensional scan across the azimuth and zenith angles. It is illustrated in Figure 4.2.

Here is a description of the algorithm:

1. From the received signal matrix $\mathbf{X}$, perform a subspace decomposition to obtain the matrix of noise eigenvectors, using either SVD ($\mathbf{U}_w$) or PAST ($\overline{\mathbf{U}_s}$).

2. Define a search range and step size for both angles $\boldsymbol{\Theta}$. e.g.: $\theta \in [0^o,90^o]$ and $\phi \in [0^o,360^o]$, each with a step of 0.5^o. The fineness of this grid determines the precision of the final estimate, but also significantly impacts the computational cost.

3. Initialize an empty results grid matrix to store the output of the cost function for each (j,l)-th angle pair.

4. Inside the loops, for the current angle pair θ_j and ϕ_l, construct the theoretical steering vector for the UPA, $\mathbf{a}(\boldsymbol{\Theta}_{jl})$.

5. Project the steering vector onto the noise subspace and calculate the value of the MUSIC pseudospectrum $J(\boldsymbol{\Theta}_{jl})$ and store this value in the results grid.

6. After the loops have completed, search in the pseudospectrum grid for the coordinates $(\theta_{\max},\phi_{\max})$ that correspond to the maximum value in the grid. These coordinates are

Figure 4.2. MUSIC sweep plot on the θ and ϕ axes. In (a), the sweep is made by SVD without FDM, suffering from aliasing. In (b), it is made by SVD (left) and PAST (right), with FDM, i.e. correcting the aliasing issue.

a)

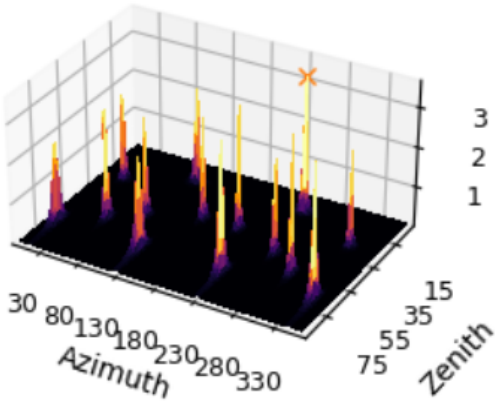

b)

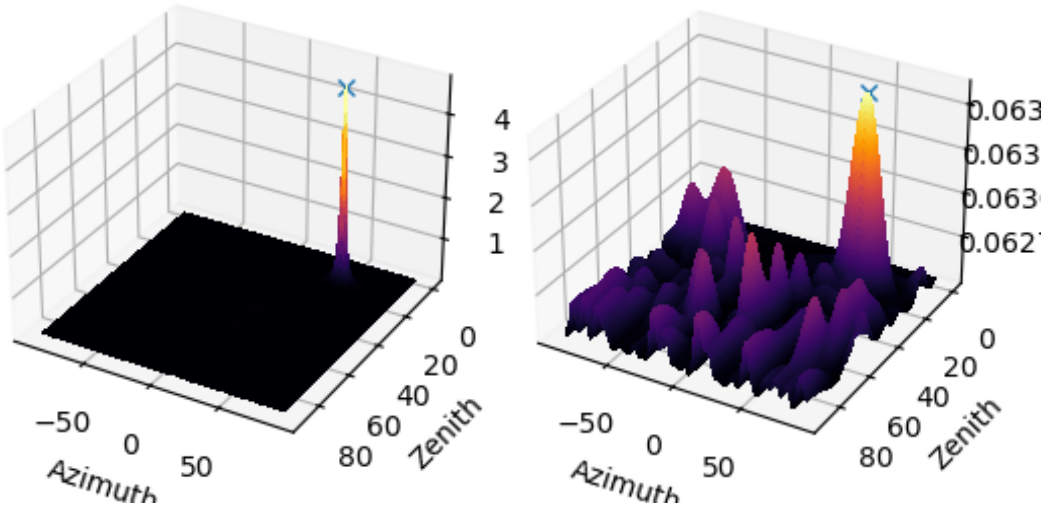

Source: Own authorship.

the estimated DoA, $\hat{\boldsymbol{\Theta}}$, of (4.17). If multiple signals are present, there will be multiple distinct peaks corresponding to each source.

4.4 SPATIAL FILTERING

Once the DoA of the desired satellite signal has been accurately estimated, the next step in the reception chain is to apply spatial filtering. This process involves, intelligently, combining the signals from all N elements of the antenna array. The primary objective is to constructively combine the signal components arriving from the satellite's direction while destructively interfering with noise and any interfering signals arriving from other directions, mitigating interference from, e.g., terrestrial sources and other satellites.

This technique significantly enhances the desired signal's strength, thereby improving the overall SINR and the final BER, thereby enhancing detection, demodulation, and tracking accuracy (TREES, 2002). For ground stations with arrays receiving satellite signals (downlink), the same filter coefficients derived for reception can be applied in reverse to beamform the return-link (uplink) signal, steering the transmitted energy toward the satellite with maximum gain and minimal interference leakage.

Let $\mathbf{X} \in \mathbb{C}^{N \times K}$, with K samples, be the received signal matrix as discussed in Section 3.1. The output of spatial filtering, $\mathbf{y}$, is a vector signal formed by a weighted sum of the signals received at each $n \in [1, \cdots, N]$ antenna element:

$$\mathbf{y} = \sum_{n=1}^{N} w_n^* \mathbf{x}_n = \mathbf{w}^H \mathbf{X}, \tag{4.18}$$

where $\mathbf{x}_n$ is the vector of the $N \times 1$ row of $\mathbf{X}$, and $\mathbf{w}$ is the vector $N \times 1$ of complex w_n applied to each element. The core of spatial filtering lies in determining the optimal set of weights $\mathbf{w}$. This section will describe two fundamental beamforming methods: the conventional Delay-and-Sum beamformer and the optimal Wiener filter.

4.4.1 Delay-and-Sum

The Delay-and-Sum beamformer, also known as a conventional beamformer, is the simplest and most intuitive spatial filtering technique. Its strategy is to simply co-phase the signals

from each antenna element for the known direction of the desired signal, and then sum them. This coherent summation causes the signal components from the target direction to add up constructively, while the spatially uncorrelated noise components add non-coherently.

To achieve this, the complex weights $\mathbf{w}_{DS}$ are chosen to be the steering vector corresponding to the satellite's estimated DOA, (θ_s, ϕ_s) to be applied in equation (4.18). The weight vector is therefore set to:

$$\mathbf{w} = \mathbf{w}_{DS} = \mathbf{a}(\mathbf{\Theta}_s), \tag{4.19}$$

where $\mathbf{a}(\mathbf{\Theta}_s)$ is the array's steering vector for the satellite's direction. This method effectively steers the main lobe of the array's radiation pattern directly towards the satellite, providing a gain proportional to the number of elements, N.

4.4.2 Wiener Filter

The Wiener filter provides the optimal linear solution for estimating a desired signal from a noisy measurement by minimizing the Mean Square Error (MSE) between the beamformer's output and the true desired signal. In the context of array processing, this translates to finding the weight vector $\mathbf{w}_{\text{opt}}$ that minimizes $E[\|\mathbf{d} - \mathbf{y}\|^2]$, where $\mathbf{d}$ is the desired signal waveform.

The solution to this minimization problem is given by the classic Wiener-Hopf equation(HAYKIN, 2014):

$$\mathbf{w}_{opt} = \mathbf{R}^{-1}\mathbf{p}, \tag{4.20}$$

where $\mathbf{R}$ is the covariance matrix of the received signal vector, from (4.10). This matrix contains statistical information about the desired signal, any interfering signals, and the noise. It can be estimated from the received data as described in the Section 4.2. $\mathbf{p} = E[\mathbf{X}\mathbf{d}^*]$ is the cross-correlation vector between the received signal vector and the desired signal $\mathbf{d}$.

Since the desired signal $\mathbf{d}$ is unknown at the receiver, we cannot calculate $\mathbf{p}$ directly. However, we know the spatial signature of the desired signal, which is its steering vector, $\mathbf{a}(\mathbf{\Theta}_s)$. By assuming the desired signal is uncorrelated with the interference and noise, the cross-correlation vector $\mathbf{p}$ becomes proportional to the steering vector of the desired signal. This leads to the Minimum Variance Distortionless Response (MVDR) beamformer, also known as the Capon beamformer, which is a practical implementation of the Wiener filtering concept. The MVDR

weight vector is given by:

$$\mathbf{w}_{\text{MVDR}} = \frac{\mathbf{R}^{-1}\mathbf{a}(\boldsymbol{\Theta}_s)}{\mathbf{a}(\boldsymbol{\Theta}_s)^H\mathbf{R}^{-1}\mathbf{a}(\boldsymbol{\Theta}_s)}, \tag{4.21}$$

This beamformer has the property that it passes the signal from the desired direction $\boldsymbol{\Theta}_s$ with unity gain (a distortionless response) while minimizing the power of the contributions from all other directions (minimizing the variance), which includes both noise and interference. It is therefore an adaptive filter that automatically places nulls in its radiation pattern in the directions of interfering signals, making it far superior to the Delay-and-Sum beamformer in complex signal environments(TREES, 2002).

Summary for Beamforming Implementation

1. DoA estimation: The arrival direction $\tilde{\boldsymbol{\Theta}}$ is determined using methods such as MUSIC.

2. Delay-and-sum filter coefficients calculation: Direct computation of $\mathbf{w}_{DS}$ from geometry parameters of the array and carriers frequency f_n.

3. Wiener Filter: Estimate $\mathbf{R}$ from received data; compute $\mathbf{p}$ using a known pilot or training sequence.

4. Signal combination: Apply the weights w_n to the SDR-acquired channel signals from each array element and sum.

4.5 PHASE AND TIME CORRECTION

After the raw signal from each antenna element has been acquired, digitized and multiplexed by the SDR, it remains corrupted by the significant time and phase distortions inherent to the satellite channel caused by the propagation environment. Before the information can be demodulated, the receiver must establish a coherent time and phase reference. This is a two-step process: first, the carrier phase error, dominated by the Doppler effect, must be corrected. Second, in the final part of the Digital Signal Processing (DSP) chain, the receiver's local clock must be precisely aligned with the timing of the incoming symbols to ensure sampling occurs at the optimal instant. This section details the techniques employed for both of these critical

synchronization tasks.

According to (KAPLAN; HEGARTY, 2017), modern Global Navigation Satellite System (GNSS) and satellite receivers often employ combined loops, using the FLL during acquisition and switching to PLL for tracking, where after a FLL (coarse) stabilization, the system could hand off control to a PLL for fine phase tracking, once the Doppler variation becomes slower. In this work, the fine synchronization is made in the time domain by the PLL algorithm MaM.

Having a vector of M symbols in an instant t_k (for K samples), in light of the analysis of Section 2.3.1, the combined signal from the spatial filtering block of the (4.18) can be modeled as

$$y(t_k) = \sum_{m=0}^{M-1} a_m p(t_k - mT_s - \Delta\tau) e^{j\varphi_d(t_k)} + w(t_k), \tag{4.22}$$

where:

- a_m are the transmitted symbols.
- $p(t_k)$ is the pulse shape described in Section 2.3.2.
- T_s is the symbol period.
- $\Delta\tau$ is an unknown timing , it is related to the propagation delay of Section 3.2.
- $\varphi_d(t_k)$ is the resultant phase due to Doppler shift.
- $w(t_k)$ is additive noise of mean zero.

4.5.1 FLL

Let $y[k]$ be the signal after passing by the spatial filtering block (Section 4.4). The signal is then sampled by two ADCs operating 90^o out of phase, producing the two streams of digital samples I_k and Q_k the in-phase and quadrature components and, being $k = 0, \cdots, K-1$ the sample index. These can be represented as a single stream of complex numbers, $y[k] = I_k + jQ_k$. At this stage, in an instant t_k, any residual frequency error, $f_d(t_k)$, between the received signal and the local oscillator will cause the complex samples to rotate in the complex plane at a rate of $2\pi f_d(t_k)$ radians per second (phase distortion).

A FLL is a digital feedback control system designed to estimate and track the frequency offset of an incoming signal. In the context of LEO satellite communications, its primary role is to combat the large and rapidly changing Doppler frequency shift, which can be in the order of several kilohertz. The FLL is particularly crucial during the initial signal acquisition phase, as it can lock onto the signal even with a large frequency error, a task for which a more precise PLL would struggle.

Initial Frequency Aiding

Before the FLL begins its tracking, the receiver performs an initial, coarse correction of the Doppler shift. This is known as frequency aiding. A significant advantage of satellite communication is that the Doppler shift is highly predictable. Using the satellite's orbital data as discussed on the Section 2.1.6, the GS can calculate the satellite's velocity vector $v_r(t_0)$ relative to its own ECEF position at a specific time stamp t_0 through the (2.5).

This allows for a reasonably accurate a priori estimate of the Doppler shift $\tilde{f}_d(t_0)$, computed with the (2.4). This initial estimate is used to adjust the receiver's local oscillator frequency, bringing it close to the actual received frequency. This aiding process significantly reduces the "search space"for the FLL, allowing it to achieve lock much faster and more reliably.

Feedback Loop Block

The principle for the residual frequency error estimation for the FLL is using a discriminator block to extract the frequency difference between the incoming signal and the locally generated replica. For this, it makes a Phase Differencing through the Arctangent Discriminator computing (KAPLAN; HEGARTY, 2017)

$$f_d(t_k) = \frac{\varphi_d(t_k) - \varphi_d(t_{k-1})}{2\pi T} \propto \frac{d}{dt}\left[\tan^{-1}\left(\frac{Q_k}{I_k}\right)\right], \tag{4.23}$$

where $\varphi_d(t_k)$ is the instantaneous phase (3.7) and $T = \frac{1}{R}$ is the sampling interval. This is the core of the FLL, where the frequency error is estimated.

For implementation, the operation of the FLL is a continuous iterative process that can be broken down into the following key steps:

A common and effective frequency discriminator for digitally modulated signals is the cross-product discriminator. This discriminator works by measuring the phase rotation that occurs between two consecutive complex samples, $y[k]$ and $y[k-1]$. The phase rotation is directly proportional to the frequency error. From $k = 1$ onwards, the error signal, e_k, is calculated using the following cross-product (TEUNISSEN; MONTENBRUCK, 2017)

$$e_k = \frac{Q_k I_{k-1} - I_k Q_{k-1}}{I_k I_{k-1} + Q_k Q_{k-1}} = \frac{\mathrm{Im}\{y[k]y^*[k-1]\}}{\mathrm{Re}\{y[k]y^*[k-1]\}}, \tag{4.24}$$

where $y^*[k-1]$ is the complex conjugate of the previous sample $(I_{k-1} - jQ_{k-1})$, and $\mathrm{Im}\{\cdot\}$ denotes the imaginary part of the complex product. This value is an estimate of the sine of the phase difference between the two samples given by the (4.23), which for small phase differences is approximately equal to the phase difference itself. The sign of e_k indicates the direction of the frequency error (i.e., whether the local oscillator is too high or too low), and its magnitude is proportional to the size of the error.

Nonetheless, the instantaneous error signal, e_k, is noisy due to thermal noise and the random nature of the data modulation. To obtain a stable control signal, the estimated shift frequency $\tilde{f}_d(t_k)$, the sequence of error estimates e_k is passed through a loop filter $h_{LP}(t_k)$, that is, performing the convolution.

$$\tilde{f}_d(t_k) = e_k \ * \ h_{LP}(t_k). \tag{4.25}$$

The loop filter is a digital low-pass filter that averages the error signal over a specific time constant. This filtering process smooths out the noise and provides a stable low-variance estimate of the frequency error. A typical first-order loop filter transfer function is

$$\sum_{k=-\infty}^{\infty} h_{LP}(t_k) z^{-k} = H_{LP}(z) = \frac{K_{LP}}{1 - e^{-\omega_c T} z^{-1}}, \tag{4.26}$$

in which $z \in \mathbb{C}$ is a frequency variable. This filter defines the bandwidth and stability of the loop. The loop gain K_{LP} and cutoff frequency ω_c must be chosen to be wide enough to track rapid Doppler changes in LEO (as already said, typically in the order of $\pm$40kHz), but not so wide as to follow noise. Its design is a critical trade-off: a narrow bandwidth reduces noise but also slows the loop's ability to track rapid changes in the frequency shift.

The filtered error signal is used as the control input to a Numerically Controlled Oscillator (NCO). It is a digital circuit that generates the precise frequency of the receiver's local oscillator for the downconversion stage. The control signal from the loop filter adjusts the NCO's output

Figure 4.3. Doppler frequency shift correction estimation on FLL.

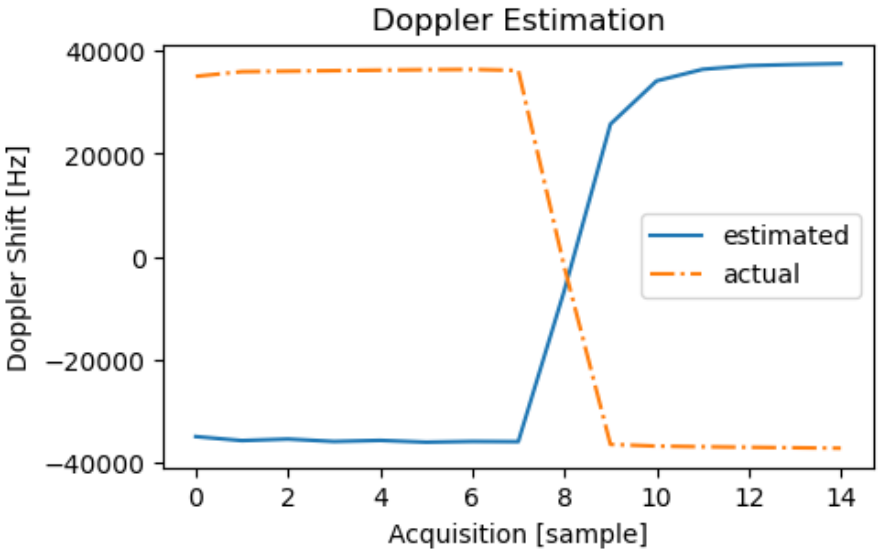

Source: Own authorship.

frequency. If the filtered error indicates the local oscillator frequency is too low, the NCO increases its frequency and vice-versa. This creates a closed feedback loop that continuously works to drive the average frequency error to zero, thereby "locking"the receiver's local oscillator to the frequency of the incoming signal (TEUNISSEN; MONTENBRUCK, 2017). For this purpose, (3.7) is digitally implemented. The filtered frequency estimate is discretely integrated to update the phase accumulator $\tilde{\varphi}_d(t_k)$ of the local oscillator:

$$\tilde{\varphi}_d(t_k) = \tilde{\varphi}_d(t_{k-1}) + 2\pi T \sum_{k=0}^{K-1} \tilde{f}_d(t_k). \tag{4.27}$$

This updates the frequency and hence the phase of the local replica to match the incoming signal, closing the loop mesh.Once the loop locks, the FLL keeps the local oscillator tuned with the Doppler-shifted frequency. Then the output signal samples are fixed by phase multiplication:

$$y'[k] = y[k]e^{-\jmath\tilde{\varphi}_d(t_k)}. \tag{4.28}$$

Figure 4.4 illustrates this whole process in the signal.

4.5.2 M&M Timing Synchronization

After the carrier phase error has been corrected by the FLL, the resulting baseband signal still needs to be synchronized in time. The receiver must determine the precise moments to

Figure 4.4. Blocks diagram of FLL system for Doppler phase shift correction.

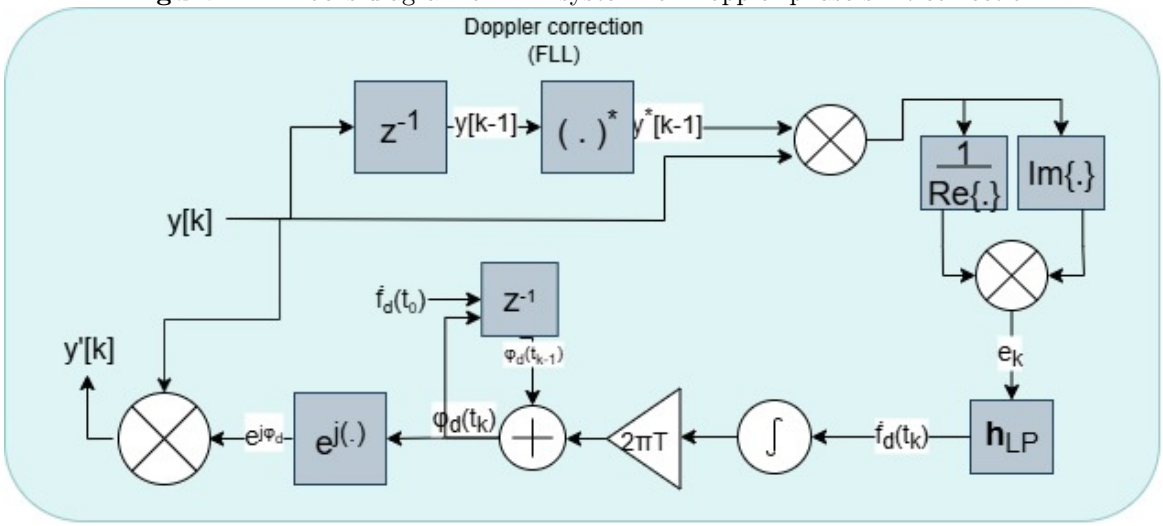

Source: Own authorship.

sample the waveform to capture each symbol at the point of maximum SNR and minimum ISI. For this task, the MaM algorithm is employed.

The MaM algorithm is a NDA timing error detector, meaning it does not require a known pilot sequence to operate. It derives a timing error signal directly from the received data samples, making it highly efficient. The algorithm operates in real time and works by comparing the received sample at the current decision instant with the preceding sample and the corresponding symbol decisions in a closed loop. It is robust to unknown symbol sequences and works well under moderate ISI and noise conditions.

Knowing the number of samples per symbol $N_s = \frac{K}{M}$, the timing error ϵ_m at the m-th symbol instant is calculated as

$$\epsilon_m = \mathrm{Re}\{\hat{y}^*_{m-1} y_m - \hat{y}^*_m y_{m-1}\}, \tag{4.29}$$

where

- y_m and y_{m-1} are the complex samples received at the current and previous decision instants mN_s and $(m-1)N_s$.
- $\hat{y}_m$ and $\hat{y}_{m-1}$ are the corresponding hard decisions (i.e., the nearest constellation points) for those symbols.

This error signal has the property of being, on average, zero when the sampling is perfectly

timed ($\Delta\tau = 0$). If the sampling is too early ($\Delta\tau > 0$), the error signal will be positive, and if it is too late ($\Delta\tau < 0$), it will be negative.

This error signal is then fed into a loop filter h_{LP}, which controls the timing of the sampling clock (provided by a Voltage-Controlled Oscillator (VCO)). This feedback mechanism, known as a Timing Recovery Loop, continuously adjusts the sampling instants to drive the average error to zero, thereby locking the receiver's clock to the timing of the incoming symbols. This ensures that each symbol is sampled at its optimal point, maximizing the performance of the demodulator. The offset symbol decision instant $\tau[m]$ is computed as

$$\tau[m] = \tau[m-1] + C\ \epsilon_m * h_{LP}. \tag{4.30}$$

C is loop gain constant. h_{LP} is similar to that of Section 4.5.1 and its cutoff frequency must be adjusted with respect to T_s.

Finally, with $\tau[0]$ being able to be initiated as zero, the output synchronized signal is

$$y_m = y'(mN_s + \text{round}(\tau[m])), \tag{4.31}$$

where round(τ) is the integer number nearest to τ. Figure 4.5 illustrates this whole process in the signal.

Figure 4.5. Blocks diagram of MaM system for clock time synchronization.

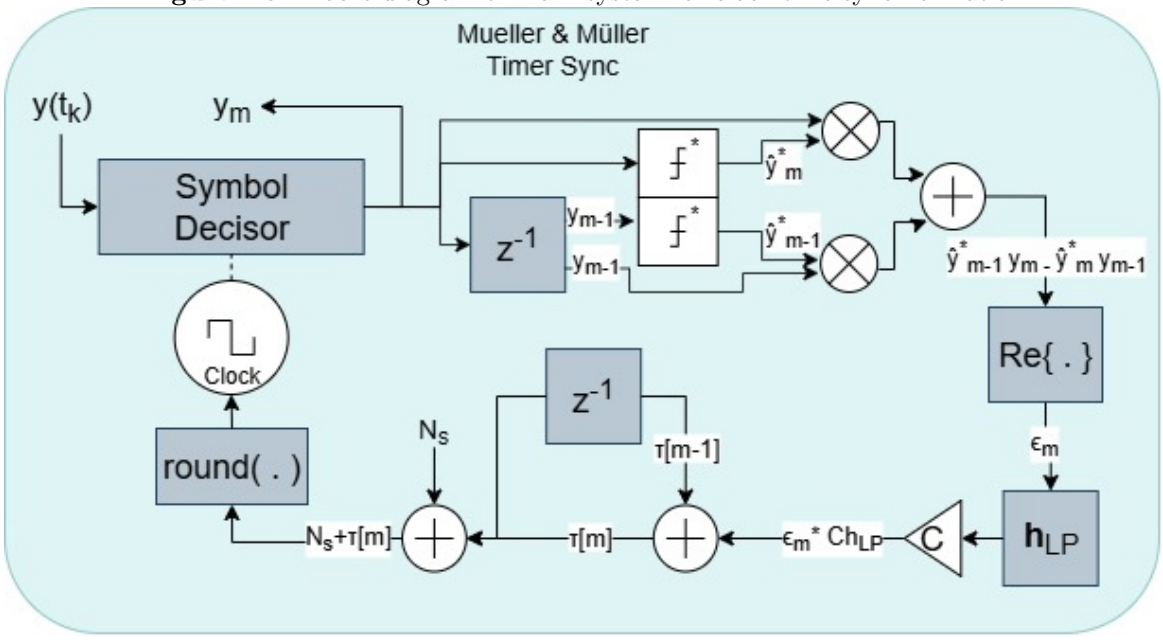

Source: Own authorship.

CHAPTER 5

RESULTS AND CONCLUSIONS

The validation of the signal processing algorithms and the overall system model developed in this work is conducted through a series of simulations. It is important to emphasize that the system was not been tested in a real-world hardware environment. The results presented herein are based on a controlled, simulated LEO satellite communication link designed to evaluate the performance of the core algorithms under specific conditions. The steps for the development and evaluation of this work are shown in the Figure 5.1.

For the signal acquisition process, the simulations rely on the concept of using previously obtained satellite timestamps. In a practical application, this would correspond to the SDR using ephemeris data (e.g., TLEs) to predict the satellite's position and Doppler shift at a given time, thereby acquiring and time-stamping the received signal blocks for subsequent processing.

To maintain focus on the primary research objectives, several simplifications are made in the simulation environment. The satellite trajectory is modeled as a perfect circular orbit. The channel model is simplified to include only the FSPL and AWGN. Deleterious effects such as multipath propagation and other forms of fading are not modeled. Furthermore, the simulations deal exclusively with the reception of known pilot signal messages to assess the performance of the synchronization and estimation algorithms without the added complexity of data decoding.

5.1 SETUP PARAMETERS

The following subsections detail the parameters used to configure the simulation scenario, the ground station array, and the transmission and reception signal chains.

Figure 5.1. Sequence of steps for the development/evaluation of this work.

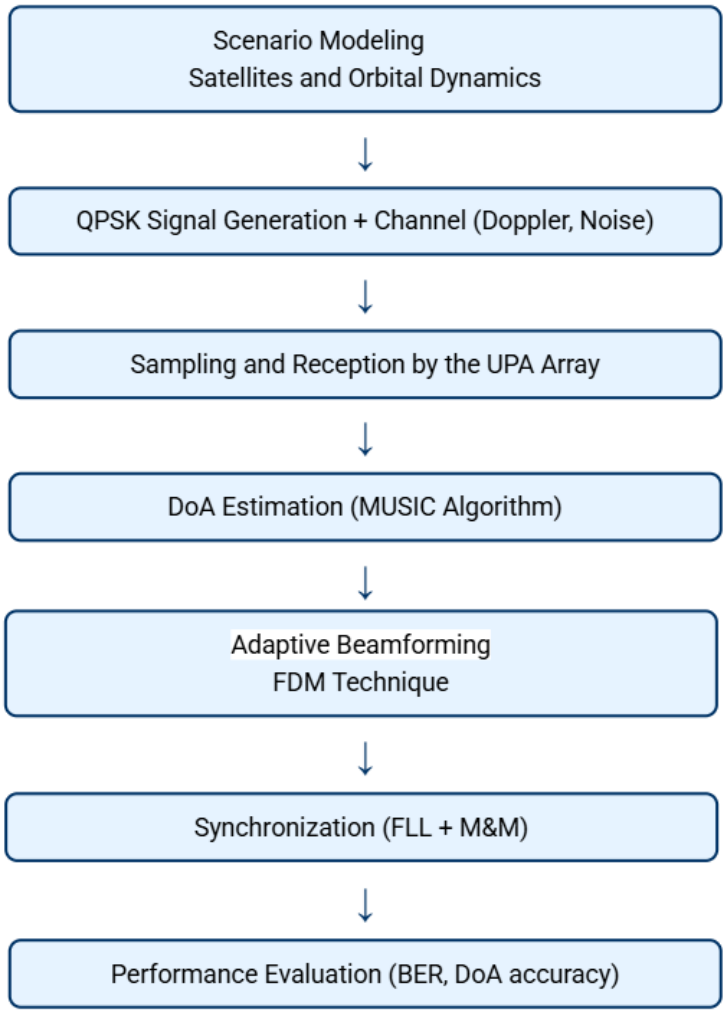

Source: Own authorship.

5.1.1 Scenario

A circular LEO satellite orbit was simulated with a fixed altitude h. The total duration of the satellite pass available for communication was set to $T_p = 1.2$ minute. During this pass, signal acquisitions (snapshots) were taken at regular intervals of $\Delta T = 20$ seconds, resulting in a total of N_T snapshots for analysis.

Table 5.1. Orbital parameters.

Quantity	**Notation**	**Value**	**Unit**
Snapshot period	ΔT	6	sec
Number of snapshots	N_T	12	-
Total satellite pass time	T_p	1.2	min
Earth radius	R_E	6371	km
Satellite altitude	h	150	km

Source: Own authorship.

5.1.2 UPA

The ground station was modeled with a $N_y \times N_z$ Uniform Planar Array with an interelement spacing of $d_y = d_z = 2\lambda$. To mitigate grating lobes, a subcarrier frequency spacing was applied to each element according to the FDM scheme in (4.7), where the frequency offset for the element at position (y, z) is given by $\Delta f_{yz} = \left(y - \frac{N_y-1}{2}\right)\Delta f + \left(z - \frac{N_z-1}{2}\right)\Delta f$, for $y = 0, \cdots, N_y - 1$ and $z = 0, \cdots, N_z - 1$, this arrangement is shown in the Figure 5.2. The array (all the parabolic antennas) boresight was mechanically fixed, pointing towards the satellite's DOA at the time of the first snapshot, $\boldsymbol{\Theta}(t_1)$.

Table 5.2. Array and antenna parameters.

Quantity	**Notation**	**Value**	**Unit**
Number of array elements	$N_y = N_z$	4	-
Array spacing	$d_y = d_z$	4λ	m
Subcarrier frequency spacing	Δf	$625 \cdot 10^6 \cdot \frac{d_y}{\mathrm{m}}$	Hz
Parabola diameter	d	2	m
Antenna efficiency	η_a	0.8	-

Source: Own authorship.

Figure 5.2. Allocation of subcarrier frequencies to each array element along the y and z axes.

	0	1	2	3
0	1.250	1.583	1.917	2.250
1	1.583	1.917	2.250	2.583
2	1.917	2.250	2.583	2.917
3	2.250	2.583	2.917	3.250

Source: Own authorship.

5.1.3 Transmission signal

The transmitted signal was a QPSK modulated pilot sequence. The baseband symbols were shaped using the raised-cosine pulse $p(t)$ as described in Section Section 2.3.2.

Table 5.3. Transmission signal parameters.

Quantity	Notation	Value	Unit
Carrier central frequency	f_0	2.25	GHz
Number of symbols in pilot sequence	M	64	-
Symbol duration time	T_s	50	ns
Roll-off factor	b	0.35	-

Source: Own authorship.

5.1.4 Reception

At the receiver, low-pass filters were used in both the FLL and MaM feedback loops. An additional low-pass filter, h_{LP}, was implemented after the phase correction stage and before timing synchronization to filter residual noise and improve the accuracy of the symbol decisions used by the MaM algorithm.

Table 5.4. Reception parameters.

Quantity	Notation	Value	Unit
Sampling period	T	$\frac{T_s}{8} = 6.25$	nsec
Cutoff frequency of low-pass filter	f_c	$\frac{1}{T_s} = 20$	MHz

Source: Own authorship.

Table 5.5. MUSIC/PAST parameter.

Quantity	Notation	Value	Unit
Angle step for MUSIC scanning	-	0.5	deg
PAST forgetting factor	ξ	0.99	-

Source: Own authorship.

Table 5.6. Phase tracking and symbol timing parameters.

Quantity	Notation	Value	Unit
FLL loop filter gain	K_{loop}	0.2	-
FLL loop filter cutoff frequency	f_{FLL}	$\frac{1}{T_s} = 20$	MHz
M&M loop filter cutoff frequency	f_{MaM}	$\frac{1}{T_s} = 20$	MHz
M&M loop gain	C	0.4	-

Source: Own authorship.

5.2 SIMULATIONS AND PERFORMANCE ANALYSIS

The models and algorithms described in this thesis were implemented using the Python programming language[1].

The performance of the system was evaluated using Monte Carlo simulations. For each test, random pilot sequences (for each Montecarlo) of length $M = 64$ were transmitted. A random reception delay of $\Delta\tau \sim \mathcal{U}(0,0.25T_s]$ was introduced to test the timing recovery, and AWGN with zero mean and variable power was added to the signal.

The GS was placed at a fixed location on the Earth surface, while the LEO satellite orbit was generated such that the GS was approximately at the center of the satellite footprint at the midpoint of the simulated pass (at snapshot $\frac{N_T}{2}$). The satellite path is fixed.

Table 5.7. GS and satellite orbit parameters.

Quantity	Notation	Value	Unit
GS latitude and longitude	$(\vartheta_{GS},\phi_{GS})$	$(-16,-48)$	deg
Satellite central latitude and longitude	$(\vartheta_{Sat},\phi_{Sat})$	$(\vartheta_{GS},\phi_{GS})$	deg
Satellite angular velocity components	$(\omega_\vartheta,\omega_\phi)$	$(15.5, 4.1)$	Revolutions/day
Montecarlo realizations	-	1000	-

Source: Own authorship.

[1]The complete source code is available at the repository found at <https://github.com/gabrielbopi/LEO_groundstation>

5.2.1 Performance tests

DoA estimation with MUSIC

The accuracy of the MUSIC algorithm for DOA estimation was assessed. Figure 5.3 plots the angular estimation error $|\boldsymbol{\Theta} - \tilde{\boldsymbol{\Theta}}|$ against the noise power and DOA estimation error at each snapshot of the satellite's pass.

Figure 5.3. DOA estimation. At left, deviation (average for all snapshots) vs. noise power. At right, deviation (for a specific noise power) vs. time (Snapshot).

a) SVD

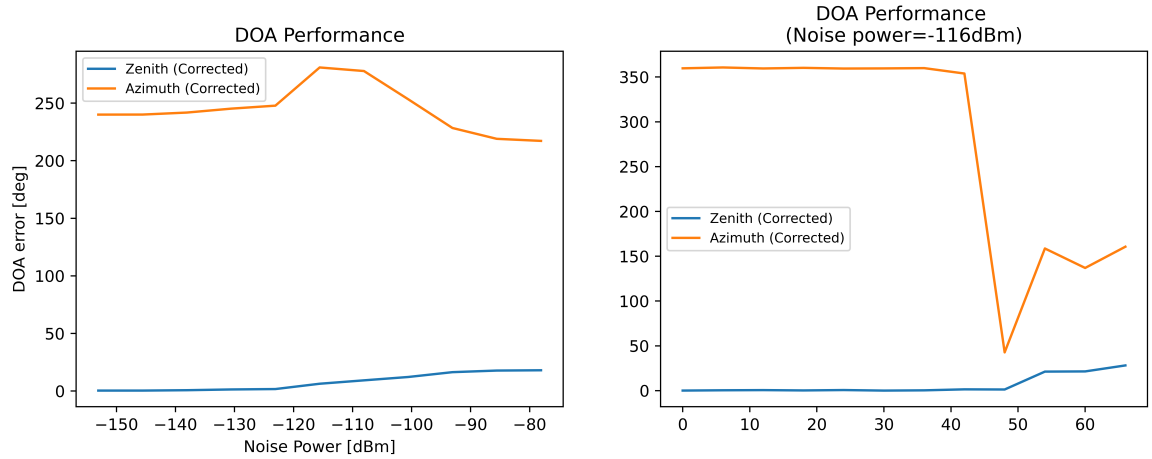

b) PAST

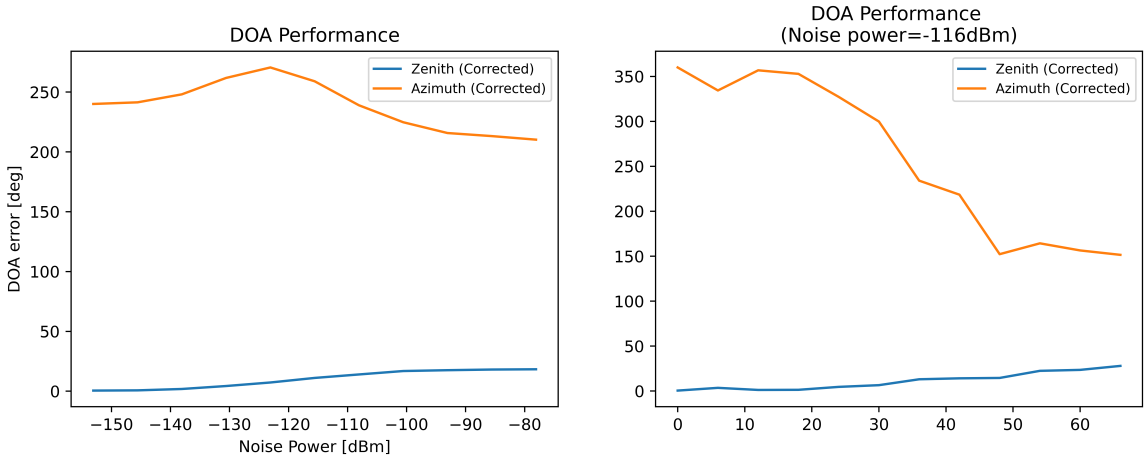

Source: Own authorship.

Looking at the graph on the right, it can be seen that the estimate fails after a certain point in time. This is likely due to the low visibility of satellite EM wave when the DoA is not close to the parabola boresight, given the short-range directivity of these antennas. This demonstrates the need for antenna systems with greater range to maximize the visibility of the

emitted signal.

In the graph on the left, it can be seen that the amount of error in the estimation increases progressively with increasing noise power level, demonstrating that signal quality is important for accurate estimation of DoA.

Doppler correction

The performance of the FLL in tracking the time-varying Doppler shift was evaluated. Figure 5.4 shows the deviation $|f_d - \tilde{f}_d|$ of the frequency estimate from the true Doppler shift as a function of the noise power and the estimation deviation at each snapshot throughout the satellite pass.

Figure 5.4. Doppler estimation. At left, deviation (average for all snapshots) vs. noise power. At right, deviation (for a specific noise power) vs. time (Snapshot).

a) SVD

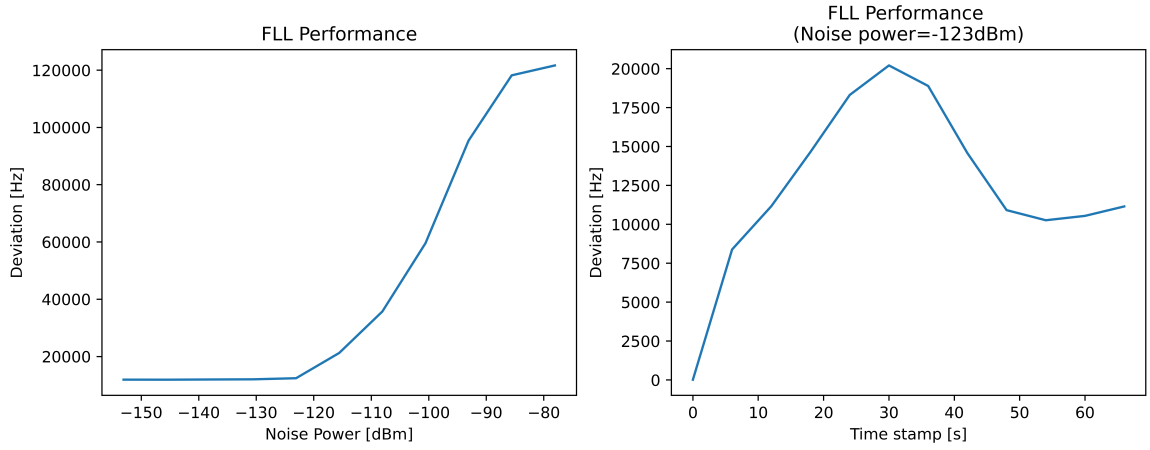

b) PAST

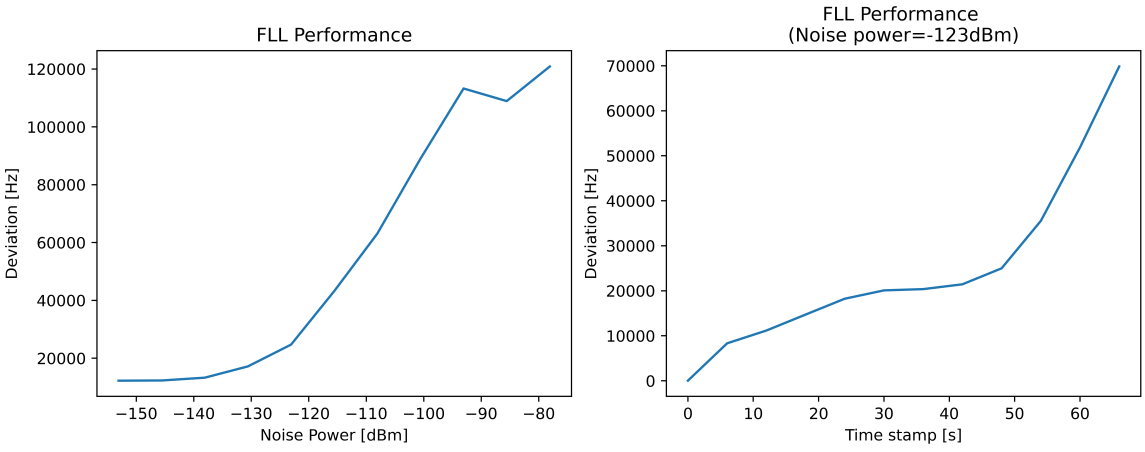

Source: Own authorship.

Analyzing the graph on the left, it can be seen that the system performs well up to a certain noise level (approximately −123 dBm). After this point, excessive distortion in the signal amplitude leads to signal discrimination failures (the (4.24) stage).

Looking at the right, we see that there is a peak error at one point due to a failure in the DOA estimation, but it is subsequently corrected due to the adaptive nature of the FLL. This shows that the accuracy of the FLL depends on the performance of the DoA estimation.

Reception BER × SNR

The end-to-end performance of the receiver was evaluated by measuring the BER as a function of the SNR. Figure 5.5 shows the performance under certain conditions: with no additional distortions (ideal case), with no corrections applied, with only the FLL active, with only timing synchronization active, and with both synchronization loops active.

Figure 5.6 shows this performance evaluation when the FDM technique is not used, where it can be seen that in all cases the estimation fails, becoming unfeasible. This demonstrates the importance of implementing FDM in the system.

It can be seen that phase and timing corrections result in an overall performance gain in the system (purple curve compared to orange), demonstrating some effectiveness of the techniques, although somewhat limited for the tested configurations. This limitation can also possibly be attributed to the satellite's low visibility range.

However, it can also be noted that symbol synchronization without phase correction worsened reception performance (red curve compared to orange), demonstrating the need to jointly implement both correction blocks in the system (phase correction and symbol synchronization, as seen in the purple curve compared to green).

5.3 CONCLUSIONS

This dissertation has presented a comprehensive investigation into the implementation of adaptive signal processing algorithms for a LEO satellite ground station based on a large-space UPA. The primary motivation for this work was to address the growing need for agile, low-cost

Figure 5.5. BER vs. SNR for different receiver configurations.

a) SVD

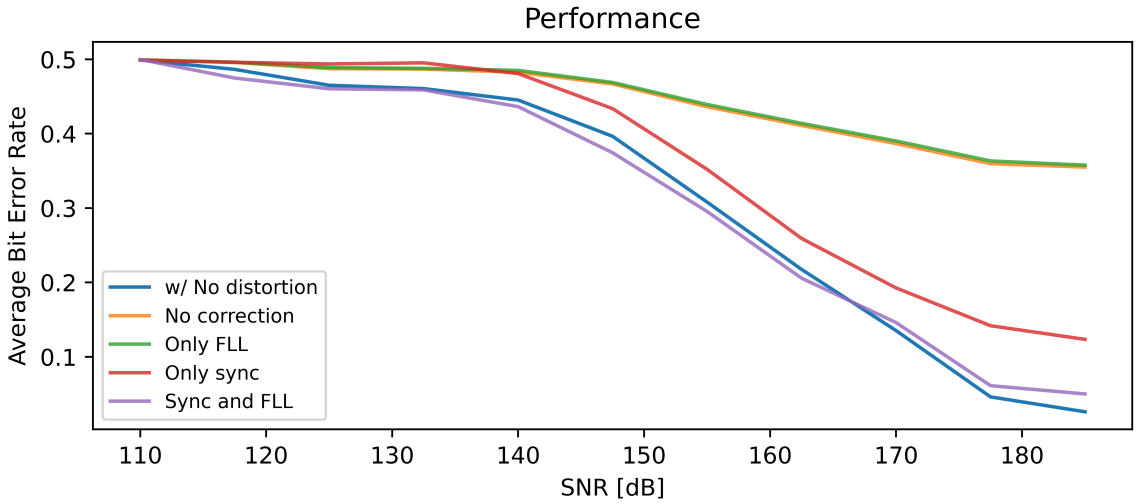

b) PAST

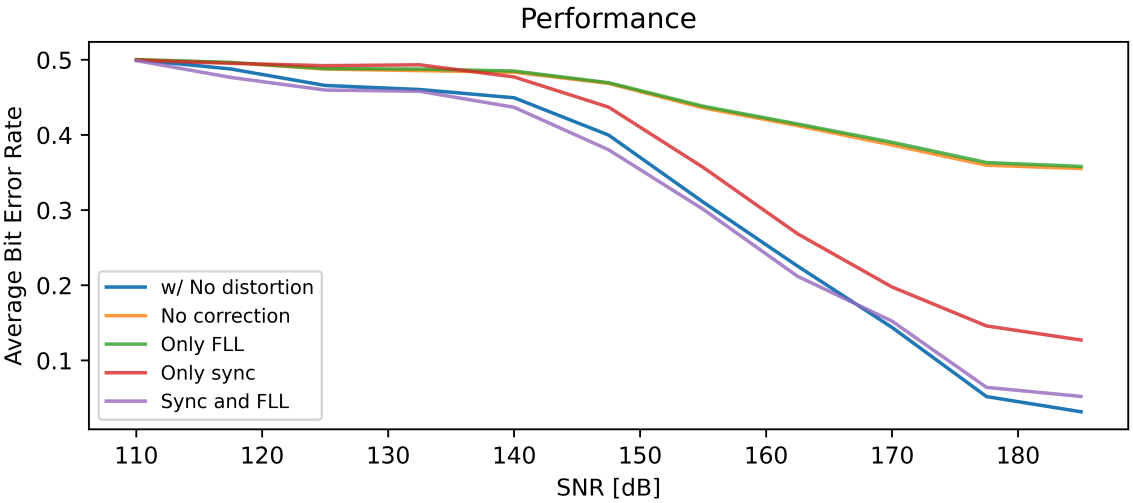

Source: Own authorship.

Figure 5.6. BER vs. SNR for different receiver configurations not making use of FDM. The estimation fails.

a) SVD

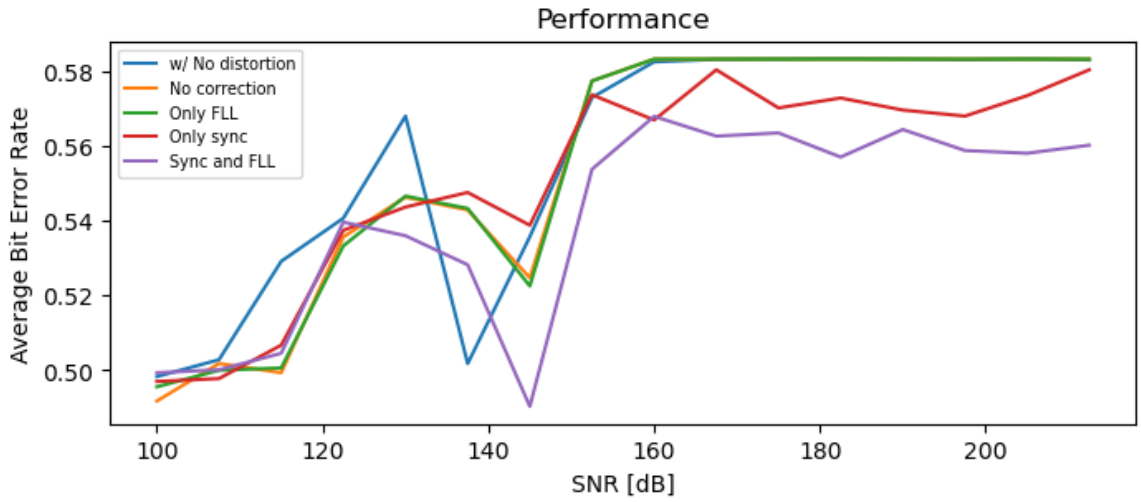

b) PAST

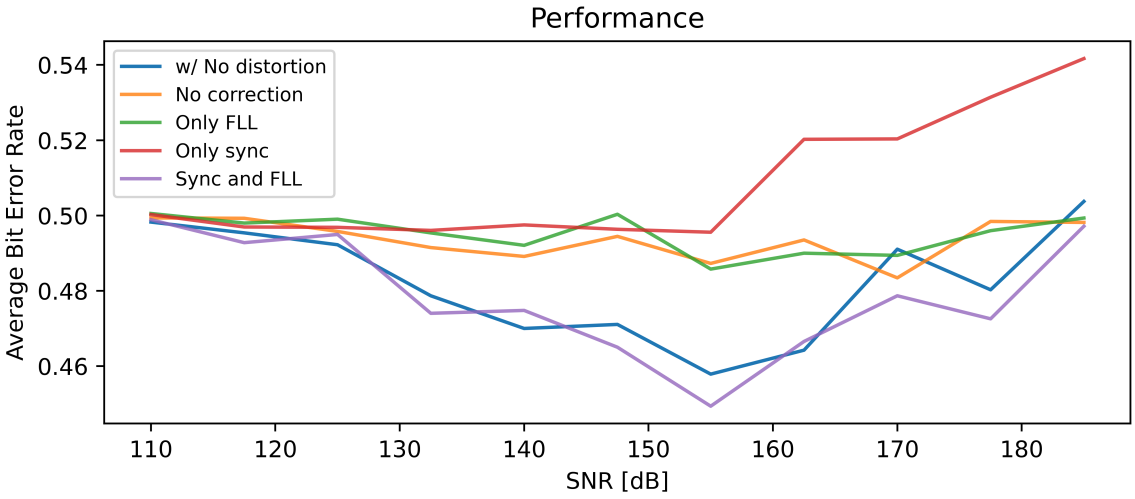

Source: Own authorship.

ground segment solutions capable of tracking fast-moving LEO satellites while tackling the inherent challenges posed by sparse array geometries, namely the presence of grating lobes.

A complete end-to-end simulation framework was successfully developed, encompassing a detailed signal model with QPSK modulation and raised-cosine pulse shaping, a dynamic LEO channel model accounting for time-varying Doppler and propagation delay, and the geometric model of the UPA. Within this framework, a full receiver chain was implemented, including robust algorithms for carrier and timing synchronization (a FLL and the MaM algorithm, respectively) and a high-resolution DoA estimation method (MUSIC).

The central contribution of this dissertation is the proposal, implementation, and analysis of a novel FDM technique for the suppression of grating lobes. By assigning a unique subcarrier frequency to each antenna element, the system successfully emulates the behavior of a non-uniform array in the signal processing domain. The simulation results have shown that this technique mitigates grating lobes, but at the cost of increasing the total signal bandwidth. Empirical analysis suggests that for shorter inter-element distances (e.g., $d_{y,z} \leq 4\lambda$), the linear relationship between the required subcarrier spacing and the array spacing makes the technique viable within reasonable system bandwidth limits.

The performance analyses have revealed any insights. With the array's initial pointing fixed at the first DoA, the system's performance was strong at the beginning of the satellite pass but deteriorated as the satellite moved away. This degradation is likely due to the worsening of the DoA estimate, a consequence of the poor visibility of the individual parabolic antennas to a satellite far from their boresight, given their characteristic high directivity. This highlights a critical relationship: the accuracy of the FLL is directly dependent on the performance of the DoA estimate. While the phase and timing correction loops demonstrated some effectiveness, the overall performance gains were modest for the tested configurations. This limitation can also be attributed to the satellite's low visibility range as it moved away from the array's fixed pointing direction. However, it must be made known that this work was conducted under a set of simplifying assumptions, including a channel model limited to Free-Space Path Loss and AWGN, and the absence of real-world hardware testing.

5.3.1 Future Works

The research presented in this dissertation provides a simulation-based validation of digital communication methods, establishes a foundational framework for adaptive array processing in LEO satellite ground stations and introduces a novel technique for grating lobe mitigation. Nevertheless, the simplifications made in the models and the scope of the investigation open up numerous avenues for future research. The following areas are identified as promising directions for extending and enhancing this work:

- **Extension of the channel model:** The channel considered in this work was simplified, relying solely on FSPL and AWGN. Future models should include the effects of multipath propagation, small-scale fading (Rician and Rayleigh), and atmospheric attenuation phenomena (such as gaseous absorption). These additions would bring the simulations closer to the conditions of real satellite links and allow a more rigorous evaluation of receiver performance.

- **Antenna directivity limitations:** The short-range directivity of parabolic antennas observed in this study highlights the need for antenna systems with wider coverage to maximize visibility of the satellite signal. A promising approach is to test different pointing strategies for each parabola in the array, thereby increasing the effective visibility within the satellite footprint and mitigating performance degradation as the satellite moves away from the initial boresight.

- **FDM-based grating lobe mitigation:** Further investigation is needed into the FDM approach to suppress grating lobes in large-spaced arrays. In particular, exploring alternative schemes for the subcarrier frequency spacing Δf_n and optimizing the allocation of subcarriers under the constraints of practical bandwidth limits in the uplink remains an important direction.

- **Decoupling and calibration:** The ideal array model used in this work neglects the real-world impairments of mutual coupling between antenna elements and gain/phase errors in the RF front-end. Future research should incorporate decoupling and calibration techniques to compensate for these non-idealities, which is essential for achieving the high

performance predicted by theory.

- **Real LEO constellation simulations:** Future simulations should incorporate real satellite constellations (e.g., OneWeb, Starlink, or open-access CubeSat constellations), including the effects of inter-satellite handoffs as a satellite exits the visibility range of the ground station and another takes its place. This would allow the evaluation of tracking algorithms in realistic multi-satellite scenarios.

- **Adaptive Interference Cancellation:** This work focused on signal enhancement in a noise-limited environment. Future efforts should implement fully adaptive beamforming techniques, such as the LMS or Kalman filter algorithms. This would leverage the array's capabilities for interference cancellation from other sources, enabling dynamic tracking of the desired satellite while simultaneously placing nulls in the directions of interfering signals.

- **Hardware implementation:** Experimental validation of the proposed techniques is essential. An important next step is to implement the algorithms on real SDR platforms and evaluate their performance under real-world conditions, including orbital dynamics, Doppler shifts, and hardware-induced distortions.

- **Efficient DoA estimation:** Finally, further investigation into more efficient and adaptive DoA estimation methods with reduced computational burden is necessary. While effective, the MUSIC algorithm's angular scan is computationally intensive. Techniques such as ESPRIT, or hybrid model-driven/data-driven approaches may provide a favorable trade-off between accuracy and complexity.

REFERENCES

AGATONOVIĆ, M.; STANKOVIC, Z.; DONCOV, N.; SIT, L.; MILOVANOVIĆ, B.; ZWICK, T. Application of artificial neural networks for efficient high-resolution 2D DOA estimation. *Radioengineering*, v. 21, p. 1178–1186, 12 2012. Cited in page 28.

AL-HOURANI, A. A tractable approach for predicting pass duration in dense satellite networks. *IEEE Communications Letters*, v. 25, n. 8, p. 2698–2702, 2021. Cited in page 21.

ALI, I.; BONANNI, P. G.; AL-DHAHIR, N.; HERSHEY, J. E. *Doppler Applications in LEO Satellite Communication Systems*. 1st. ed. [S.l.]: Springer Publishing Company, Incorporated, 2013. ISBN 1475783906. Cited in page 11.

ANDERSON, T. W. Asymptotic theory for principal component analysis. *The Annals of Mathematical Statistics*, Institute of Mathematical Statistics, v. 34, n. 1, p. 122 – 148, 1963. Disponível em: <https://doi.org/10.1214/aoms/1177704248>. Cited in page 53.

BADEAU, R.; RICHARD, G.; DAVID, B. Adaptive ESPRIT algorithm based on the PAST subspace tracker. In: *2003 IEEE International Conference on Acoustics, Speech, and Signal Processing, 2003. Proceedings. (ICASSP '03)*. [S.l.: s.n.], 2003. v. 6, p. VI–229. Cited 3 times in pages 9, 54, and 55.

BALANIS, C. A. *Antenna theory: analysis and design*. [S.l.]: John wiley & sons, 2016. Cited 3 times in pages 6, 30, and 33.

BRAUN, T. M.; BRAUN, W. R. *Satellite Communications Payload and System*. 2nd. ed. [S.l.]: John Wiley & Sons, Ltd, 2021. ISBN 9781119384342. Cited in page 2.

CELESTRAK. Website, *NORAD Two-Line Element Set Format*. 2022. *Online*, last accessed on 15/07/2025. Disponível em: <https://celestrak.org/NORAD/documentation/tle-fmt.php>. Cited 2 times in pages 19 and 20.

CHENG, Y.; HAARDT, M.; HENNIGER, H.; METZIG, R.; DIEDRICH, E. Interference suppression and electronic tracking using antenna arrays at satellite ground stations. In: *WSA 2013; 17th International ITG Workshop on Smart Antennas*. [S.l.: s.n.], 2013. p. 1–7. Cited in page 5.

DAVIS, L.; COLLINGS, I.; EVANS, R. Estimation of LEO satellite channels. In: *Proceedings of ICICS, 1997 International Conference on Information, Communications and Signal Processing. Theme: Trends in Information Systems Engineering and Wireless Multimedia Communications (Cat.* [S.l.: s.n.], 1997. v. 1, p. 15–19 vol.1. Cited in page 6.

ETSI. *Study on channel model for frequencies from 0.5 to 100 GHz (3GPP TR 38.901 version 16.1.0 Release 16)*. [S.l.], 2020. Cited 2 times in pages 25 and 26.

GARDNER, F. A BPSK/QPSK timing-error detector for sampled receivers. *IEEE Transactions on Communications*, v. 34, n. 5, p. 423–429, 1986. Cited in page 10.

HAARDT, M.; ZOLTOWSKI, M.; MATHEWS, C.; RAMOS, J. Esprit and closed-form 2-d angle estimation with planar arrays. *Digital Signal Processing Handbook*, Boca Raton, FL: CRC, 1998. Cited in page 9.

HAYKIN, S. *Adaptive filter theory*. 5th. ed. Upper Saddle River, NJ: Prentice Hall, 2014. Cited 2 times in pages 53 and 60.

HE, G.; GAO, X.; SUN, L.; ZHANG, R. A review of multibeam phased array antennas as LEO satellite constellation ground station. *IEEE Access*, v. 9, p. 147142–147154, 2021. Cited in page 1.

INGRAM, M. A.; BAROTT, W. C.; POPOVIC, Z.; RONDINEAU, S.; LANGLEY, J.; ROMANOFSKY, R.; LEE, R. Q.; MIRANDA, F.; STEFFES, P.; MANDL, D. LEO download capacity analysis for a network of adaptive array ground stations. In: *SERP 2005*. [s.n.], 2005. Disponível em: <https://ntrs.nasa.gov/citations/20050210122>. Cited in page 1.

INGRAM, M. A.; ROMANOFSKY, R.; LEE, R. Q.; MIRANDA, F.; POPOVIC, Z.; LANGLEY, J.; BAROTT, W. C.; AHMED, M. U.; MANDL, D. Optimizing satellite communications with adaptive and phased array antennas. In: *ESTC 2004*. [S.l.: s.n.], 2004. Cited 3 times in pages 2, 3, and 21.

JIANG, S.; FU, N.; WEI, Z.; LIAN, Z.; QIAO, L.; PENG, X. Compressed sampling for spectrum measurement and DOA estimation with array cooperative MWC. *IEEE Transactions on Instrumentation and Measurement*, v. 72, p. 1–14, 2023. Cited in page 10.

JR, L. J. I. *Satellite communications systems engineering: atmospheric effects, satellite link design and system performance*. 2nd. ed. [S.l.]: John Wiley & Sons, 2017. Cited in page 18.

KAPLAN, E.; HEGARTY, C. J. *Understanding GPS/GNSS: Principles and Applications, Third Edition*. 3rd. ed. USA: Artech House, Inc., 2017. ISBN 1630810584. Cited 3 times in pages 10, 62, and 63.

KHALILPOUR, J.; RANJBAR, J.; KARAMI, P. A novel algorithm in a linear phased array system for side lobe and grating lobe level reduction with large element spacing. *Analog Integrated Circuits and Signal Processing*, v. 104, n. 3, p. 265–275, 2020. Disponível em: <https://doi.org/10.1007/s10470-020-01612-1>. Cited in page 11.

KRIM, H.; VIBERG, M. Two decades of array signal processing research: The parametric approach. *Signal Processing Magazine, IEEE*, v. 13, p. 67 – 94, 08 1996. Cited 2 times in pages 9 and 56.

KRIVOSHEEV, Y. V.; SHISHLOV, A. V.; DENISENKO, V. V. Grating lobe suppression in aperiodic phased array antennas composed of periodic subarrays with large element spacing. *IEEE Antennas and Propagation Magazine*, v. 57, n. 1, p. 76–85, 2015. Cited in page 11.

KUMAR, G.; RAO, G.; KUMAR, M. GPS signal short-term propagation characteristics modeling in urban areas for precise navigation applications. *Positioning*, v. 04, p. 192–199, 01 2013. Cited in page 92.

LCEPT. Website, *CNPq: Estação Terrena Autônoma Distribuída de Baixo Custo e Alta Taxa de Download*. 2022. *Online*, last accessed on 04/07/2025. Disponível em: <https://lab-telecom.unb.br/2022/03/05/cnpq-edital-uniespaco-2022-estacao-terrena-autonoma-distribuida-de-baixo-custo-e-alta-taxa-de-down>. Cited 2 times in pages 2 and 3.

LIN, H.-C.; HOWARD, M.; VIJAYAKUMAR, S. Learning null space projections. In: *2015 IEEE International Conference on Robotics and Automation (ICRA)*. [S.l.: s.n.], 2015. p. 2613–2619. Cited in page 55.

LIN, Z.; CHEN, Y.; LIU, X.; JIANG, R.; SHEN, B. Adaptive beamforming design of planar arrays based on bayesian compressive sensing. *IEEE Sensors Journal*, v. 21, n. 4, p. 5185–5194, 2021. Cited in page 10.

LIU, L.; ZHANG, Z.; ZHANG, X.; WEI, P.; AN, J.; LI, H. Joint spectrum sensing and DOA estimation based on a resource-efficient sub-nyquist array receiver. *IEEE Transactions on Signal Processing*, v. 72, p. 5354–5370, 2024. Cited in page 10.

LIU, S.; ZHAO, J.; WU, D.; ZENG, C.; MAO, Z.; HUANG, Y. 2D DOA estimation by a large-space T-shaped array. *Digital Signal Processing*, v. 130, p. 103699, 2022. ISSN 1051-2004. Disponível em: <https://www.sciencedirect.com/science/article/pii/S1051200422003165>. Cited in page 11.

LIU, W. Super resolution DOA estimation based on deep neural network. *Scientific Reports*, v. 10, n. 1, p. 19859, 2020. Disponível em: <https://doi.org/10.1038/s41598-020-76608-y>. Cited in page 10.

MARAL, G.; BOUSQUET, M.; SUN, Z. *Satellite communications systems: systems, techniques and technology*. 6th. ed. [S.l.]: John Wiley & Sons, 2020. Cited 2 times in pages 7 and 21.

MENGALI, U. *Synchronization techniques for digital receivers*. [S.l.]: Springer Science & Business Media, 2013. Cited in page 10.

MIRZA, H. A.; RAJA, M. A. Z.; CHAUDHARY, N. I.; QURESHI, I. M.; MALIK, A. N. A robust multi sample compressive sensing technique for DOA estimation using sparse antenna array. *IEEE Access*, v. 8, p. 140848–140861, 2020. Cited in page 10.

MITOLA, J. *Software Radio Architecture: Object-Oriented Approaches to Wireless Systems Engineering*. John Wiley & Sons, 2000. 1-34 p. ISBN 9780471216643. Disponível em: <https://onlinelibrary.wiley.com/doi/abs/10.1002/047121664X.ch1>. Cited in page 50.

MORADKHANI, S.; HOSSEINZADEH, S.; ZAKER, R. Deep-learning based DOA estimation in the presence of multiplicative noise. *Wireless Personal Communications*, v. 126, n. 4, p. 3093–3101, 2022. Disponível em: <https://doi.org/10.1007/s11277-022-09854-0>. Cited in page 10.

MORI, T. Comparative study of antenna array calibration methods based on symmetrical mutual coupling of 4-element linear array. In: *IEICE Technical Report; IEICE Tech. Rep.* [S.l.]: IEICE, 2023. v. 122, n. 339, p. 6–11. Cited in page 5.

MUELLER, K.; MULLER, M. Timing recovery in digital synchronous data receivers. *IEEE Transactions on Communications*, v. 24, n. 5, p. 516–531, 1976. Cited in page 10.

ORFANIDIS, S. J. *Electromagnetic waves and antennas*. [S.l.]: Rutgers University New Brunswick, NJ, 2016. Cited 2 times in pages 22 and 25.

PINHEIRO, G. B.; ARAÚJO, D. C.; RONDINEAU, S. R. M. J. Implementation of adaptive algorithms for direction-of-arrival estimation in satellite communication with large-space array. In: *2024 Workshop on Communication Networks and Power Systems (WCNPS)*. [S.l.: s.n.], 2024. p. 1–7. Cited in page 11.

PRATT, T.; ALLNUTT, J. E. *Satellite communications*. 3rd. ed. [S.l.]: John Wiley & Sons, 2019. Cited 3 times in pages 1, 18, and 20.

PROAKIS, J.; SALEHI, M. Textbook. *Digital communications*. Fifth. [S.l.]: McGraw-Hill, 2008. Cited in page 37.

RONDINEAU, S.; DIETLEIN, C.; POPOVIC, Z.; LEE, R. Q.; MIRANDA, F. A.; ROMANOFSKY, R. R.; INGRAM, M. A.; BAROTT, W. C.; LANGLEY, J.; MANDL, D. Ground stations of arrays to increase the LEO download capacity. In: *2006 European Microwave Conference*. [S.l.: s.n.], 2006. p. 874–877. Cited in page 2.

ROY, R.; KAILATH, T. ESPRIT-estimation of signal parameters via rotational invariance techniques. *IEEE Transactions on Acoustics, Speech, and Signal Processing*, v. 37, n. 7, p. 984–995, 1989. Cited in page 9.

SADIKU, M. N. *Elements of Electromagnetics*. 7th. ed. New York: Oxford University Press, 2018. ISBN 9780190698614. Cited 3 times in pages 86, 87, and 88.

SEKIZAWA, S. Estimation of arrival directions using MUSIC algorithm with a planar array. In: *ICUPC '98. IEEE 1998 International Conference on Universal Personal Communications. Conference Proceedings (Cat. No.98TH8384)*. [S.l.: s.n.], 1998. v. 1, p. 555–559 vol.1. Cited in page 9.

SHENG, L.; ZHAO, J.; WU, D.; HUANG, Y.; XIA, L. An unambiguous 2D DOA estimation algorithm by a large-space l-shaped array. *Circuits, Systems, and Signal Processing*, v. 42, n. 11, p. 6614–6635, 2023. Disponível em: <https://doi.org/10.1007/s00034-023-02405-3>. Cited in page 11.

SHI, W.; HE, Q.; WU, H. Generalized spatial-temporal coprime sampling for joint DOA and doppler estimation. *IEEE Geoscience and Remote Sensing Letters*, v. 20, p. 1–5, 2023. Cited in page 10.

SKLAR, B. *Digital communications: fundamentals and applications*. 3rd. ed. [S.l.]: Pearson, 2020. Cited 6 times in pages 7, 37, 38, 40, 41, and 42.

SMOLDERS, A.; VISSER, H.; JOHANNSEN, U. *Modern Antennas and Microwave Circuits – A complete master-level course*. [S.l.]: Center for Wireless Technology Eindhoven (CWTe), 2019. Cited 2 times in pages 23 and 25.

SOBRINHO, F. R.; MENDONçA, G. W. S. D.; ARAÚJO, D. C.; BORTOLOTTO, E. R.; RONDINEAU, S. R. M. J. Parabolic antenna array position estimation and calibration techniques. In: *2024 Workshop on Communication Networks and Power Systems (WCNPS)*. [S.l.: s.n.], 2024. p. 1–5. Cited in page 5.

STRANG, G. *Álgebra linear e suas aplicações*. [S.l.]: Cengage Learning, 2010. Cited in page 53.

TEUNISSEN, P.; MONTENBRUCK, O. *Springer Handbook of Global Navigation Satellite Systems*. 1st. ed. [S.l.]: Springer Publishing Company, Incorporated, 2017. ISBN 3319429264. Cited 3 times in pages 11, 64, and 65.

TONG, W.; ZHENG, Z.; WANG, W.-Q.; SO, H. C. Symmetric displaced coprime planar array for two-dimensional direction-of-arrival estimation. *IEEE Sensors Journal*, v. 22, n. 23, p. 23221–23231, 2022. Cited in page 28.

TREES, H. *Optimum Array Processing – Part IV of Detection, Estimation, and Modulation Therory*. [S.l.]: John Wiley & Sons, 2002. ISBN 0471093904. Cited 9 times in pages 1, 6, 7, 31, 32, 33, 34, 59, and 61.

VALLADO, D. A. *Fundamentals of astrodynamics and applications*. 4th. ed. [S.l.]: Microcosm Press, 2013. ISBN 9781881883203. Cited 4 times in pages 15, 18, 19, and 20.

WANG, H.; FANG, D.-G.; CHOW, Y. L. Grating lobe reduction in a phased array of limited scanning. *IEEE Transactions on Antennas and Propagation*, v. 56, n. 6, p. 1581–1586, 2008. Cited in page 11.

WANG, Z.; WANG, W.-Q.; ZHENG, Z.; SHAO, H. Nested array sensor with grating lobe suppression and arbitrary transmit–receive beampattern synthesis. *IEEE Access*, v. 6, p. 9227–9237, 2018. Cited in page 11.

XU, S.; BRIGHENTE, A.; CHEN, B.; CONTI, M.; CHENG, X.; ZHU, D. Deep neural networks for direction of arrival estimation of multiple targets with sparse prior for line-of-sight scenarios. *IEEE Transactions on Vehicular Technology*, v. 72, n. 4, p. 4683–4696, 2023. Cited in page 10.

YANG, B. Projection approximation subspace tracking. *IEEE Transactions on Signal Processing*, v. 43, n. 1, p. 95–107, 1995. Cited 2 times in pages 54 and 55.

ZAKI, S. B. M.; KAYA, N.; CHO, M. Implementation of adaptive antenna array for ground station tracking system. *Transactions of the japan society for aeronautical and space sciences, aerospace technology japan*, v. 18, p. 199–208, 09 2020. Cited 2 times in pages 1 and 2.

ZHANG, B.; LIU, Y.; ZHAO, Z.; YAN, P. Multi-beam steering with low grating lobes using optimized unequally spaced phased array. *Optics Communications*, v. 427, p. 48–53, 2018. ISSN 0030-4018. Disponível em: <https://www.sciencedirect.com/science/article/pii/S0030401818305261>. Cited in page 11.

ZHENG, S.; YANG, Z.; SHEN, W.; ZHANG, L.; ZHU, J.; ZHAO, Z.; YANG, X. Deep learning-based DOA estimation. *IEEE Transactions on Cognitive Communications and Networking*, v. 10, n. 3, p. 819–835, 2024. Cited in page 10.

APÊNDICE A

SPHERICAL COORDINATES

The **Spherical Coordinate System** will be described for the study of satellite orbits, GS arrays, and the antennas that comprise them.

A.1 DEFINITION AND CONVERSIONS

The spherical coordinate system specifies a point P in 3D space using the triplet (r, θ, ϕ) as shown in the Figure A.1, where (SADIKU, 2018):

- Radial distance (r): The distance from the origin to the point P ($r \geq 0$).
- Zenith - or colatitude - angle (θ): The angle measured from the local vertical, called Zenith direction (positive Z-axis) to the vector $\overrightarrow{OP}$ ($0 \leq \theta \leq \pi$).
- Azimuth angle (ϕ): The angle measured from the positive X-axis to the projection of the vector $\overrightarrow{OP}$ onto the XY-plane ($0 \leq \phi < 2\pi$).

In some cases it can be use the Elevation (ϑ) - angle from the local horizontal plane (X-axis) - instead of the Zenith (θ). The relationship between the two is complementary:

$$\vartheta = \frac{\pi}{2} - \theta. \tag{A.1}$$

A.2 SPHERICAL TO CARTESIAN CONVERSION

Given a point (r, θ, ϕ) in spherical coordinates, the conversion to Cartesian coordinates is

$$\begin{cases} x = & r \sin\theta \cos\phi \\ y = & r \sin\theta \sin\phi \\ z = & r \cos\theta. \end{cases} \tag{A.2}$$

Figure A.1. Spherical coordinates. Description of a position vector **r** through its versor r and the angles ϕ and θ.

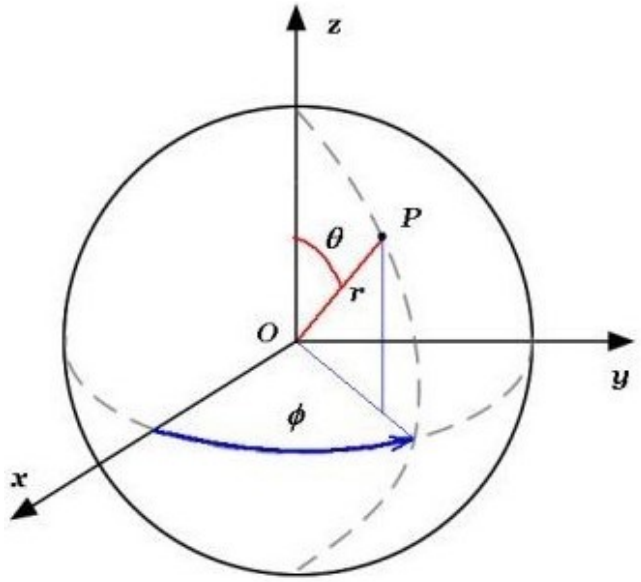

Source: (SADIKU, 2018)

Conversely, given a point (x, y, z) in Cartesian coordinates, the conversion to spherical coordinates is

$$\begin{cases} r = \sqrt{x^2 + y^2 + z^2} \\ \theta = \arccos\left(\frac{z}{r}\right) \\ \phi = \arctan\left(\frac{y}{x}\right) = \angle\left(x + jy\right). \end{cases} \tag{A.3}$$

A.3 BASIS VECTORS CONVERSION

A vector **A** expressed in Cartesian coordinates, $\mathbf{A} = A_x\hat{\mathbf{x}} + A_y\hat{\mathbf{y}} + A_z\hat{\mathbf{z}}$, visualized in Figure A.2, can be transformed into its spherical components, $\mathbf{A} = A_r\hat{\mathbf{r}} + A_\theta\hat{\theta} + A_\phi\hat{\phi}$ (SADIKU, 2018). The spherical unit vectors in terms of Cartesian coordinates are:

$$\begin{array}{lccc} \hat{\mathbf{r}} = & \sin\theta\cos\phi\hat{\mathbf{x}} & +\sin\theta\sin\phi\hat{\mathbf{y}} & +\cos\theta\hat{\mathbf{z}} \\ \hat{\theta} = & \cos\theta\cos\phi\hat{\mathbf{x}} & +\cos\theta\sin\phi\hat{\mathbf{y}} & -\sin\theta\hat{\mathbf{z}} \\ \hat{\phi} = & -\sin\phi\hat{\mathbf{x}} & +\cos\phi\hat{\mathbf{y}}. & \end{array} \tag{A.4}$$

This transformation is accomplished using a rotation matrix derived from the dot products of the unit vectors in both systems. The transformation matrix for the spherical vector components is:

$$\begin{bmatrix} A_r \\ A_\theta \\ A_\phi \end{bmatrix} = \begin{bmatrix} \sin\theta\cos\phi & \sin\theta\sin\phi & \cos\theta \\ \cos\theta\cos\phi & \cos\theta\sin\phi & -\sin\theta \\ -\sin\phi & \cos\phi & 0 \end{bmatrix} \begin{bmatrix} A_x \\ A_y \\ A_z \end{bmatrix}. \tag{A.5}$$

Figure A.2. Radial unitary vectors of r, θ and ϕ.

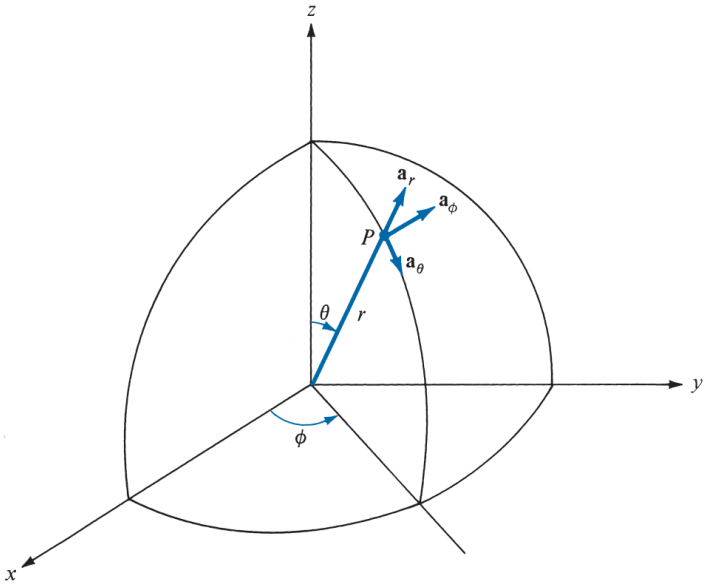

Source: (SADIKU, 2018).

APÊNDICE B

OTHER CHANNEL EFFECTS

B.1 ANTENNAS INCOMPATIBILITIES

- Polarization mismatch: occurs when the transmit and receive antennas have different polarization orientations. The effective gain is reduced by a factor $\cos^2(\Delta\theta)$, where $\Delta\theta$ is the angle between polarization vectors.

- Antenna misalignment: refers to pointing errors or mechanical deviations in the antenna array orientation, leading to beam pointing errors and reduction in effective gain. These effects are particularly critical in narrow-beam, high-frequency systems (e.g., Ka-band).

B.2 ATMOSPHERIC EFFECTS

The Earth's atmosphere is not a perfect vacuum and introduces several forms of attenuation, which become particularly severe at the higher frequencies (Ku, Ka, and Q/V bands) used in modern satellite systems.

- Atmospheric Absorption: Gaseous molecules in the atmosphere, primarily oxygen and water vapor, absorb energy from the passing radio wave, converting it into heat. This absorption is highly dependent on frequency, with significant attenuation peaks occurring at the resonant frequencies of these molecules (e.g., around 22 GHz for water vapor and 60 GHz for oxygen). The attenuation due to atmospheric absorption, A_a (dB), is a function of the signal's path length through the atmosphere, which in turn depends on the ground station's elevation angle to the satellite.

- Rain Attenuation: Hydrometeors such as rain, fog, and clouds can severely attenuate and scatter the signal. Rain is the most significant factor, with the effect increasing

dramatically with frequency and rain rate. The specific attenuation, γ_R (dB/km), can be modeled using a power-law relationship $\gamma_R = kR^\alpha$, where R is the rain rate in mm/h, and the coefficients k and α depend on the signal's frequency and polarization.

- Tropospheric/Ionospheric Scintillation: At frequencies above 10 GHz, turbulent mixing of air with different temperatures and humidity in the troposphere can cause rapid fluctuations in the signal's amplitude and phase. In the ionosphere, irregularities in electron density can cause similar rapid fluctuations, particularly at lower frequencies (L-band and S-band).

B.3 FADING

The received signal strength can experience rapid fluctuations, known as fading. This is a combination of large-scale effects due to major obstacles and small-scale effects due to multipath propagation.

- Shadowing (Large-Scale Fading): As the satellite moves, the path can be obstructed by large objects like buildings or hills, causing a significant drop in the mean signal power. This effect is known as shadowing and is typically modeled by a log-normal distribution.

- Multipath Fading (Small-Scale Fading): The signal arrives at the receiver via multiple paths, causing rapid fluctuations around the mean signal level. This is often modeled by one of two statistical distributions:

  - Rician Fading: This model is applicable when a strong, dominant Line-of-Sight (LoS) path exists between the satellite and the ground station, in addition to multiple weaker, scattered non-LoS paths. The probability density function of the received signal envelope, $r(t)$, follows a Rician distribution. The severity of the fading is characterized by the Rician κ-factor (kappa, the ratio of the power in the LoS component to the power in the scattered components). A high κ indicates a strong LoS path and less severe fading. This is the typical fading model for LEO systems in open or suburban areas.

  - Rayleigh Fading When the LoS path is completely obstructed, the received signal

is a sum of many non-LoS components with no single dominant path. In this case, the signal envelope follows a Rayleigh distribution, which represents a more severe fading condition.

B.4 MULTIPATH PROPAGATION

As already said in the Section 1.2.3, In a realistic environment the signal does not only arrive via the direct LoS path. It also reflects and scatters off the ground, buildings, and other obstacles, creating multiple indirect paths to the receiver. This is multipath propagation. The received signal is then a superposition of the LoS component and several Non-Line-of-Sight (NLoS) delayed, attenuated, and phase-shifted replicas. When multiple signals (the LoS satellite signal, multipath components, and potential interferers) are present, the received signal model is expanded to a sum over all incident waves component:

$$r_{\text{NLOS}}(t) = \sum_{l=1}^{L} \alpha_l s(t - \tau_l) e^{j\phi_l},$$

where L is the number of paths, and τ_l, α_l, ϕ_l are delay, amplitude, and phase of the l-th path respectively.

The envelope of the received passband signal under Rician fading - described in Section 3.3 - and considering no LoS delay is:

$$r(t) = \sqrt{\frac{\kappa}{\kappa+1}} s(t) e^{j\phi} + \sqrt{\frac{1}{\kappa+1}} \sum_{l=1}^{L} a_l s(t - \tau_l) e^{j\phi_l}.$$

Taking the limit $\kappa \to \infty$, it means that is no multipath, thus this sampled equation becomes the (3.1) with no noise.

In scenarios with strong multipath (e.g., near reflective surfaces), ISI becomes significant and must be addressed via pulse shaping or equalization techniques. Figure B.1 illustrates this effect.

Figure B.1. Illustration of multipaths that an original transmitted signal (red) can travel, reflected (purple) by obstacles in the environment, and generate unwanted readings of its copies.

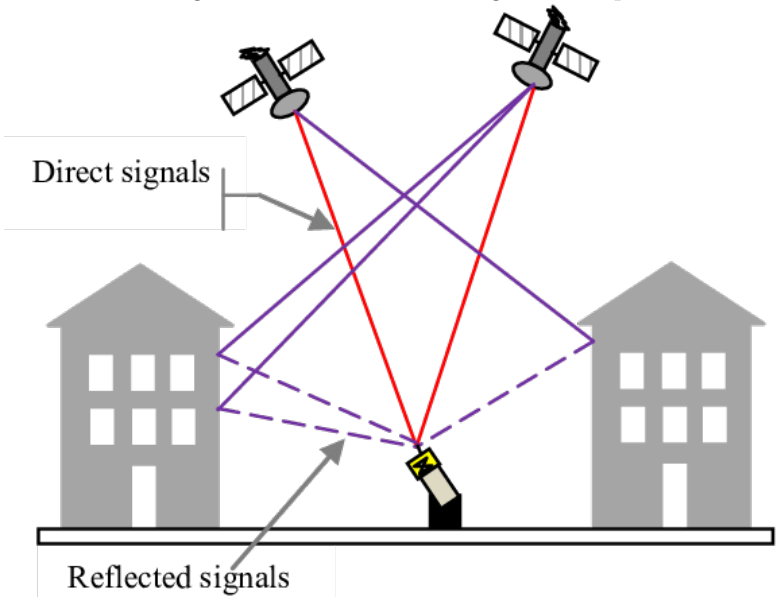

Source: (KUMAR *et al.*, 2013).